

Total Internal Reflection Fluorescence Microscopy to Study Bitumen and Clay
Interaction in Oil Sands Tailings

by

Swapnali Shende

A thesis submitted in partial fulfillment of the requirements for the degree of

Master of Science

in

CHEMICAL ENGINEERING

Department of CHEMICAL AND MATERIALS ENGINEERING
University of Alberta

© Swapnali Shende, 2016

Abstract

Oil sands tailings management remains to be a major challenge for oil industry in Canada. Promoting quick settling of fines in tailings ponds is the key to its treatment. Bitumen lost to tailings during oil sands extraction is also believed to hinder settling and consolidation of clays in tailings ponds. Complete understanding of the factors that impede fast settling of tailings would be the ground work for development of improved tailings settling techniques and flocculants.

In this study, bitumen-clay association and effect of bitumen on clay particle-particle interactions in mature fine tailings (MFT) is investigated with Total Internal Reflection Fluorescence (TIRF) microscope among other techniques. Bitumen displays natural fluorescence when illuminated with 488 nm and 543 nm. This was also established using spectrofluorometer. Fluorescence microscope imaging, ensured that clay and water did not show fluorescence. These outcomes along with high axial resolution and high contrast of TIRF were utilized to understand how bitumen interacts with clay surface in MFT. MFT sample were also diluted with process water and deionized water separately, to recognize clay boundaries under bright field microscope. The presence of hydrophobic fine clay agglomerates along with the hydrophilic clay particles was apparent from the TIRF results. Bitumen was detected to be coating clay particles and bridging clay agglomerates. By reducing the laser intensity, at laser angle above critical angle, bitumen was observed to be only partially coating some clay surfaces. The existence of biwettable clays in MFT was evident in these images. Confocal Laser scanning microscope (CLSM) which also gives high contrast images with controlled depth of field, confirmed the presence of non-uniform bitumen coating in clay surfaces. At 0.21 μm resolution, no free bitumen could be apprehended. Using He-ion microscope (HIM) which gives resolution up to 0.25 nm and high surface sensitivity, preliminary MFT images were obtained to clearly witness the layered structure of clays.

Correlative studies with HIM and TIRF will pave way to realize the clay surface properties that are partially coated with bitumen.

Acknowledgements

I would like to thank Dr. Neda Nazemifard and Dr. Zubin Jacob for believing in me and guiding me throughout the program. I also want to express thanks to Sarang Pendharker for being there whenever I ran into problems. I'm grateful towards Dr. Xiaoli Tan for many meaningful discussions. Many thanks to Gareth Lambkin, Ni Yang and Brittany Mackinnon for help with the microscope and samples. I want to thank our project sponsors, Institute of Oil Sands Innovation (IOSI) who believed in this research. I would like to thank Dr. Qi Liu and Dr. William McCaffrey along with my supervisor and co-supervisor for being in my defense committee.

Finally, I would like to show gratitude to my parents who made me capable of being here today. My parents never taught me that it is ok to give up. Also my Husband, Nitin Arora who has been my best friend all along and never pulled me down. Thanks to all my friends who were there for me through the ups and downs of my life.

Table of Contents

Chapter 1: Introduction	1
1.1 Oil Sands Overview	1
1.2 Research Objective	4
1.3 Thesis Layout.....	5
1.4 Reference	5
Chapter 2: Literature review.....	7
2.1 Oil Sands Tailings.....	7
2.2 Role of bitumen in tailings.....	11
2.3 Optical microscope	12
2.4 Fluorescence microscope	14
2.5 Total Internal Fluorescence reflection (TIRF) microscope	16
2.6 Electron microscopy	20
2.7 Image Acquisition and Processing.....	21
2.8 References.....	22
Chapter 3: Total Internal Reflection Fluorescence Microscopy to Investigate the Distribution of Residual Bitumen in Oil Sands Tailings	27
3.1 Introduction.....	27
3.2 Experimental Section	30
3.2.1 Spectrofluorometer	30
3.2.2 Confocal Epifluorescence Microscope	31
3.2.3 TIRF Microscope.....	33
3.3 Results and Discussion	34
3.3.1 Spectrofluorometer	34
3.3.2 Confocal TIRF and Epifluorescence Microscope.....	36
3.4 Conclusion	42

3.5 References.....	43
Chapter 4: Total Internal Reflection Fluorescence Tomography to Study Bitumen and Clay interaction in Oil Sands Tailings	48
4.1 Introduction.....	48
4.2 Experimental Section.....	50
4.2.1 Total Internal Reflection Fluorescence (TIRF) Microscope.....	51
4.2.2 Confocal laser scanning Microscope (CLSM).....	52
4.2.3 Post Dean Stark Analysis Imaging	53
4.3 Results and Discussion	53
4.3.1 Total Internal Reflection Fluorescence (TIRF) Microscope.....	56
4.3.2 Confocal Laser Scanning Microscope (CLSM).....	61
4.3.3 Post Dean Stark Analysis Imaging	63
4.4 Conclusion	63
4.5 References.....	64
Chapter 5: Conclusion and future work.....	68
References (All).....	70
Appendix A: Sample Preparation for Spectrofluorometer and fluorescence microscope	81
Appendix B: Code for 3D Reconstruction of fluorescence images Bitumen Coating on Clay in MFT Samples	84
Appendix C: Code for Animation of the 3D Reconstruction of fluorescence images Bitumen Coating on Clay in MFT Samples	102

Table of Figures

Figure 1-1: Generic flowsheet for bitumen production from surface mining (Masliyah, Jacob H. (Jacob Heskell), Xu, Z. (Zhenghe), Czarnecki, Jan A. (Jan Adam), Dabros, 2011).....	2
Figure 2-1: Schematic for fluid fine tailings (FFT) (R. Mikula & Omotoso, 2006).....	7
Figure 2-2: Schematic of fluorescence microscope (Dobrucki, 2013).....	15
Figure 2-3: Incident light is focused at an angle greater than critical angle so that it is completely reflected. But an evanescent wave is generated near sample-coverglass interface.	19
Figure 3-1: Fluorescence emitted by bitumen on illumination with an excitation laser. Clay does not show fluorescence, and hence, clay and bitumen show a high contrast in fluorescent images.	30
Figure 3-2: Athabasca bitumen that was observed using epifluorescence microscopy techniques.	32
Figure 3-3: Kaolin (model clay) used to observe the fluorescence intensity difference between bitumen and clay.	33
Figure 3-4: MFT sample from Syncrude tailings pond.....	33
Figure 3-5: TIRF microscope schematic. The sample is illuminated by evanescent fields near the surface of the coverslip.	34
Figure 3-6: Image A shows a spectrofluorometer graph depicting the change in fluorescence intensity for a range of excitation and emission wavelengths for a 4 mL sample of toluene. Images B, C, and D show this graph for 0.1, 0.5, and 0.3 g/L bitumen in toluene, respectively.....	35
Figure 3-7: Images A and D represent the bright-field image of kaolin and Athabasca bitumen, respectively. Images B and E show the epifluorescence images of clay and Athabasca bitumen, respectively, for excitation with a xenon lamp and emission filter of 500–550 nm. Images C and F show the epifluorescence images of clay and Athabasca bitumen, respectively, for excitation with a xenon lamp and emission filter of 560–640 nm. Clay is not showing substantial fluorescence compared to the strong fluorescence of bitumen.....	37
Figure 3-8: Image A shows a bright-field image of the clay and bitumen interface. Image B shows the fluorescence image of the clay and bitumen interface for excitation with a xenon lamp and emission filter of 500–550 nm. Image C shows the fluorescence image of the clay and bitumen interface for	

excitation with a xenon lamp and emission filter of 560–640 nm. A clear clay and bitumen interface is visible with epifluorescence. 38

Figure 3-9: Image A shows a bright-field image of the water and bitumen interface. Image B shows the fluorescence image of the water and bitumen interface for excitation with a xenon lamp and emission filter of 500–550 nm. Image C shows the fluorescence image of the water and bitumen interface for excitation with a xenon lamp and emission filter of 560–640 nm. The water and bitumen interface is clearly seen with epifluorescence. 38

Figure 3-10: Image A shows a bright-field image of the MFT sample. Image B shows the TIRF images of the MFT sample for an excitation laser of 488 nm and emission filter of 500–550 nm, and image C shows the TIRF image of the MFT sample for an excitation laser of 543 nm and emission filter of 560–640 nm. MFT sample fluorescence images indicate that the fluorescing bitumen particles dispersed in non-fluorescing clay and water. Image D shows 3D reconstruction of the MFT sample at the same location and settings as image B. 39

Figure 3-11: Image A shows a bright-field image of the diluted MFT sample. Image B shows the TIRF images of the diluted MFT sample for an excitation laser of 488 nm and emission filter of 500–550 nm, and image C shows the TIRF image of the diluted MFT sample for an excitation laser of 543 nm and emission filter of 560–640 nm. The diluted MFT sample fluorescence image shows fluorescing bitumen particles near the clay particle location in the bright-field image. Image D shows 3D reconstruction of the diluted MFT sample at the same location and settings as image B. 40

Figure 3-12: Superimposed bright-field and 488 nm excitation laser TIRF images of the diluted MFT sample. The dark gray particles in these images are clay particles, while the green dots are bitumen. 41

Figure 4-1: Well type slide with glass coverslip bottom for imaging wet MFT and dilute MFT samples in epifluorescence microscope. 51

Figure 4-2: Sample illuminated by evanescent water in TIRF microscope using objective lens technique to direct the laser beam. 52

Figure 4-3: Image A is TIRF image of MFT sample. Fluorescing bitumen can be clearly seen in the non-fluorescing medium. Image B is the grayscale image of image A developed using yen algorithm for thresholding. Thresholding gives clear boundaries of bitumen but the low intensity bitumen particles are lost in this image. The thickness of bitumen coating for few particles is shown here. Image C is the graph with number of bitumen particles on x axis and area of bitumen on y axis. This graph roughly shows the bitumen distribution. 54

Figure 4-4: Images A and B are the TIRF image of Syncrude MFT 2014. Image C is the TIRF image of Syncrude 2012 and image D is TIRF image of CNRL MFT 2016. These images were taken with reduced laser intensity. They show the features within the fluorescing bitumen coating. CNRL MFT 2016 show smaller fluorescing aggregates compared the Syncrude MFT 2012 and 2014. 56

Figure 4-5: Image A is the optical section of the TIRF z-stack images for Syncrude MFT 2014 sample. Image B, C and D show the 3D reconstruction of an aggregate in the image A. It is apparent from these images that bitumen coating on these clay aggregates is non-uniform. There are regions on some of the clay surfaces where bitumen coating is absent. 58

Figure 4-6: Image A is the optical section of the TIRF z-stack images for Syncrude MFT 2014 sample. Image B depicts region of interest with focus on a single aggregate. Image C is the 3D reconstruction of the single aggregate in image B. The uneven bitumen coating can be clearly seen in these images. 59

Figure 4-7: Images A and B are Syncrude MFT 2014 in deionized water sample taken while the laser and diascopic lamp were simultaneously on. These images show the presence of bitumen coated clay aggregates that have settled on the glass coverslip. Images C and D are Syncrude MFT 2014 in process water sample taken while the laser and diascopic lamp were simultaneously on. These images show that not all clay particles are coated with bitumen. They also show the uneven bitumen coating on clay with some sections having higher fluorescence intensity while others with slightly lower fluorescence intensity. 60

Figure 4-8: Images A and D are dilute Syncrude MFT 2014 sample images taken with Confocal Laser Scanning Microscope (CLSM) 488nm laser. Images B and E are Syncrude MFT 2014 sample images taken with Confocal Laser Scanning Microscope (CLSM) 632nm laser and emission below 530nm and above 660nm are blocked so that no fluorescence is captured by reflection from clay particles are captured. Image C and F shows the superposed images of fluorescence from bitumen and reflection from clay. In the superimposed images the yellow portion shows the overlap while the red part is clay and green part is the bitumen. 61

Figure 4-9: These superimposed bright field and TIRF images of Syncrude MFT 2014 after dean stark was performed on it. These images show the presence of low percentage of bitumen still present in the dried solids after the dean stark. This represent the difficult of remove bitumen. 62

List of Abbreviations

TIRF	Total Internal Reflection Fluorescence microscope
MFT	Mature Fine Tailings
SEM	Scanning Electron Microscopy
TEM	Transmission Electron Microscopy
AFM	Atomic Force Microscopy
PMT	Photo Multiplier Tubes
CHWE	Clark Hot Water Extraction
LEE	Low Energy Extraction
XRD	X-ray Diffraction
CLSM	Confocal Laser Scanning Microscope
SAGD	Steam-assisted gravity drainage
CSS	Cyclic Steam Stimulation
VAPEX	Vapour Extraction Process
THAI	Toe to Heel Air Injection
SFE	Supercritical Fluid Extraction
CT	Composite/ Consolidated Tailings
TRO	Tailings Reduction Operations
AFD	Atmospheric Fines Drying
NA	Numerical Aperture

Nomenclature

$\eta (1)$	Refractive index of immersion oil
$\eta (2)$	Refractive index of sample
θ	Half of the objective lens angular aperture
θ_c	Critical angle
θ_1	Angle of the incident
θ_2	Refracted beam angle
λ	wavelength of incident light
$E (z)$	Energy values as a function of z
$E (0)$	Energy at the interface
d	Depth to which evanescent wave penetrates
m	Magnification of the lens
λ_i	Wavelength of the incident light
D	Diameter of Airy disks
M	Magnification of optical microscope
M_1 and M_2	Magnification of objective and ocular
DOF	depth of field

Chapter 1: Introduction

1.1 Oil Sands Overview

Oil sands in Canada are world's largest unconventional oil reserves. These are world's third largest oil reserves and are mainly located in the Athabasca, Cold Lake and Peace River region of Alberta. They represent about 98% of Canada's oil reserves (Alberta issuing body, 2015). They span over 14000 km² and are proven to hold about 170 billion barrels of oil (Masliyah, Zhou, Xu, Czarnecki, & Hamza, 2004).

Oil sands exploration activity was started by the government in the early 1920s. Suncor Energy Inc. opened its commercial oil sands processing facility in 1967. Syncrude began its operation in 1978. Shell Albian Sands commenced its mining activities near the Muskeg River in 1999. Canadian Natural Resources Limited (CNRL) Horizon Sands Project was initiated by 2009. These four major operators have been in operation for over 40 years (Masliyah, Jacob H. (Jacob Heskell), Xu, Z. (Zhenghe), Czarnecki, Jan A. (Jan Adam), Dabros, 2011).

Oil from Oil sands is not only an important supply for the country but a global solution in face of oil scarcity. Oil sands are called unconventional oil source because they have high carbon to hydrogen ratio and higher density and viscosity (Masliyah et al., 2004). They also have higher percentage of heavy metals and sulphur making them slightly expensive to process and gaining lower selling price. They contains approximately 80-85 wt% of minerals, 3-6 wt% water and 12 wt% bitumen. The minerals present are mainly quartz, silt, sands and clay (Kasperski, 2001).

Bitumen is mined either using surface mining or in-situ techniques. The surface mining technique involves excavating, crushing the large lumps, adding hot water to create slurry, and transporting it to extraction units for further processing. In-situ extraction involves drilling wells and injecting steam. This reduces bitumen viscosity and it flow into the wells, from where it is pumped out. Steam-assisted gravity drainage (SAGD) is the most efficient in-situ technique. This technique involves drilling two horizontal parallel wells parallel and pumping in steam, and collecting bitumen once it flows into the well, then it is pumped to the surface (Dyer & Huot, 2010). Cyclic Steam Stimulation (CSS), Vapour Extraction Process (VAPEX), Toe to Heel Air Injection (THAI) and Supercritical Fluid Extraction (SFE) are some experimental in-situ extraction methods (Butler

& Mokrys, 1998)(Xia, Greaves, Turta, & Ayasse, 2003). Approximately 10-20% of oil sands deposits can be recovered with surface mining. The rest can be extracted using in-situ techniques.

Figure 1-1 shows flow scheme of bitumen extraction using surface mining. Currently hot/ warm water extraction process is mostly used commercially. In this method the oil sands ore is mixed with hot water and agitated to liberate bitumen from the sand grains. Typically caustic (NaOH) is added to raise pH. Raising the pH helps in releasing natural surfactants from bitumen (Schramm & Smith, 1985). It also modifies surface potentials of bitumen and minerals, reduces the divalent ion concentration and decreases solids hydrophobicity. The pH range 8.5 – 9.0 is most favorable for bitumen recovery. (Chalaturnyk & Scott, 2002). This treatment promotes bitumen liberation from minerals by reducing the interfacial tension. The slurry is conditioned and transported in hydro transport pipelines during which the sand grains separate. It goes through various flotation stages to assist bitumen-air attachment. The top bitumen layer is skimmed and water and solids are sent to the tailings ponds. Bitumen froth is further treated to recover bitumen.

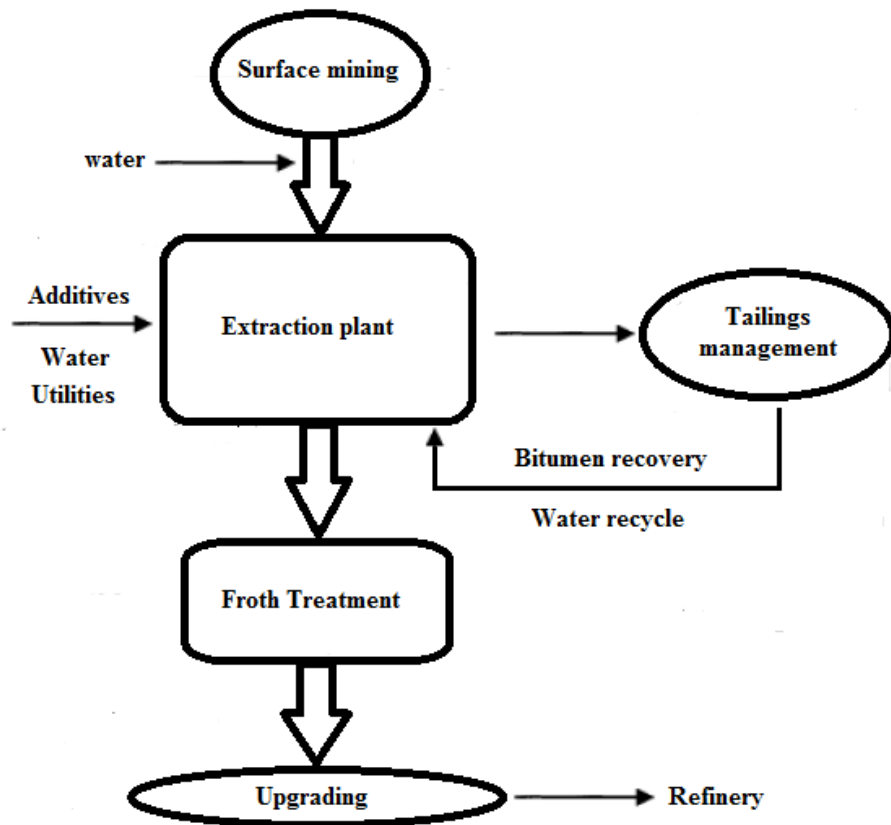


Figure 1-1: Generic flowsheet for bitumen production from surface mining (Masliyah, Jacob H. (Jacob Heskell), Xu, Z. (Zhenghe), Czarnecki, Jan A. (Jan Adam), Dabros, 2011)

Effective bitumen recovery during the above steps is dependent on the suitable lump size reduction of oil sands ore, followed by bitumen liberation from minerals influenced by the process temperature, interfacial properties, mechanical agitation, and chemical additives, followed by bitumen attachment to air bubble governed by the process temperature and finally the aerated bitumen floatation to the top of the separation vessel, where it is skimmed. Bitumen extraction is strongly influenced by physical, chemical and hydrodynamic conditions with interfacial phenomena playing a critical role. Research has been performed to introduce low temperature extraction process to reduce operating cost. In this technique oil sands slurry is prepared between 2-15 °C along with conditioning agent such as kerosene, diesel. This slurry then undergoes froth floatation for the recovery of the bitumen (Hepler & Smith, 1994). This technique does not provide bitumen recovery comparable to the warm water extraction process.

Hot/ warm water extraction process work on the principle that minerals in oil sands are hydrophilic. To promote bitumen liberation it is important that bitumen-water interaction is stronger than bitumen-sand interaction (Masliyah, Jacob H. (Jacob Heskell), Xu, Z. (Zhenghe), Czarnecki, Jan A. (Jan Adam), Dabros, 2011). The sands grains are believed to be enveloped with thin water film (~10 nm) which is coated by bitumen (Camp, 1976)(Takamura, 1982). Existence of this water coating on sand remains to be experimentally verified. It has been discovered that organic-coated and biwetttable solids exist in oil sands (Adegoroye, Wang, Omotoso, Xu, & Masliyah, 2010). The hydrophilic nature was the only reason for the water-based extractions to work. The presence of hydrophobic and biwetttable solids reduce efficiency of bitumen recovery (Sepulveda & Miller, 1978). Since bitumen-sand liberation is thermodynamically unfavorable mechanical energy is required for detachment (Masliyah, Jacob H. (Jacob Heskell), Xu, Z. (Zhenghe), Czarnecki, Jan A. (Jan Adam), Dabros, 2011). Solvent-based techniques have also been developed. These techniques could help environment by reducing the dependence on water for processing and decrease the amount of tailings (Meadus, Chevrier, & Sparks, 1982). But recovery of solvent after processing is still a challenge and these techniques are not proven to be profitable.

Bitumen obtained from extraction unit, consists approximately of 84% of Carbon, 10% of Hydrogen, 1% of Oxygen and 5% of Sulphur. Bitumen can used either in gasoline and petrochemicals production or in asphalt production (Masliyah et al., 2004). Production of one

barrel of bitumen requires 1.8 tons of oil sands and 2.5 m³ of water and produces about 3.3 m³ of tailings (Masliyah, Jacob H. (Jacob Heskell), Xu, Z. (Zhenghe), Czarnecki, Jan A. (Jan Adam), Dabros, 2011). Tailings presents a major environmental and economic challenge due to its settling time spanning over several decades and tailings ponds covering areas as large as 180 km².

1.2 Research Objective

Slow settling rates of tailings have been a serious problem in oil sands processing. The bitumen in tailings is argued to obstruct consolidation of tailings by attaching to clay. It is believed to associate with clays and increase viscosity of the MFT thus preventing further settling. It is also been thought to bridge clays together hence creating a torturous path impeding further dewatering.

Information is available regarding chemical composition of various clays in tailings. Studies have been performed to learn the inorganics surface through chemical identification but these interaction which take place at nanoscale and morphology of attached bitumen is not known. This thesis is a portion of a larger research project aimed at understanding the surface and bulk interactions between organic materials and clays in oil sands tailings. It also targets to identify the role to bitumen in preventing clay consolidation and settling. Recognizing bitumen and clay association and impact of bitumen on clay-clay interaction will aid with development of more effective chemical and processes to accelerate clay aggregation and sedimentation in tailings which will reduce settling and dewatering time.

The specific goals of this thesis project were as follows:

- Provide high resolution optical images of MFT which will map bitumen-clay interaction and bitumen surface coverage.
- TIRF microscope employed in this research, provides images that are organic material specific, high contrast and have resolution beyond the optical diffraction limit and also make clay surface characterisation possible.
- TIRF microscope with its ability of low background noise will aid with finding if the clay surface is completely or partially coated by bitumen.
- TIRF real-time imaging of MFT without any manipulation of sample surface condition will be used to observe MFT sample in its true state.
- 3D imaging will shed light on the 3D clay-bitumen surface morphology.

The effectiveness of TIRF in this research will pave way to this technique being used as a standard tool for such organic-mineral interaction studies in industry.

1.3 Thesis Layout

This thesis is organised into 6 chapters. Chapter 1 gives background information of oil sands, bitumen extraction and tailings. Chapter 2 provides an overview on wealth of topics that support this study. It gives overview on oil sands tailings and role of bitumen in tailings. It also briefly talks about optical microscope, fluorescence microscope, total internal reflection fluorescence (TIRF) microscope, electron microscope and image acquisition and processing. In chapter 3, the work on spectrofluorometer, fluorescence microscope and preliminary TIRF results are discussed. The content in this chapter is adapted from the paper that was published in ACS Publications, Energy & Fuels journal. Chapter 4 discusses the findings obtained by manipulating laser intensity and angles in TIRF. The results from TIRF are supported with confocal laser scanning microscope (CLSM). Post dean stark imaging of MFT is also presented in this chapter which represents the difficult to remove bitumen in tailings. The content in this chapter has been submitted to Elsevier Publications, Fuel journal and is under peer review. Chapter 5 puts forth the results of this research and possible future work. References have been cited at the end of each chapter. All reference are also cited together after chapter 5. Appendix A gives information on sample preparation. Appendix B provides the code developed by the PDF in our group for 3D reconstruction of fluorescence images bitumen coating. Appendix C gives the code for animation of this 3D reconstruction showing its layer by layer construction and then 360° view. This code was also developed by the PDF of our group.

1.4 Reference

- Adegoroye, A., Wang, L., Omotoso, O., Xu, Z., & Masliyah, J. (2010). Characterization of organic-coated solids isolated from different oil sands. *Canadian Journal of Chemical Engineering*, 88(3), 462–470. doi:10.1002/cjce.20294
- Alberta issuing body. (2015). Lower Athabasca Region: tailings management framework for the mineable Athabasca oil sands. Edmonton: Government of Alberta.
- Butler, R. M., & Mokrys, I. J. (1998). Closed-loop extraction method for the recovery of heavy oils and bitumens underlain by aquifers: The vapex process. *Journal of Canadian Petroleum Technology*, 37(4), 41–50. doi:10.2118/98-04-04

- Camp, F. W. (1976). *The Tar Sands of Alberta, Canada* 3rd ed. Cameron Engineers Denver.
- Dyer, S., & Huot, M. (2010). *Mining vs In Situ Fact Sheet. What is the highest environmental impact oil?* Pembina Institute. Retrieved from <https://www.pembina.org/reports/mining-vs-in-situ.pdf>
- Hepler, L. G., & Smith, R. G. (1994). *Alberta oil sands: Industrial procedures for extraction and some recent fundamental research.*
- Kasperski, K. L. (2001). *Review of research on aqueous extraction of bitumen from mined oil sands.* Edmonton, Alta: CANMET, Western Research Centre.
- Masliyah, J., Zhou, Z. J., Xu, Z., Czarnecki, J., & Hamza, H. (2004). *Understanding Water-Based Bitumen Extraction from Athabasca Oil Sands.* *The Canadian Journal of Chemical Engineering*, 82(4), 628–654. doi:10.1002/cjce.5450820403
- Masliyah, Jacob H. (Jacob Heskell), Xu, Z. (Zhenghe), Czarnecki, Jan A. (Jan Adam), Dabros, M. (2011). *Handbook on theory and practice of bitumen recovery from Athabasca Oil Sands (volume 1:).* Kingsley Knowledge Publishing.
- Meadus, F., Chevrier, P., & Sparks, B. (1982). *Solvent extraction of athabasca oil-sand in a rotating mill Part 1. Dissolution of bitumen.* *Fuel Processing Technology*, 6(3), 277–287.
- Schramm, L. L., & Smith, R. G. (1985). *The influence of natural surfactants on interfacial charges in the hot-water process for recovering bitumen from the Athabasca oil sands.* *Colloids and Surfaces*, 14(1), 67–85.
- Sepulveda, J., & Miller, J. D. (1978). *Separation Of Bitumen From Utah Tar Sands By A Hot Water Digestion-Flotation Technique.* *Min. Eng*, 30(9), 1311–1320.
- Takamura, K. (1982). *Microscopic structure of Athabasca oil sand.* *Canadian Journal of Chemical Engineering*, 60(4), 538–545.
- Xia, T. X., Greaves, M., Turta, A. T., & Ayasse, C. (2003). *THAI-A “Short-distance Displacement” In Situ Combustion Process for the Recovery and Upgrading of Heavy Oil. Oil and Natural Gas Production*, 81(March).

Chapter 2: Literature review

2.1 Oil Sands Tailings

Tailings are waste by-product from oil sands extraction. They are water based suspension containing sand, clays, silt and residual bitumen. They can also contain contaminants such naphthenic acids, polycyclic aromatic hydrocarbons, phenolic compounds, ammonia, mercury and other trace metals. Hence they need to be carefully stored to prevent harm to the environment. A zero discharge policy has been issued for the oil sands industry which makes its storage in tailings ponds mandatory.

Tailing are treated with calcium sulphate (gypsum) by some companies like Syncrude, Suncor and CNRL (Gray, 1998). Calcium ions in gypsum destabilize this suspension and speed up the settling (Caughill, Morgenstern, & Scott, 1993). These tailings are sent to tailings ponds, where the coarse sands settle out to form beaches, as seen in *Figure 2-1*. Within few years, the finer particles form fluid fine tailings (FFT) with approximately 8 wt% solids.

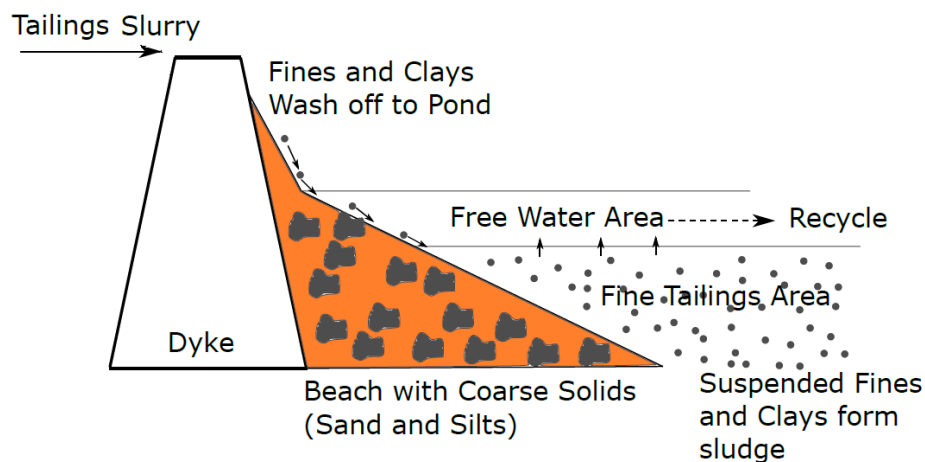


Figure 2-1: Schematic for fluid fine tailings (FFT) (R. Mikula & Omotoso, 2006)

These fine tailings further settle to form three zones. The top 3-4 m layer is water which is recycled back to the process. The middle 1-2 m layer is the transition zone with water, sand and clay. The lowest layer is called mature fine tailings (MFT). This layer consist of fine sand, silt, clay, water and some bitumen. Typically MFT has about 30 wt% solids and about 5 wt% fugitive bitumen. Typically mineral content is about 65% clay, 30% silt and 5% sand. The key clays in MFT are

kaolinite, illite, smectite and mixed-layer clay such as kaolinite-smectite and illite-smectite. All these clays are comprised of layers of silicon (Si^{4+}) tetrahedral sheets and aluminum (Al^{3+}) or magnesium (Mg^{2+}) octahedral sheets. These clays are classified based on the ratio of their tetrahedral to octahedral sheets into 1:1 type having an octahedral and a tetrahedral sheet and 2:1 type with an octahedral sheet between two tetrahedral sheets. Isomorphic substitution in clays is an important characteristic that influences their behaviour. These substitutions can occur in octahedral and/ or tetrahedral layer giving it a net charge. These charges are balanced either by the interlayer or outer surface hydrated cations such as Na^+ , K^+ , Mg^{2+} and Ca^{2+} and these ions can be usually exchanged. Some pH dependent charges such as charges introduced by the functional groups, also exist on the clays. The exchangeable ions also balance these changes. These exchangeable ions along with the pH dependent charges determine the cation exchange capacity (CEC) of a clay. CEC of clay is also an important characteristic in determining its effect on settling behaviour of MFT. These exchangeable cations are near the surface of clay and positive counter ions in the solution balance these creating an electric double layer. The pH of the solution affects the properties of clay surface affecting its dispersion or flocculation. For example, increasing the concentration of divalent exchangeable cations will increase the flocculation of clay. Sedimentation of tailings forms a gradient of mineral concentration and size along the depth of tailings while bitumen has parabolic distribution (Gray, 1998). After reaching 30 wt% solid concentration, MFT becomes stable forming a gel which entraps both coarse and fine solids in a network. Further dewatering of MFT without intervention, can take several decades. Tailing ponds are occupying over 180 km² area and millions of cubic meters FFT are present in these tailings, necessitating development of better management processes (Kaura, 2014).

Alberta Energy Resources Conservation Board (ERCB) and Alberta Environment regulate oil sands activities. Under the Environmental Protection and Enhancement Act, industries are required to restore all disturbed land with specific revegetation. Directive 074 issued in 2009 by the government to regulate tailings handling schemes for industries. It required companies to eventually eliminate long term storage of tailings and change tailings ponds into trafficable area. It also demanded that the fresh water consumption should be minimized and maximize water recycle (McFadyen, 2009). There are various other policies and legislation in place like Alberta public agencies governance act, oil sands conservation act, responsible energy development act, water act, public lands act, guidelines for wetland establishment on reclaimed oil sands leases, etc.

to guide with tailings management (Fine Tailings Fundamentals Consortium Alberta Energy, 1995). Academic and industrial research directed at improvement of tailing managements have been underway.

Conventionally, sedimentation or self-consolidation technique was used for tailings management. Since it was a natural process and required no inputs, it was quite inexpensive. But it took decades to settle. Several techniques such as centrifugation, filtration and capping has been commercially explored. But these techniques either have not shown sufficient improvement in settling rates or are uneconomical. Composite/ Consolidated Tailings (CT) by Syncrude, Tailings Reduction Operations (TRO) by Suncor and Atmospheric Fines Drying (AFD) by Shell were submitted to the government after the directive 074 (Powter, Biggar, Silva, McKenna, & Scordo, 2011).

The CT technique involves mixing MFT with coarse sand from cyclone underflow tailings and gypsum in a specific predetermined ratio to create a non-segregating slurry (Matthews, Shaw, MacKinnon, & Cuddy, 2002). This mixture rapidly consolidates to about 80 wt% solids. It is then capped with sand and soil, to enable the growth of natural foliage or transported by pipeline to the CT plant. This techniques helped Syncrude to reduce inventories and reclaim land faster. Syncrude has been using this technology since 2000 at Mildred Lake site to reclaim land at east mine pit. It has also started using the CT technique at the Aurora mine. Syncrude is the first to reclaim and hand over some of land used for oil sands excavation back to the government. Even though CT technique is a low cost solution, but the build-up of calcium and sulphate ions from gypsum in recycle water is harmful for bitumen extraction. The efficiency of this technique is also sensitive to process upsets (COSIA, n.d.-a).

The TRO and AFD techniques use the flocculent used in municipal water treatment facilities to separate clay and water. Flocculent works using two major mechanisms namely bridging and charge neutralization. Bridging mechanism involves attachment of polymer to two or more particles and bringing them together. Charge neutralization mechanism involves particles being brought together by shrinking their electric double layer. Thus reducing the particle-particle repulsion and inducing their flocculation (Gregory & Barany, 2011). The MFT which has thickened after the addition of flocculent is then spread on beaches for further natural drying. The resulting dried material can be reclaimed in the same location or can be transported to another location for reclamation. The implementation of TRO has shown substantial reduction in the

volumes of fluid tailings for Suncor. It is working towards progressively reducing the total amount of its untreated fluid tailings volumes. The AFD technology has helped to capture over 1 million tonnes of fines at the Muskeg River Mine. Research is being performed to develop better flocculants and improve the efficiency of these tailings management techniques (COSIA, n.d.-b).

It has been found that if Clark Hot Water Extraction used the settling rates are slower compared to OSLO Hot Water Extraction process. This is mainly due to the use of caustic during the extraction process which increases the stability of this suspension by reducing the surface charge of the suspended particle. It is realized that changing the strongly dispersing conditioning agents used during extraction will reduce settling time. The slow consolidation of MFT has been attributed to a number of factors. The presence of mixed layer clays or clays weathered or degraded by caustic soda action and coated with bitumen can form sterically stabilized gel-like structure in tailings which prevent settling (Hooshiar Fard, 2011). It is agreed that as the particle size of clays decreases the degree of gelation increases (Kotlyar, Sparks, LePage, & Woods, 1998). Low absolute values of the repulsive potential for these fines are claimed to promote this behaviour (Van Olphen, 1991). The ultra-fines ($< 0.2 \mu\text{m}$) are known to settle down to 3 wt/vol% content which is known as the critical gelation concentration (CGC), regardless of their initial concentration. Once the CGC is reached they form gel structure and further sedimentation is difficult (Mercier et al., 2012). The water holding capacity of minerals in MFT is due to these gel-like structures which consists of water trapped in the network of fine particles. Formation of “Iron-Organic complex” was also suspected to be responsible for water holding capacity of MFT (Majid & Sparks, 1996). The ferric ions were believed to bind the organic material to the clays, affecting their surface properties. But this theory was later disregarded. The role of ultra-fines was emphasized to be responsible for MFT water holding capacity and gelation by numerous researches. The ultra-fines that are naturally delaminated and form flocs in the tailings in presence of sodium and bicarbonate ions, are considered to contribute 90% to its water holding capacity. The existence of biwettable clays is also known to accelerate gelation and stabilization of bitumen emulsion which increases tailings viscosity. Bitumen also bonds the coarser biwettable clays, thickening and strengthening the ultra-fine gel structure. It was also realized that clays such as kaolinite and illite were an order of magnitude smaller in oil sands also contributed to the problem (Fine Tailings Fundamental Consortium and Alberta. Dept. of Energy. Oil Sands and Research Division and others, 1995).

2.2 Role of bitumen in tailings

Oil sands tailings have a complex settling behaviour. Presence of residual bitumen in tailings further complicates the situation (Chow, McKenna, Win, & Journault, 2014). Clay behaviour in the presence of residual bitumen is unclear and studies need to be performed to understand the nature of the clay/bitumen interface in tailings (J. D. Scott, Dusseault, & Carrier, 1985). Not only bitumen recovery from the oil sands is inversely related to the amount of the organic-coated minerals in the raw oil sands ore (Adegoroye et al., 2010)(Dang-Vu et al., 2009a) but the interaction of biwetttable and hydrophobic clay with bitumen also hinders consolidation of tailings (Dang-Vu et al., 2009b). The gel formation in tailing is attributed to require clay-bound organic matter, free bitumen, and well-dispersed clay. This situation is easily created due to mixing of the slurry at low stresses (Ignasiak, Kotlyar, Longstaffe, Strausz, & Montgomery, 1983). The SEM images obtained by Mikula et al. (R. J. Mikula & Munoz, 2000) have shown the presence of free bitumen droplets of 1-10 μm in size in MFT along with bitumen attached to the edges of clays, possibly contributing to the tailings structure which impedes further settling. Adsorption of bitumen on fines ($<2 \mu\text{m}$) and ultra-fines ($<0.2 \mu\text{m}$) alters the clay surface charge, expandability and cation exchange capacity (Clementz, 1976)(M. Osacky et al., 2013). This bitumen-clay interaction complicates the understanding of these clays based on the information available for the individual clay types (Johnston, 2010). The percentage of hydrophobic solids is found to be higher in poor quality ores (Dang-Vu et al., 2009a). The oil sands clays are also believed to be thinner compared to the reference clays hence giving them higher specific surface area and more reactive surfaces.

Impact of presence of bitumen on shear strength, trafficability, waste containment requirements, initial densification, hydraulic conductivity, consolidation and post reclamation settlement of tailings has been studied but more research needs to be performed for most of these factors. Research conducted by Majid et al. (Majid & Sparks, 1993) showed that once bitumen is removed from MFT, the solids showed better dewatering capabilities compared to the sample before bitumen removal. These results have led to the understanding high water retention of MFT is promoted due to the presence of residual bitumen. But the degree of its contribution is not clearly understood. The polar molecules such as asphaltenes and resins in bitumen are also believed to retain significant water layers which adds to the water holding capacity of MFT (Ignasiak et al.,

1983). Residual bitumen in tailings is also known to reduce its draining capacity. It also reduced the hydraulic conductivity of tailings (J. D. Scott et al., 1985). Absence of bitumen would also increase the rate of densification. Since bitumen is about 10^6 times more viscous compared to water, it block pores of clays, creates a torturous flow path and reduces permeability of MFT by about 10 to 100 times (Ignasiak et al., 1983), thus preventing the release of water and further consolidation of MFT (Fine Tailings Symposium (1993 : Edmonton, 1993).

While researches have proved that removal of bitumen from MFT improves their consolidation (Majid & Sparks, 1996), some researches also argue that fugitive bitumen binds to fines, bridging them and increase their settling rate (J. D. Scott et al., 1985). Effect of fugitive bitumen on flocculants is also not completely understood. While removal of bitumen from MFT to a certain degree showed improvement in flocculation and settling performance for 0.45 – 0.18 wt% bitumen but further removal of bitumen showed detrimental effect on flocculation (Klein, Harbottle, Alagha, & Xu, 2013).

2.3 Optical microscope

Optical equipment such as microscopes deviate and focus light within the electromagnetic spectrum with different types of lens. Most current commercial microscopes are compound microscopes with an array of lenses within the optic tube. The illumination beam paths is such that the specimen is placed between the light source and the objective lens. This type of configuration is known as transmitted light or bright field illumination. Optical microscope utilizes phenomenon such as transmission, reflection, refraction, diffraction and polarization to their benefit. In case of microscope utilizing transmission, a light source is added to make the specimen visible. For an accurate image formation from the specimen, it is important to collect most of the diffracted light. This can be achieved by replacing the space between objective and substrate with higher refractive index material such as water (1.33) or oil (1.51) and hence objective lens with high numerical aperture. Numerical aperture (NA) is measure of the objective's capability to gather light and resolve fine details in the sample.

$$\text{Numerical Aperture (NA)} = \eta (1) \times \sin (\theta)$$

(Equation 2.3.1)

Where n is the refractive index of immersion oil and θ is $\frac{1}{2}$ of the objective lens angular aperture. Better resolution can be achieved with higher NA (Seward, 2010). Hence resolution is a function of the ability of a lens to gather light. The smallest features that can be distinguished within the sample is known as Abbe resolution. It is defined with the help of Rayleigh equation:

$$\text{Resolution} = 1.22 \times (\lambda / 2NA)$$

(Equation 2.3.2)

Where λ is the wavelength of incident light (Krishnan, Varma, & Mayor, 2001). This equation can also be depicted as follows:

$$D \times NA = 1.22 \times \lambda$$

(Equation 2.3.3)

Where D is the diameter of Airy disks. For high numerical objects smaller Airy disk are seen. Airy disks are patterns formed by various points in the sample due to diffraction and scattering of light while passing through these points. The distance and intensity of these airy disks limit the resolution. The overall magnification equation for a microscope is shown below:

$$M = l \times M_1 \times M_2 / 250 \text{ mm}$$

(Equation 2.3.4)

Where l is projection/ tube length which is usually 250 mm and M_1 and M_2 are magnification of objective and ocular. The 250 mm is usually the minimum distance of vision. Magnification is a function of the number of lenses in the microscope to a certain degree.

Depth of focus or z-plane resolution is also an important consideration. This term shows the ability to produce a sharp image from a non-flat surface. It is defined by the following equation:

$$\text{DOF} \approx \lambda / NA$$

(Equation 2.3.5)

Though lens are manufacture with utmost precision, they suffer from defects such as spherical aberration where the peripheral rays and axial rays have different focal points. This causes the

image be blurry and slightly out of focus. Another type of lens defect is the chromatic aberration which comes into play due to wide bandwidth of light. The axial impact of this aberration results in blue light being refracted to the greatest extent followed by green and then red light. The lateral impact of this aberration results in chromatic difference of magnification where the blue image of a detail are slightly larger than the green image or the red image, hence resulting in color rings around the details of the sample. A converging lens can be combined with a weaker diverging lens, to nullify the influence of chromatic aberration. Difference in the refractive index within the sample also create artifacts in the resulting image due to different angles of refraction at different points. Interference fringe, are also a common defect in imaging. Bright or dark band which are created due to this effect are caused by beams of incident light that are in phase or out of phase with each other. This comes into play due to the wave nature of light. If the crests and troughs of two light beam are out of phase then either constructive or destructive interference occurs. If a beam of light is monochromatic and is passed through two narrow slits then instead of forming two patches of overlapping light, they will form interference fringes, which is a pattern of evenly spaced alternating bright and dark bands (Harris, Hill, & Vaughan, 1994).

Optical microscope are the simple and relatively cheaper to use but have limited magnification possibility restricted by optical diffraction limit. These microscope also provide relative low contrast images. But the resolution can be marginally increased by reducing the incidence light wavelength to the ultraviolet range.

2.4 Fluorescence microscope

Fluorescence occurs when a photon with energy $h\nu_{\text{ex}}$ from an illumination source is absorbed by the fluorophore so as to excite it to an electronic excited singlet state (S_1'). The fluorophore stays at this excited state for about 1–10 nanoseconds. From here to it relaxes down to the ground singlet state (S_1). This fluorophore then comes back to ground state (S_0) after emitting a photon of energy $h\nu_{\text{em}}$. This phenomenon is depicted by the Jablonski diagram. During this process some energy is lost due to various phenomenon such as vibrational losses. Since some energy is lost hence the emitted photon is of lower energy and higher wavelength compared to the excitation photon. This energy difference is known as Stokes shift. The properties which decide the quality of a fluorophore are its ability to absorb light energy at a given wavelength, the percentage of absorbed light that produces fluorescence emission vs. other non-radiative losses and the chemical stability

of the fluorophore in the excited state (Webb & Brown, 2013). As the fluorophore can emit many photon during this process and does not usually get permanently destroyed hence fluorescence techniques have high sensitivity. Fluorescence is generally observed in polyaromatic hydrocarbons and heterocyclic hydrocarbons. Each material has a specific excitation and emission spectrum (Mondal, 2014). The materials which do not show natural fluorescence can be tagged with fluorescent dyes to help observe them.

Fluorescence microscope is a type of optical microscope which exploits the fluorescence phenomena of material. *Figure 2-2* shows the schematic for Fluorescence microscope. Fluorescence microscope illuminates the sample with specific wavelengths which excites the fluorophores in the sample, and then only allows the emitted fluorophores to reach the camera. It separates the excitation and emission wavelengths using the filters to block or pass specific wavelength. It either requires a wide wavelength light source such as xenon lamp or multiple specific wavelength lasers. Efficient and exclusive capture of emitted light is handled via a filter cube with an excitation filter, dichroic mirror and an emission filter. Digital camera captures real-time images and transfers it to the computer for further image processing. Advantages of this microscope are, its high contrast, sensitivity and selectivity.

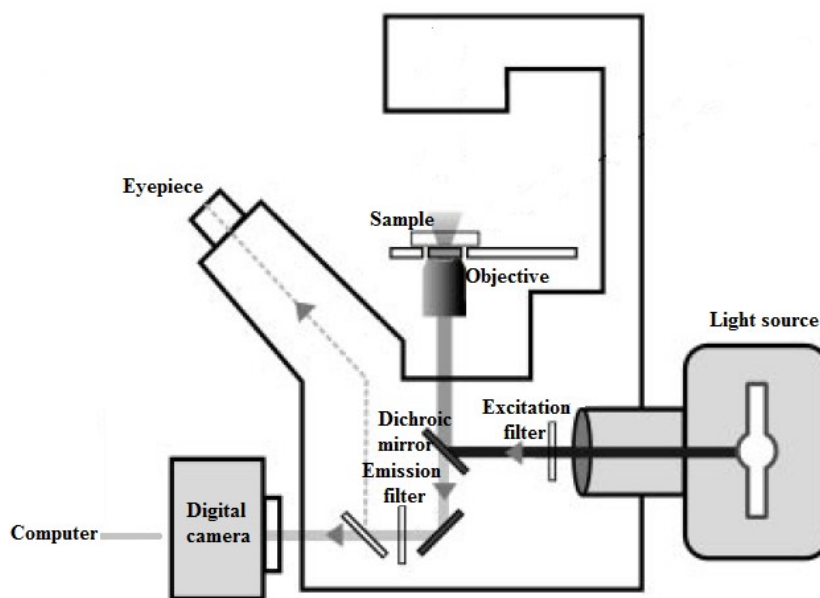


Figure 2-2: Schematic of fluorescence microscope (Dobrucki, 2013)

High contrast images can be obtained due to selective excitation of fluorophores against the black background. Specificity and selectivity is achieved using dyes that attach to a specific molecule or site. In case of substances showing natural fluorescence, excitation can be achieved only at a precise wavelength. Highly sensitive cameras and detector can be employed which can even detect a single molecule in the sample (Dobrucki, 2013).

Epifluorescence microscopes are common type of fluorescence microscope where illumination and emission path of light is through the same objective lens. A semi-transparent mirror directs the light through objective which also is a condenser. It is also common for these epifluorescence microscopes to be inverted, meaning the objective is below the sample. On inverted microscopes, specimen is placed above the objective lens and hence observed from below. This makes accessing and manipulating the sample quite convenient. It is also more suitable in case of liquid samples. Since two functions of illumination and image capturing are being done by a single objective lens of the microscope the alignment of light path is also perfect. It also ensures that only reflected excitation light and emitted light are collected by the objective. This enhances the signal-to-noise ratio (Ishikawa-Ankerhold, Ankerhold, & Drummen, 2012).

Confocal fluorescence microscopy technique gives 3D images by suppressing any signal coming from out-of-focus planes. This can be done by using a pinhole in front of the detector which only allows light from an in-focus plane while the light from out-of-focus planes is mostly blocked. In this method a focused spot of illuminating light scans across the sample. The emitted light passing through the detector pinhole is then transformed into electrical signals collected by a PMT tube and image built from this output displayed on a computer monitor screen. Confocal microscopy offers several advantages such as controlled depth of field, elimination of out-of-focus noise, capability to work with specific sections of a thick samples and some improvement in improvement axial and lateral resolution.

2.5 Total Internal Fluorescence reflection (TIRF) microscope

Different mechanisms are applied to restrict the excitation and detection of fluorophores to a thin region of the sample and background fluorescence from outside the focal plane. This drastically improves the signal-to-noise ratio, and spatial resolution of the specimen. TIRF is a super-resolution technique that exceeds the light microscope limit by employing the unique properties of an induced evanescent wave or field generated which illuminates the sample region immediately

adjacent to the glass-sample interface. Total internal reflection of incidence light takes place at the interface between high refractive index substrate and low refractive index sample. This phenomena is governed by Snell's Law:

$$\eta (1) \times \sin \theta_1 = \eta (2) \times \sin \theta_2$$

(Equation 2.5.1)

Where $\eta (1)$ is the higher refractive index (usually glass) and $\eta (2)$ is the lower refractive index (usually water). The angle of the incident is θ_1 , while the refracted beam angle is θ_2 . The incidence light may encounters the interface at an angle such that the refracted angles is parallel to the interface, such angle of incidence is called critical angle θ_c .

By manipulating the Snell's law, an equation with critical angle term can be obtained:

$$\eta (2) = \eta (1) \times \sin \theta_c$$

(Equation 2.5.2)

Hence, critical angle can be expressed as:

$$\theta_c = \sin^{-1} \eta (2) / \eta (1)$$

(Equation 2.5.3)

As for the total internal refraction to take place, the incidence wave needs to approach from higher refractive index such as glass ($\eta (1) \sim 1.55$) to lower refractive index medium such as water based emulsion ($\eta (2) \sim 1.33$). For these values of refractive indices, the critical angle is about 61° . Major reason for popularity of the glass water interface is because glass substrate remains transparent in both visible and ultraviolet light and most biological samples are water based. Samples with slightly higher refractive index than water will give lower evanescent wave penetration and hence higher axial resolution (H. Wang & Nann, 2011).

As the incidence angle of illuminating light approaches the critical angle, the refracted light intensity diminishes and the intensity of reflected light increase. At angles above critical angles all of the incidence light is reflected. The incidence light does not travel into the sample, but there is an electromagnetic field termed as evanescent field is generated near the interface, which is

capable of exciting fluorophores. As seen in *Figure 2-3*, evanescent wave is generated parallel to the substrate–sample interface. Evanescent means vanishing, but it does not vanish with time but with distance from the interface between substrate–sample. The intensity of evanescent waves decays exponentially with distance from the interface at which it is generated (Sako & Uyemura, 2002). It decays within a distance much shorter than the wavelength dimension. The energy as a function of distance from the interface can be expressed as follows:

$$E(z) = E(0) \exp(-z/d)$$

(Equation 2.5.4)

Where $E(z)$ are the energy values as a function of z which is the distance perpendicular to the interface, $E(0)$ is the energy at the interface and d is the depth to which evanescent wave penetrates. The penetration depth, d is dependent on the wavelength of the incident light λ_i , the angle of the incident is θ_1 , and the refractive indices of the sample $\eta(2)$ and substrate $\eta(1)$. The equation for penetration depth of the evanescent wave is as follows:

$$d = \lambda_i / 4\pi \times (\eta(1)^2 \sin^2 \theta_1 - \eta(2)^2)^{-1/2}$$

(Equation 2.5.5)

The optical section thickness of this illumination is about one-tenth that produced by confocal fluorescence microscopy. As the fluorophores in the bulk of the sample are not excited hence most of the background noise is eliminated, giving a high signal-to-noise ratio compared to conventional epifluorescence microscope. Since the evanescent wave illumination is “compressed” due to its exponential decay, helps to increase the resolution in the direction of its propagation.

Depending on the incidence angle, the depth to which this evanescent wave travels ranges approximately from $1/10\lambda - \lambda_i$, where λ_i is the excitation light wavelength in vacuum (Axelrod, 2014)(Aguilera, Montoya, Primm, & Varela-Ramirez, 2006). It can illuminate thin regions, giving axial resolution as low as 60-100 nm, which is comparable to electron microscope (Shen et al., 2014). The brightness of fluorophores is proportional to source intensity and numerical aperture of objective. It is also dependent on distance of fluorophore from glass. TIRF gives good depth discrimination (Steyer & Almers, 2001).

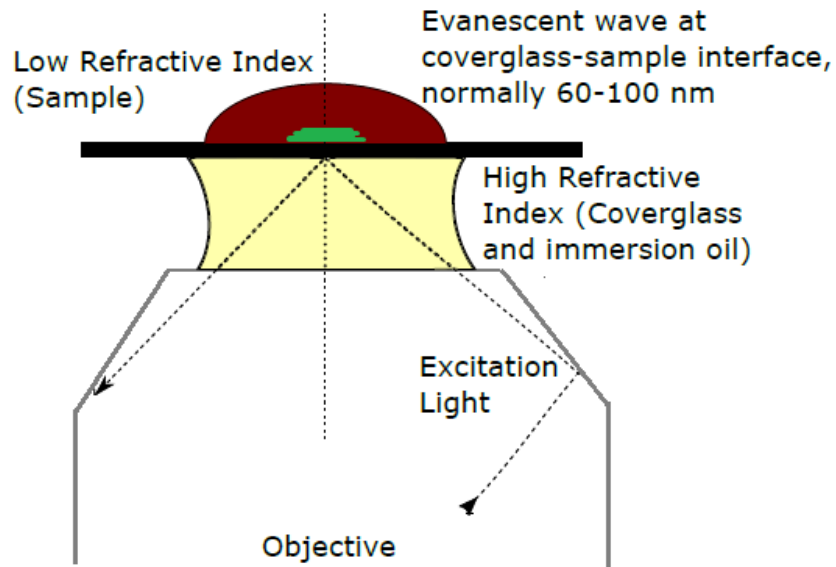


Figure 2-3: Incident light is focused at an angle greater than critical angle so that it is completely reflected. But an evanescent wave is generated near sample-coverglass interface.

Two common configuration available are the prism type and lens type. The prism type gives larger field of view but gives restricted access to the sample and is not available commercially. Whereas the lens type configuration which is available commercially allows free sample access and better quality images (Schneckenburger, 2005). TIRF technique can be easily implemented with lens type configuration using a high numerical aperture objective and laser source in an epifluorescence microscope (Krishnan et al., 2001). This is because, objective with high numerical aperture is capable of gathering light scattered at high angles from objective centerline. The relationship between numerical aperture and incidence angles is shown as follows:

$$\text{Numerical Aperture (NA)} = n \sin \theta$$

(Equation 2.5.6)

Where NA is the numerical aperture of the objective, n represents refractive index, and θ is 1/2 the objective angular aperture. Hence for total internal reflection to occur at the interface, the numerical aperture of the objective must exceed the refractive index of sample by substantial margin preferably above 1.4. The brightness of the image which is the efficiency at which the light

is being transmitted by the objective is dependent on the NA and the magnification of the lens as follows:

$$\text{Brightness} \propto \text{NA}^4 / m^2$$

(Equation 2.5.7)

Where m is the magnification of the lens. TIRF is commonly used for selective near surface excitation. By varying the excitation light angle the concentration of fluorophores can also be inferred as a function of distance from interface. Varying the excitation light along with the laser intensity on a coated surface can display resonance behavior which gives information about the coating thickness, refractive index and lateral surface non-uniformity (Axelrod, 2014). TIRF is sometimes combined with other techniques such as bright-field, epifluorescence, dark-field and differential interference contrast illumination on the same equipment which simplifies simultaneously observing a sample with different techniques.

2.6 Electron microscopy

In case of optical microscopes, the resolution is usually limited by the optical diffraction limit decided by the wavelength of illuminating light. To overcome this limitation electron microscopes use electrons with wavelength much lower than light to illuminate the sample. The electron beams are focused at the sample using electromagnetic coils and the emitted electron and photons are collected by a detector. These microscopes can give up to nanoscale resolution. Various types of electron microscopes such as Transmission Electron Microscope (TEM), Scanning Electron Microscope (SEM) and Cryo-SEM are employed to study different aspects of sample. TEM provides higher resolution compared to SEM and can provide information such as morphology, crystallization, stress and magnetic domains (Stolojan, 2015). But SEM can provide topography and surface composition of the sample (Khursheed, 2011). TEM is also expensive compared to SEM and requires more sample preparation.

SEM requires sample to be coated with an insulating material to prevent the sample from getting destroyed due to charging (R. J. Mikula & Munoz, 2000). TEM requires sample to be thinned to about 100 nm in order to be imaged which is a tedious process. Both these techniques require depressed pressure and temperature for imaging (Hooshiar, Uhlik, Ivey, Liu, & Etsell, 2012).

2.7 Image Acquisition and Processing

Image acquisition using TIRF microscope involves acquiring 2-D focal plane images at different sampling heights (z) using high speed camera. The 2-D focal plane images have finite depth of field. Depth of field is the depth of sample thickness that is in sharp focus. For TIRF images this can be adjusted using different incidence angles of laser. Since most image features in a sample are three-dimensional in nature, it is meaningful to construct a 3-D image by stitching several 2-D images. 3-D images can be constructed by stitching several 2-D images either using TIRF software or external software such as imageJ or python. Overlapping feature in adjacent images help the image processing software to stitch the images together.

The TIRF images are in 8-bit RGB format containing red, green and blue channels. Each channel containing 256 possible brightness values. Since bright features in these images can never contain an abrupt boundary, the boundary of the feature needs to be distinguished using segmenting. The easiest way to do this is using thresholding. Thresholding converts the image into a binary image using a chosen algorithms.

For bitumen samples, the images show fluorescing areas in green color while everything else is black. Hence the green channel is extracted from these images. The green channel image can then segmented using thresholding into binary image where black pixels (or foreground) are bitumen and white pixels (or background) are non-fluorescing features (clays and water). The resultant binary image, with 'TRUE' values for pixels at which bitumen is present (fluorescence was observed), and 'FALSE' values where it is absent. Thresholding helps in distinguishing where the fluorescing bitumen ends and non-fluorescing features start.

While calculating the threshold values, the adjacent layers up to a thickness of the resolution limit along z axis ($\sim 450\text{nm}$) are considered. This is done because features from other planes within the diffraction limit also leave impressions over current plane. Hence, the threshold for each plane is computed for a sub-block of the 3-D image. This ensures fidelity in tomographic reconstruction at deeper planes, even for a decreasing illumination intensity in TIRF. But for reconstruction of small particles, with near uniform illumination of all planes, a fixed threshold on normalized 3D image can be used.

After segmenting, the indices of 'TRUE' pixels are extracted from the binary 3D image. These pixels are then converted into physical coordinates by multiplying the x-y plane indices with distance per pixel (~210 nm for 100X objective) and the z direction indices by distance per layer in acquired z stack. The physical coordinates are then stitched together to get 3D tomographic reconstruction.

2.8 References

- Adegoroye, A., Wang, L., Omotoso, O., Xu, Z., & Masliyah, J. (2010). Characterization of organic-coated solids isolated from different oil sands. *Canadian Journal of Chemical Engineering*, 88(3), 462–470. doi:10.1002/cjce.20294
- Aguilera, R. J., Montoya, J., Primm, T. P., & Varela-Ramirez, A. (2006). Green Fluorescent Protein as a Biosensor for Toxic Compounds. *Reviews in Fluorescence* (Vol. 3). doi:10.1007/0-387-33016-X
- Axelrod, D. (2014). Evanescent Excitation and Emission. *Fluorescence Microscopy: Super-Resolution and other Novel Techniques*. Elsevier Inc. doi:10.1016/B978-0-12-409513-7.00001-4
- Caughill, D. L., Morgenstern, N., & Scott, J. (1993). Geotechnics of nonsegregating oil sand tailings. *Canadian Geotechnical Journal*, 30(5), 801–811.
- Chow, R., McKenna, G., Win, S. M. K., & Journault, J. (2014). Recovery of bitumen from oil sands tailings streams and deposits: Potential opportunities and benefits. Retrieved from http://www.ai-ees.ca/media/12375/aitf_bgc_bitumen_from_tailings_for_ae-ees_and_cosia_dec__2013.pdf
- Clementz, D. M. (1976). Interaction of petroleum heavy ends with montmorillonite. *Clays and Clay Minerals*, 24(6), 312–319. doi:10.1346/CCMN.1976.0240607
- COSIA. (n.d.-a). Composite Tailings Process Addresses Challenging Tailings Material. Retrieved from <http://www.cosia.ca/uploads/files/Media Resources/Media Kit/Composite Tailings Process Addresses Challenging Tailings Material.pdf>

- COSIA. (n.d.-b). Tailings Reduction Technology. Retrieved from <http://www.cosia.ca/tailings-reduction-technology>
- Dang-Vu, T., Jha, R., Wu, S. Y., Tannant, D. D., Masliyah, J., & Xu, Z. (2009a). Wettability determination of solids isolated from oil sands. *Colloids and Surfaces A: Physicochemical and Engineering Aspects*, 337(1-3), 80–90. doi:10.1016/j.colsurfa.2008.11.055
- Dang-Vu, T., Jha, R., Wu, S.-Y., Tannant, D. D., Masliyah, J., & Xu, Z. (2009b). Effect of solid wettability on processability of oil sands ores. *Energy Fuels*, 23(5), 2628–2636. doi:10.1021/ef9000117
- Dobrucki, J. W. (2013). *Fluorescence Microscopy. Fluorescence Microscopy- From Principles to Biological Applications*. doi:10.1002/9783527671595
- Fine Tailings Fundamental Consortium and Alberta. Dept. of Energy. Oil Sands and Research Division and others. (1995). *Advances in oil sands tailings research*. Edmonton: Alberta Dept. of Energy.
- Fine Tailings Fundamentals Consortium Alberta Energy. (1995). *Advances in oil sands tailings research*. Edmonton, Alta: Alberta Dept. of Energy.
- Fine Tailings Symposium (1993 : Edmonton, A. (1993). *Oil Sands : Our Petroleum Future Conference Proceedings*.
- Gray, M. R. (1998). *Extraction and upgrading of oilsands bitumen: Intensive short course*. University of Alberta Edmonton.
- Gregory, J., & Barany, S. (2011). Adsorption and flocculation by polymers and polymer mixtures. *Advances in Colloid and Interface Science*, 169(1), 1–12. doi:10.1016/j.cis.2011.06.004
- Harris, M., Hill, C., & Vaughan, J. (1994). Optical helices and spiral interference fringes. *Optics Communications*, 106(4), 161–166.
- Hooshar, A., Uhlik, P., Ivey, D. G., Liu, Q., & Etsell, T. H. (2012). Clay minerals in nonaqueous extraction of bitumen from Alberta oil sands: Part 2. Characterization of clay minerals. *Fuel Processing Technology*, 96, 183–194. doi:10.1016/j.fuproc.2011.10.010

- Hooshiar Fard, M. A. (2011). Characterization of Clay Minerals in the Athabasca Oil Sands in Water Extraction and Nonaqueous Solvent Extraction Processes (PhD Thesis). University of Alberta.
- Ignasiak, T. M., Kotlyar, L., Longstaffe, F. J., Strausz, O. P., & Montgomery, D. S. (1983). Separation and characterization of clay from Athabasca asphaltene. *Fuel*, 62(3), 353–362.
- Ishikawa-Ankerhold, H. C., Ankerhold, R., & Drummen, G. P. C. (2012). Advanced Fluorescence Microscopy Techniques—FRAP, FLIP, FLAP, FRET and FLIM. *Molecules*, 17(12), 4047–4132. doi:10.3390/molecules17044047
- Johnston, C. T. (2010). Probing the nanoscale architecture of clay minerals. *Clay Minerals*, 45(3), 245–279. doi:10.1180/claymin.2010.045.3.245
- Kaura, A. (2014). Understanding and Developing New Methods for Treating Oil Sands Tailings. University of Alberta.
- Khursheed, A. (2011). Scanning Electron Microscope Optics And Spectrometers. World Scientific Publishing Company.
- Klein, Colin. Effect of Residual Bitumen on Polymer-assisted Flocculation of Fluid Fine Tailings. Master of Science Dissertation, University of Alberta, Canada. (2014). University of Alberta, Canada.
- Kotlyar, L., Sparks, B., LePage, Y., & Woods, J. (1998). Effect of Particle Size on Clay Flocculation Behavior of Ultra-Fine Clays in Salt Solutions. *Clay Minerals*, 33(1), 103–107.
- Krishnan, R. V, Varma, R., & Mayor, S. (2001). Fluorescence methods to probe nanometre-scale organization of molecules in living cell membranes. *J. Fluor.*, 11(3), 211–226.
- Majid, A., & Sparks, B. D. (1993). Dewatering of Athabasca oil sands fine tails using agglomeration techniques. In Proceedings. Fine Tailings Symposium, Oil Sands Our Petroleum Future. Conference, 1993.

- Majid, A., & Sparks, B. D. (1996). Role of hydrophobic solids in the stability of oil sands fine tailings. *Fuel*, 75(7), 879–884.
- Majid, A., & Sparks, B. D. (1996). Role of hydrophobic solids in the stability of oil sands fine tailings. *Fuel*, 75(7), 879–884.
- Matthews, J., Shaw, W., MacKinnon, M., & Cuddy, R. (2002). Development of composite tailings technology at Syncrude. *International Journal of Surface Mining, Reclamation and Environment*, 16(1), 24–39.
- McFadyen, D. (2009). Directive 074: Tailings Performance Criteria and Requirements for Oil Sands Mining Schemes. Energy Resources Conservation Board, Calgary, AB, Canada.
- Mercier, P. H. J., Ng, S., Moran, K., Sparks, B. D., Kingston, D., Kotlyar, L. S., ... McCracken, T. (2012). Colloidal Clay Gelation: Relevance to Current Oil Sands Operations. *Petroleum Science and Technology*, 30(April 2015), 915–923. doi:10.1080/10916466.2010.495959
- Mikula, R. J., & Munoz, V. a. (2000). Characterization of emulsions and suspensions in the petroleum industry using cryo-SEM and CLSM. *Colloids and Surfaces A: Physicochemical and Engineering Aspects*, 174, 23–36. doi:10.1016/S0927-7757(00)00518-5
- Mikula, R., & Omotoso, O. (2006). Role of Clays in Controlling Oil Sands Tailings Processing Behaviour in Oil Sands Processing. *Clay Science*, 12(2), 177–182. doi:10.11362/jessjclayscience1960.12.Supplement2_177
- Mondal, P. P. (2014). Fundamentals of fluorescence microscopy: exploring life with light. *Statewide Agricultural Land Use Baseline 2015 (Vol. 1)*. Dordrecht: Springer.
- Osacky, M., Geramian, M., Dyar, M. D., Sklute, E. C., Valter, M., Ivey, D. G., ... Etsell, T. H. (2013). Characterisation of petrologic end members of oil sands from the Athabasca region, Alberta, Canada. *The Canadian Journal of Chemical Engineering*, 9(June), 1–14. doi:10.1002/cjce.21860
- Powter, C., Biggar, K., Silva, M., McKenna, G., & Scordo, E. (2011). Review of oil sands tailings technology options.

- Sako, Y., & Uyemura, T. (2002). Total Internal Reflection Fluorescence Microscopy for Single-molecule Imaging in Living Cells Total internal reflection fluorescence microscopy for detecting single-molecules in living cells. *Cell Structure and Function*, 27, 357–365. doi:10.1247/csf.27.357
- Schneckenburger, H. (2005). Total internal reflection fluorescence microscopy: Technical innovations and novel applications. *Current Opinion in Biotechnology*, 16(1 SPEC. ISS.), 13–18. doi:10.1016/j.copbio.2004.12.004
- Scott, J. D., Dusseault, M. B., & Carrier, W. D. (1985). Behaviour of the clay/bitumen/water sludge system from oil sands extraction plants. *Applied Clay Science*, 1(1-2), 207–218.
- Seward, G. H. (2010). *Optical Design of Microscopes*. Bellingham, Wash. (1000 20th St. Bellingham WA 98225-6705 USA): SPIE.
- Shen, H., Huang, E., Das, T., Xu, H., Ellisman, M., & Liu, Z. (2014). TIRF microscopy with ultra-short penetration depth. *Optics Express*, 22(9), 10728–34. doi:10.1364/OE.22.010728
- Steyer, J. a, & Almers, W. (2001). A real-time view of life within 100 nm of the plasma membrane. *Nature Reviews. Molecular Cell Biology*, 2(4), 268–275. doi:10.1038/35067069
- Stolojan, V. (2015). *Nanometrology Using the Transmission Electron Microscope*. Morgan & Claypool Publishers Institute of Physics.
- Van Olphen, H. (1991). *An introduction to clay colloid chemistry: for clay technologists, geologists, and soil scientists*, 2nd ed. Malabar, FL: Krieger Publishing Co.
- Wang, H., & Nann, T. (2011). *Fluorescence Spectroscopy in Biology*. (O. S. Wolfbeis, Ed.) *Upconverting Nanoparticles* (Vol. 7). Springer. doi:10.1007/4243_2010_8
- Webb, D. J., & Brown, C. M. (2013). *Epi-Fluorescence Microscopy*. doi:10.1007/978-1-62703-056-4_2

Chapter 3: Total Internal Reflection Fluorescence Microscopy to Investigate the Distribution of Residual Bitumen in Oil Sands Tailings¹

3.1 Introduction

Oil sands consist of mostly water, minerals, and bitumen. The amount of oil sands deposits in Canada make it a country with the third largest oil reserves in the world are mainly found in the Athabasca, Cold Lake and Peace River region of Alberta. Bitumen from oil sands has a higher viscosity, higher density, higher quantity of heavy metals, and lower hydrogen/carbon ratio in comparison to conventional crude oil (Masliyah, Jacob H. (Jacob Heskell), Xu, Z. (Zhenghe), Czarnecki, Jan A. (Jan Adam), Dabros, 2011). Oil sands are recovered from the ground by either surface mining or in situ technology. About 10% of the oil sands reserves can be recovered using surface mining technique, which is much cheaper than the in situ technique (Sparks, Kotlyar, Carroll, & Chung, 2003). Surface mining involves removing the overburden, digging the exposed oil sands, transporting the oil sands to the crushers, and then sending the crushed oil sands to the extraction plants. The hot water extraction process is one of the techniques used for extracting oil from the oil sands. In this technique, oil sands are mixed with hot water to form a slurry, which is then sent to a separation vessel. Here, the slurry separates into 3 layers: a bottom layer consisting of sand, a middle layer consisting of clay, water and some sand and a top layer called a bitumen froth. The waste by-product from the extraction process consisting of sand, clay, fine silt, and water are called tailings. It is sent to tailing ponds to allow sedimentation. Tailings are known to contain contaminants, such as naphthenic acids (A. C. Scott, MacKinnon, & Fedorak, 2005), polycyclic aromatic hydrocarbons (Folwell, McGenity, Price, Johnson, & Whitby, 2014), mercury, and trace metals (Holden, Haque, Mayer, & Ulrich, 2013), which are harmful to the environment and therefore need to be mitigated. Over time, a top water layer is formed in the tailing ponds, which is recycled back to the extraction plant. The bottom layer eventually forms mature fine tailings (MFT), which has a solid content up to 30% (w/w) with the remainder being water. Further dewatering of MFT can take as long as 100 years (Masliyah, Jacob H. (Jacob Heskell), Xu, Z. (Zhenghe), Czarnecki, Jan A. (Jan Adam), Dabros, 2011). Strict government regulations, economic constraints, and negative environmental impacts have urged industries to increase the

¹ A version of this chapter has been published in ACS Publications, Energy & Fuels journal.

speed of tailings dewatering, water recycle, and tailings land reclamation. Various methods, such as adding gypsum to increase clay consolidation (Wang, Feng, Xu, & Masliyah, 2010), adding flocculants (Yang, Qian, & Shen, 2004)(Mpofu, Addai-Mensah, & Ralston, 2003)(Li, Long, Xu, & Masliyah, 2008), filtration, and drying, have been explored to increase the separation rate of water from solids to no avail. To increase the MFT settling rate, it is important to understand its components, their surface chemistry, and their surface interactions. Substantial research is being conducted in this area. The slow settling of MFT and lowered bitumen recovery are mainly attributed to factors such as pH (Masliyah et al., 2004), small clay particle size (Boxill, 2011), negative surface charge of clay (Tamiz Bakhtiari et al., 2015), gelation of clay (Mercier et al., 2012), types of clays (Boxill, 2011)(Yin & Miller, 2012)(H. A. W. Kaminsky, Etsell, Ivey, & Omotoso, 2009)(J. Liu, Xu, & Masliyah, 2004) and presence of the residual bitumen in tailings (Masliyah, Jacob H. (Jacob Heskell), Xu, Z. (Zhenghe), Czarnecki, Jan A. (Jan Adam), Dabros, 2011)(Sparks et al., 2003)(“Klein, Colin. Effect of Residual Bitumen on Polymer-assisted Flocculation of Fluid Fine Tailings. Master of Science Dissertation, University of Alberta, Canada,” 2014). Residual bitumen ends up in tailings as a result of the bitumen–clay attachment in oil sands, which impairs the bitumen–air attachment during froth flotation (Dang-Vu et al., 2009b)(Muñoz, Kasperski, Omotoso, & Mikula, 2003)(Hooshier et al., 2010). A significant percentage of oil sands clays has organic material physically or chemically adsorbed onto its surface (Sparks et al., 2003)(H. A. W. Kaminsky et al., 2009)(J. Liu et al., 2004)(Marek Osacky, Geramian, Ivey, Liu, & Etsell, 2015).

These clay–organic interactions take place at a 1–10 nm scale, but they impact the recovery and upgrading of bitumen on a much larger scale (Johnston, 2010). As a result of the nanoscale of these interactions and a lack of contrast, a bright-field optical microscope cannot be used to study these interactions. Various other techniques, such as X-ray photoelectron spectroscopy (XPS) (Marshall, Kingston, Moran, & Mercier, 2013), X-ray fluorescence (XRF) microscopy (M. Osacky et al., 2013), atomic force microscopy (AFM) (J. Liu et al., 2004), transmission electron microscopy (TEM) (Hooshier et al., 2012), and scanning electron microscopy (SEM) (Hooshier et al., 2012), have been used to study bitumen, asphaltenes, and/or oil sands tailings. However, these techniques have various shortcomings. SEM and TEM require extensive sample preparation and working under vacuum and a depressed temperature, which can alter the tailings' chemical structure (Hooshier et al., 2012). Although AFM does not require much sample preparation, it reveals

surface features only, without material specificity (J. Liu et al., 2004). All of the above methods are not specific toward organic materials, and hence, the organic interaction with clay and their morphology is inferred but not known. However, fluorescence microscopy has shown excellent promise in imaging in situ bitumen/asphaltenes structures at the micrometer scale without much sample preparation (Bearsley, Forbes, & Haverkamp, 2004)(Hung, Castillo, & Reyes, 2004)(Franco et al., 2013)(Stasiuk, Gentzis, & Rahimi, 2000).

In this article we report use of fluorescence microscopy to image bitumen in MFT. The fluorescence phenomena in MFT are depicted in *Figure 3-1*, where a bitumen–clay interface is illuminated with a laser to excite bitumen molecules to higher energy levels. The excited molecules then emit fluorescence while returning to the ground level. Because only bitumen shows natural fluorescence (R. J. Mikula & Munoz, 2000)(Muñoz et al., 2003), the exact bitumen location on clay can be imaged using fluorescence microscopy. Because bitumen is dispersed throughout the bulk of the sample, fluorescence from deeper planes creates significant background noise, resulting in the loss of information from the focused region of the sample. For that reason, to image bitumen distribution in MFT, we adapted a Total Internal Reflection Fluorescence (TIRF), which until now was used only in cell biology research (Boulanger et al., 2014)(Knight, 2014)(Shen et al., 2014), to image bitumen distribution in MFT. In TIRF, the sample is illuminated by an evanescent wave near the surface, in contrast to illumination by a propagating wave in a conventional confocal fluorescence microscope. The illumination depth in TIRF can be made as small as 100 nm to eliminate the background noise, enabling imaging of detailed features. TIRF can provide information on bitumen distribution and the bitumen–clay interaction in tailings in real time, showing the effect of change in the temperature, pressure, flocculants, and pH (Amann & Pollard, 2001)(Nazemifard, Bhattacharjee, JH, & DJ, 2013).

First, we present the fluorescence excitation and emission spectra and show that it is possible to observe the bitumen–clay and bitumen–water interfaces using confocal epifluorescence microscopy. Then, we show the distribution of bitumen in MFT using TIRF images. Finally, using high resolution TIRF microscopy, we provide novel insights on the spatial location of residual bitumen on clay agglomerates in diluted MFT samples. Understanding bitumen distribution on clay and how it affects the clay–clay interaction in MFT is crucial for the development of more effective chemicals and processes to accelerate particle aggregation and sedimentation.

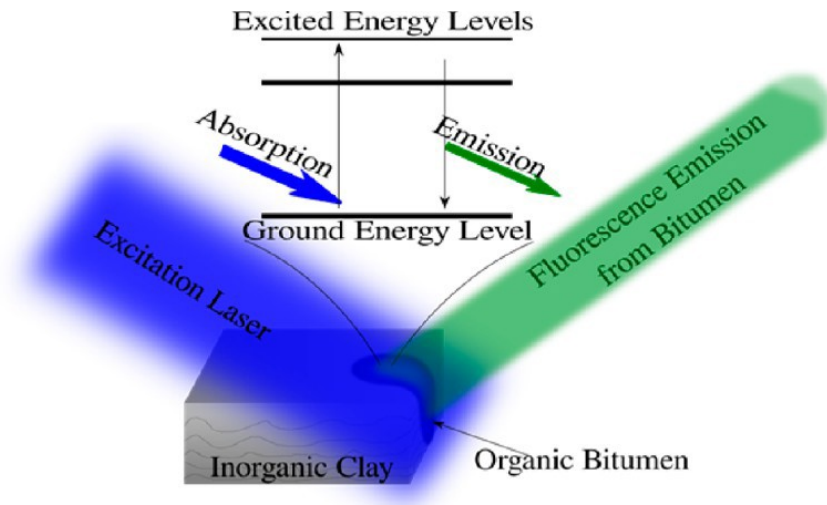


Figure 3-1: Fluorescence emitted by bitumen on illumination with an excitation laser. Clay does not show fluorescence, and hence, clay and bitumen show a high contrast in fluorescent images.

3.2 Experimental Section

Pure kaolin model clay, Athabasca bitumen, and MFT were provided by the Institute of Oil Sands Innovation (IOSI), University of Alberta. Athabasca bitumen used in the spectrofluorometer and confocal epifluorescence microscopy experiments was obtained from Syncrude Canada, Ltd. It was produced by the hot-water extraction process and contained about 4–5 wt % asphaltenes. The MFT samples used in the confocal epifluorescence microscopy and TIRF experiments were obtained in 2014 from Syncrude Canada, Ltd. tailings ponds. These MFT samples contain approximately 31 wt % solids, 4 wt % bitumen, and 65 wt % water. Confocal epifluorescence microscopy and TIRF do not require an elaborate procedure for sample preparation. The sample preparations simply involved preparing the glass slides.

3.2.1 Spectrofluorometer

Laser source and excitation filters used to image bitumen, asphaltenes, and tailings are indicated in past literature. As a result of some discussions about the excitation wavelength of various bitumen components in these literature (Bearsley et al., 2004), confirming the favorable laser source was deemed necessary for our TIRF experiments. A spectrofluorometer was chosen for this purpose. A Varian Cary Eclipse spectrofluorometer was used to obtain the excitation and emission spectra with respect to fluorescence intensity for bitumen. These spectra aided to visualize the

range of excitation and emission wavelengths over which bitumen can be easily detected using fluorescence techniques. Hence, narrowed down the favorable laser source and emission filter in TIRF for MFT imaging. Dilute bitumen samples with concentrations of 0.1, 0.3, and 0.5 g/L bitumen in toluene were made to obtain these spectra. This was necessary because the spectrofluorometer is known to give better results for dilute samples. As a result of the inner filter effect (Hall, 1989), at a high sample concentration there is high excitation light scattering and internal absorption of fluorescence, leading to the loss of fluorescence intensity in the resulting spectra. As a result, it is necessary to use dilute samples (Brandt, 2010).

A constant quantity (4 mL) of these samples was taken in a glass cuvette to ensure repeatability of results.

3.2.2 Confocal Epifluorescence Microscope

The fluorescence microscope is an optical microscope that uses a high-intensity light source to illuminate a sample, which then emits fluorescence. Fluorescence from the sample is always of higher wavelength than that of the excitation wavelength. A dichroic mirror and an emission filter can allow emitted wavelength to pass through. A condenser and an objective then collect the wavelength. A more efficient form of the fluorescence microscope, the epifluorescence microscope enables illumination and detection to take place on the same side of the sample. This ensures that only reflected excitation light and emitted light are collected by the objective, which drastically increases the signal-to-noise ratio (Ishikawa-Ankerhold et al., 2012). The advantages of using any type of fluorescence microscopy for oil sands related research is that this technique is organic specific, which is not the case with most other techniques being used currently. It is also a non-destructive method and can provide measurements with respect to time (Ishikawa-Ankerhold et al., 2012). Past studies have indicated that bitumen shows natural fluorescence (Bearsley et al., 2004)(R. J. Mikula & Munoz, 2000). Hence, using dyes to tag bitumen is not necessary. This is another advantage of the fluorescence microscopy technique.

The epifluorescence microscope has the objective at the bottom of the sample holder. Consequently, the glass cover had to be placed on the bottom side. All slides were prepared by first placing the sample on the glass cover and then covering the sample with a glass to prevent any possible air gap between the glass cover and the sample. An air gap is not favorable because

the refractive index of air (~ 1) is lower than the refractive index of the glass cover, objective lens, and immersion oil (~ 1.52 for all three), which leads to distortion of the images.

The model clay–bitumen interface sample, bitumen–water interface sample, individual bitumen (as shown in *Figure 3-2*), model clay samples (as shown in *Figure 3-3*), MFT (as shown in *Figure 3-4*), and dilute MFT sample slides were prepared and imaged using an epifluorescence microscope with a xenon lamp source and emission filters in the range of 500–550 nm (green) and 560–640 nm (red). The confocal feature of the epifluorescence microscope made it possible to capture the fluorescence image Z-stack for the MFT samples, which gave information about the shape of the fluorescing particles and also presented the possibility to perform quantitative analysis for changes in the bitumen distribution on clay with variations in temperature, pressure, and flocculants.

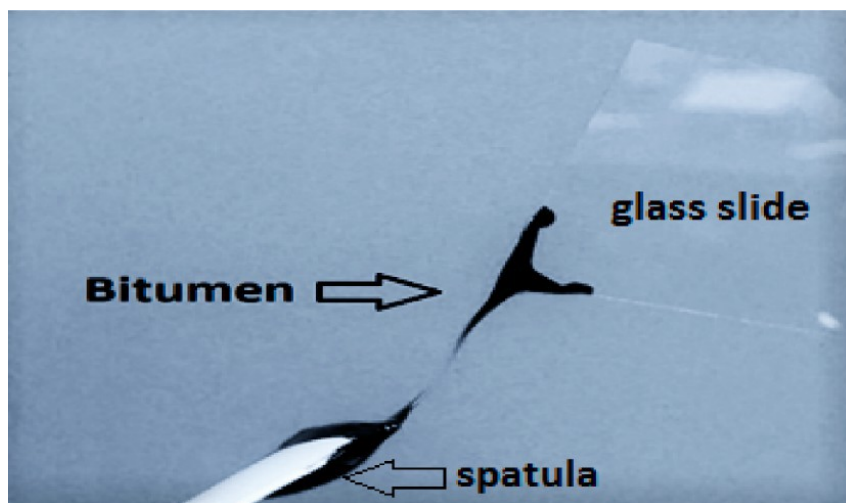


Figure 3-2: Athabasca bitumen that was observed using epifluorescence microscopy techniques.



Figure 3-3: Kaolin (model clay) used to observe the fluorescence intensity difference between bitumen and clay.



Figure 3-4: MFT sample from Syncrude tailings pond.

3.2.3 TIRF Microscope

In a conventional epifluorescence microscope, the entire sample is flooded with excitation light, resulting in fluorescence from all planes. This obscures details in the captured images. In TIRF, the excitation laser is made incident on the glass coverslip at an angle greater than its critical angle, as shown in *Figure 3-5*. As a result, the incident laser undergoes total internal reflection, and only an evanescent field develops adjacent to the glass–sample interface and decays exponentially away from it. The depth of the evanescent field can be controlled by controlling the incident angle. This depth can be made as small as 100 nm, eliminating any noise from deeper planes. The objective lens then collects the light emitted by the fluorophores and a digital camera is used to form the resulting image. This technique can generate a very high-contrast images. Samples prepared for epifluorescence microscopy were also used for TIRF microscopy. The TIRF facility had 488, 543,

and 633 nm laser sources. The emission filters used for the 488, 543, and 633 nm excitation lasers were in the ranges of 500–550 nm (green), 560–640 nm (red), and 650–730 nm (red), respectively. To obtain good TIRF images, the incidence angle was made slightly greater than the critical angle.

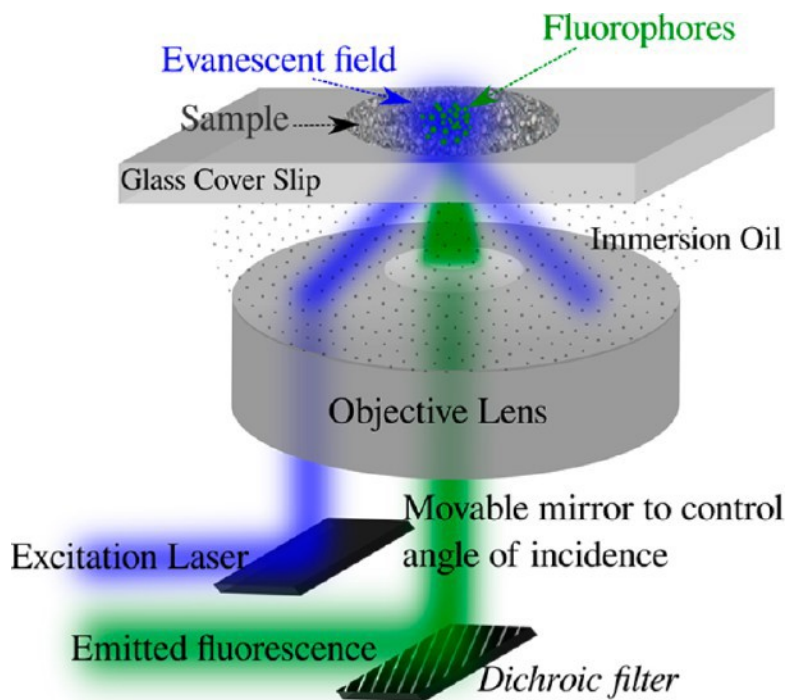


Figure 3-5: TIRF microscope schematic. The sample is illuminated by evanescent fields near the surface of the coverslip.

3.3 Results and Discussion

3.3.1 Spectrofluorometer

The spectrofluorometer experiments helped to narrow down the laser source and filter cubes for the confocal epifluorescence microscope and TIRF microscope experiments. The results obtained from the spectrofluorometer were plotted in the form of color contour maps to help visualize the results. Because toluene was used to prepare the diluted bitumen samples, it was important to obtain excitation and emission spectra data for toluene to make sure that fluorescence from toluene would not interfere with fluorescence from the bitumen. It can be observed in *Figure 3-6A* that toluene did not show any substantial fluorescence in the excitation and emission wavelength ranges of interest.

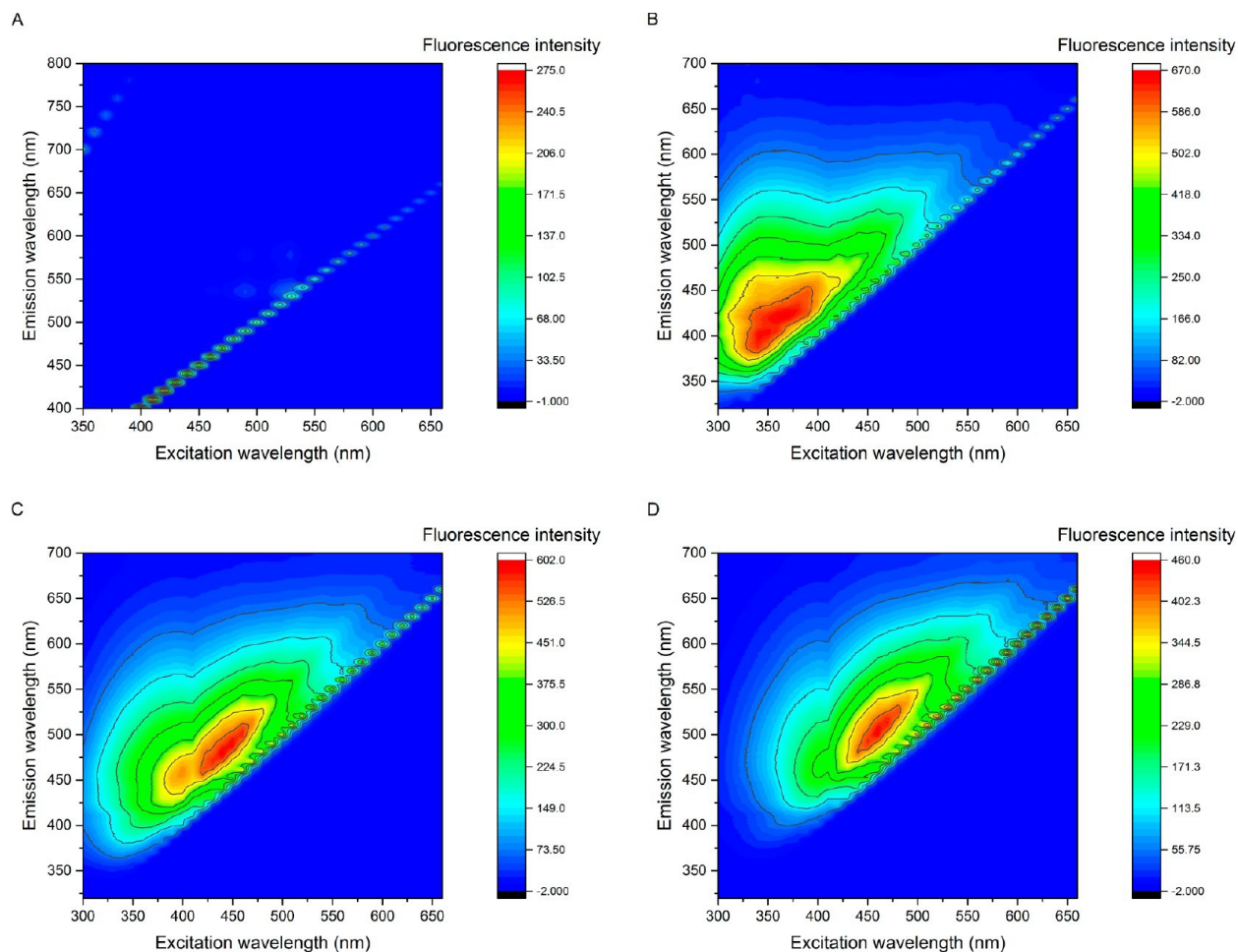


Figure 3-6: Image A shows a spectrofluorometer graph depicting the change in fluorescence intensity for a range of excitation and emission wavelengths for a 4 mL sample of toluene. Images B, C, and D show this graph for 0.1, 0.5, and 0.3 g/L bitumen in toluene, respectively.

The graphs for 0.1, 0.3, and 0.5 g/L concentrations of Athabasca bitumen containing about 4–5 wt% asphaltenes can be seen in the images B, C, and D of *Figure 3-6*, respectively. The spectrofluorometer results showed that the peak excitation wavelength was in the range of 350–500 nm and the peak emission wavelength was in the range of 400–550 nm for the 0.1, 0.3, and 0.5 g/L concentrations of bitumen. These data are in agreement with the literature (Bearsley et al., 2004)(Hung et al., 2004)(Franco et al., 2013)(Stasiuk et al., 2000)(R. J. Mikula & Munoz, 2000). As expected, an increased first-order scattering was observed with an increase in the sample concentration. Taking the spectrofluorometer results into consideration, a 488 nm laser source and

500–550 nm emission filter from the available resources were found to be the best choices for the confocal epifluorescence microscope and TIRF microscope imaging.

3.3.2 Confocal TIRF and Epifluorescence Microscope

Bitumen and clay sample images were taken using bright-field and epifluorescence microscopies. Samples of bitumen were prepared by smearing a thin film of bitumen on the glass cover. The thin film/strands of bitumen made it possible to image it with a bright-field microscope. Samples of kaolin (model clay) were prepared by sprinkling Kaolin powder on the glass cover. The bright-field images of clay and bitumen can be seen in images *A* and *D* of *Figure 3-7*, respectively. *Figure 3-7 D* shows that the lack of contrast makes it difficult to observe bitumen. Bitumen can be clearly observed as a result of its strong fluorescence in images *E* and *F* of *Figure 3-7*. However, *Figure 3-7 B* and *C* shows that clay cannot be clearly seen, because it lacks substantial fluorescence.

The fluorescence intensities of bitumen and kaolin samples (*Figure 3-7*) were compared at the same camera settings in an epifluorescence microscope. These settings were noted and used for MFT samples, ensuring that bitumen and clay could be distinguished in these samples.

Samples with the bitumen and clay interface were prepared by smearing the bitumen strands on the glass cover and sprinkling some kaolin around it. The clay and bitumen interface could be clearly observed using epifluorescence microscopy, as seen in *Figure 3-8*. These images confirm that bitumen and clay can be distinguished using fluorescence techniques.

The water and bitumen sample slides were prepared by smearing the bitumen strands on the glass cover and then adding some water. These sample images were observed using an epifluorescence microscope. *Figure 3-9* shows that water did not show fluorescence and the bitumen/water interface could be clearly distinguished. The fluorescence images for bitumen/ clay and bitumen/water confirmed that bitumen would be clearly seen in MFT sample fluorescence images.

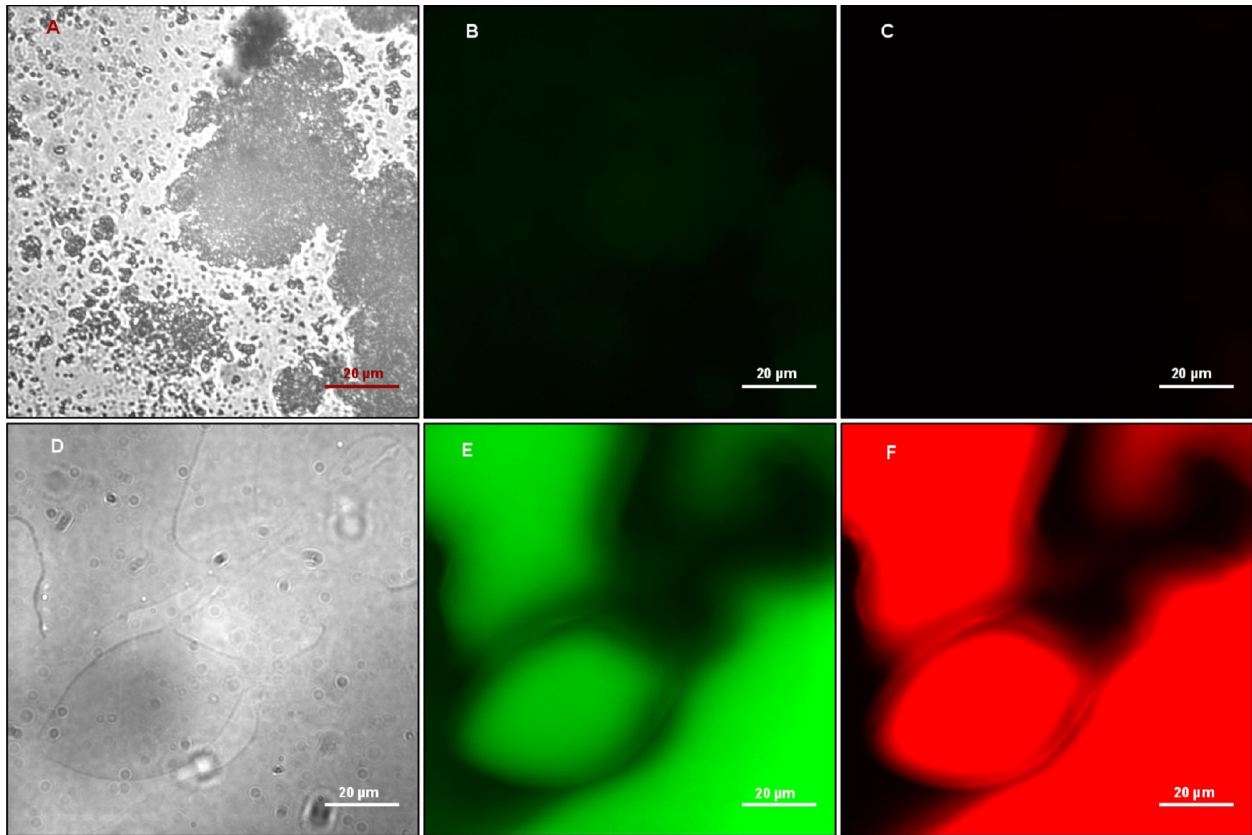


Figure 3-7: Images A and D represent the bright-field image of kaolin and Athabasca bitumen, respectively. Images B and E show the epifluorescence images of clay and Athabasca bitumen, respectively, for excitation with a xenon lamp and emission filter of 500–550 nm. Images C and F show the epifluorescence images of clay and Athabasca bitumen, respectively, for excitation with a xenon lamp and emission filter of 560–640 nm. Clay is not showing substantial fluorescence compared to the strong fluorescence of bitumen.

In the case of the MFT sample, both fluorescence images and bright-field images were important. The bright-field image showed the location of clay particles in the sample, while the fluorescence images showed the location of bitumen. The MFT sample was prepared by smearing a thin film onto the glass cover. The thin film enabled imaging with a bright-field microscope. *Figure 3-10B* and *C* show the fluorescence images of the MFT sample showed fluorescing particles in a pool of non-fluorescing media. The conclusion drawn from imaging the bitumen–clay and bitumen–water interfaces, it is understood that the fluorescing particles were bitumen and non-fluorescing media were water and clay combined. However, as a result of a high concentration of clay particles in these MFT samples, it was difficult to clearly observe clay particle boundaries in the bright-field images of MFT samples. *Figure 3-10A* did not clearly show whether the bitumen was attached to

the clay, suspended in water, or both. To overcome this information deficit, the MFT sample was diluted. The three-dimensional (3D) image seen in *Figure 3-10D* helped to clarify the shape of the fluorescing particles.

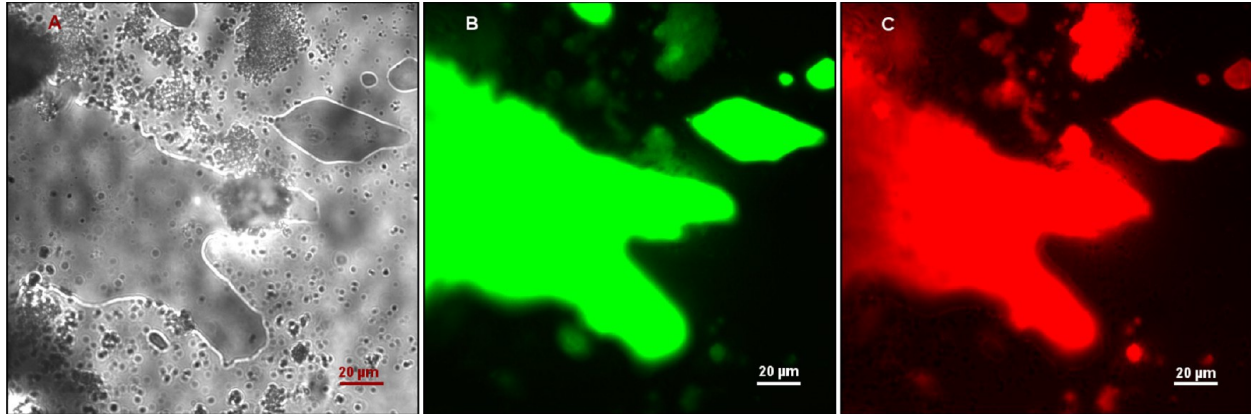


Figure 3-8: Image A shows a bright-field image of the clay and bitumen interface. Image B shows the fluorescence image of the clay and bitumen interface for excitation with a xenon lamp and emission filter of 500–550 nm. Image C shows the fluorescence image of the clay and bitumen interface for excitation with a xenon lamp and emission filter of 560–640 nm. A clear clay and bitumen interface is visible with epifluorescence.

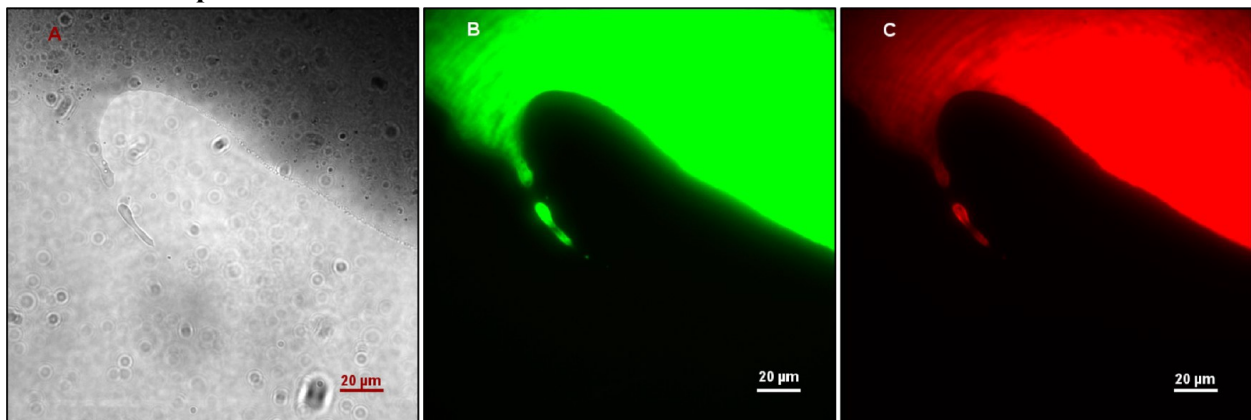


Figure 3-9: Image A shows a bright-field image of the water and bitumen interface. Image B shows the fluorescence image of the water and bitumen interface for excitation with a xenon lamp and emission filter of 500–550 nm. Image C shows the fluorescence image of the water and bitumen interface for excitation with a xenon lamp and emission filter of 560–640 nm. The water and bitumen interface is clearly seen with epifluorescence.

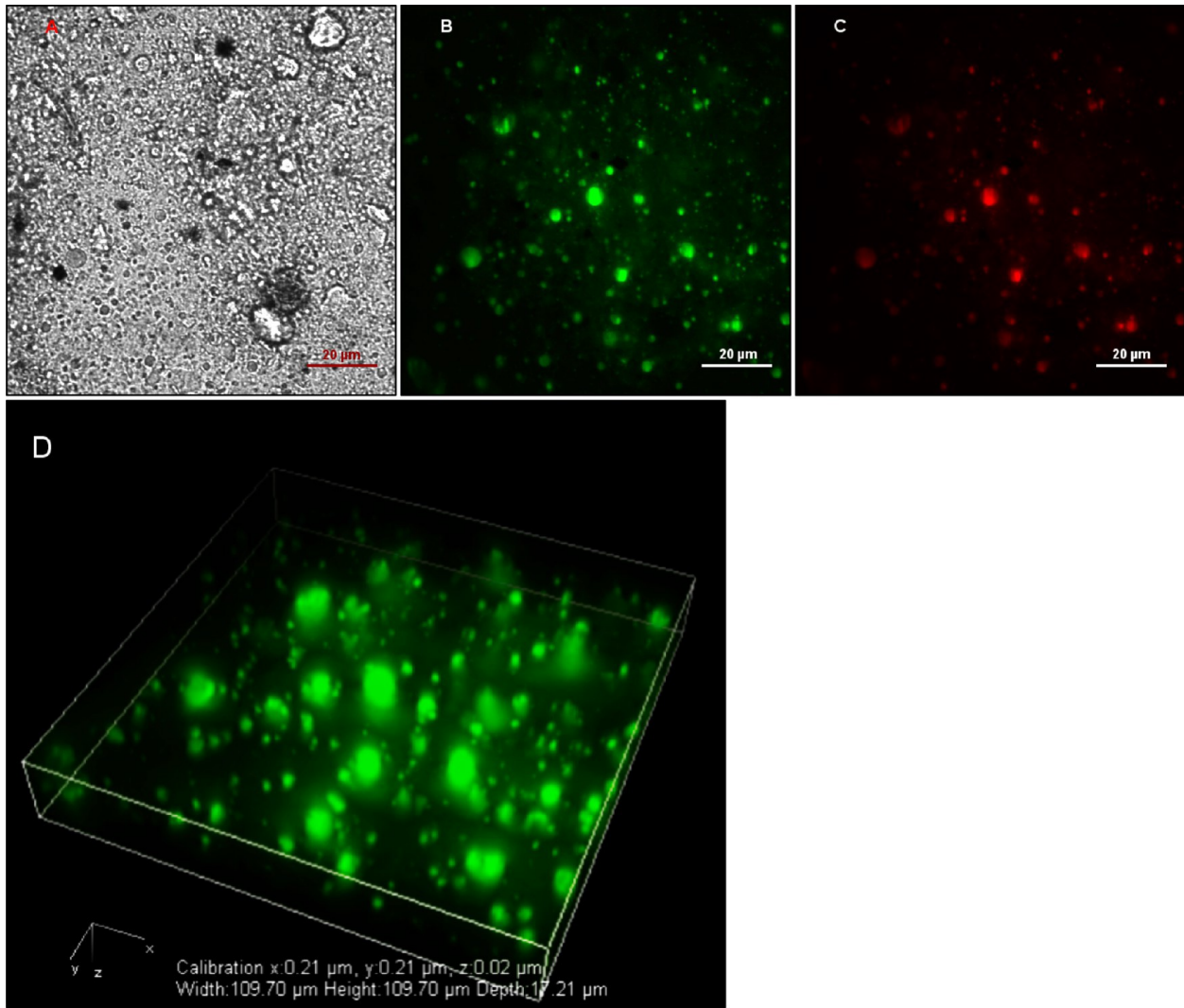


Figure 3-10: Image A shows a bright-field image of the MFT sample. Image B shows the TIRF images of the MFT sample for an excitation laser of 488 nm and emission filter of 500–550 nm, and image C shows the TIRF image of the MFT sample for an excitation laser of 543 nm and emission filter of 560–640 nm. MFT sample fluorescence images indicate that the fluorescing bitumen particles dispersed in non-fluorescing clay and water. Image D shows 3D reconstruction of the MFT sample at the same location and settings as image B.

Diluted MFT samples were prepared by first diluting 1 g of MFT with about 100 mL of deionized water at 60 °C. A drop of this diluted MFT was added to the glass cover, allowed to dry, and covered with a glass slide. As seen in *Figure 3-11A*, the bright-field image of diluted MFT samples helped to observe that a single layer of clay aggregated and reduced the density of clay particles, which previously obscured details. It showed the two-dimensional (2D) shape of clay aggregates

and also helped to better understand the bitumen coverage on clay. These samples were easier to observe under a bright field, and noise was greatly reduced in these images as a result of a lower concentration of clay particles.

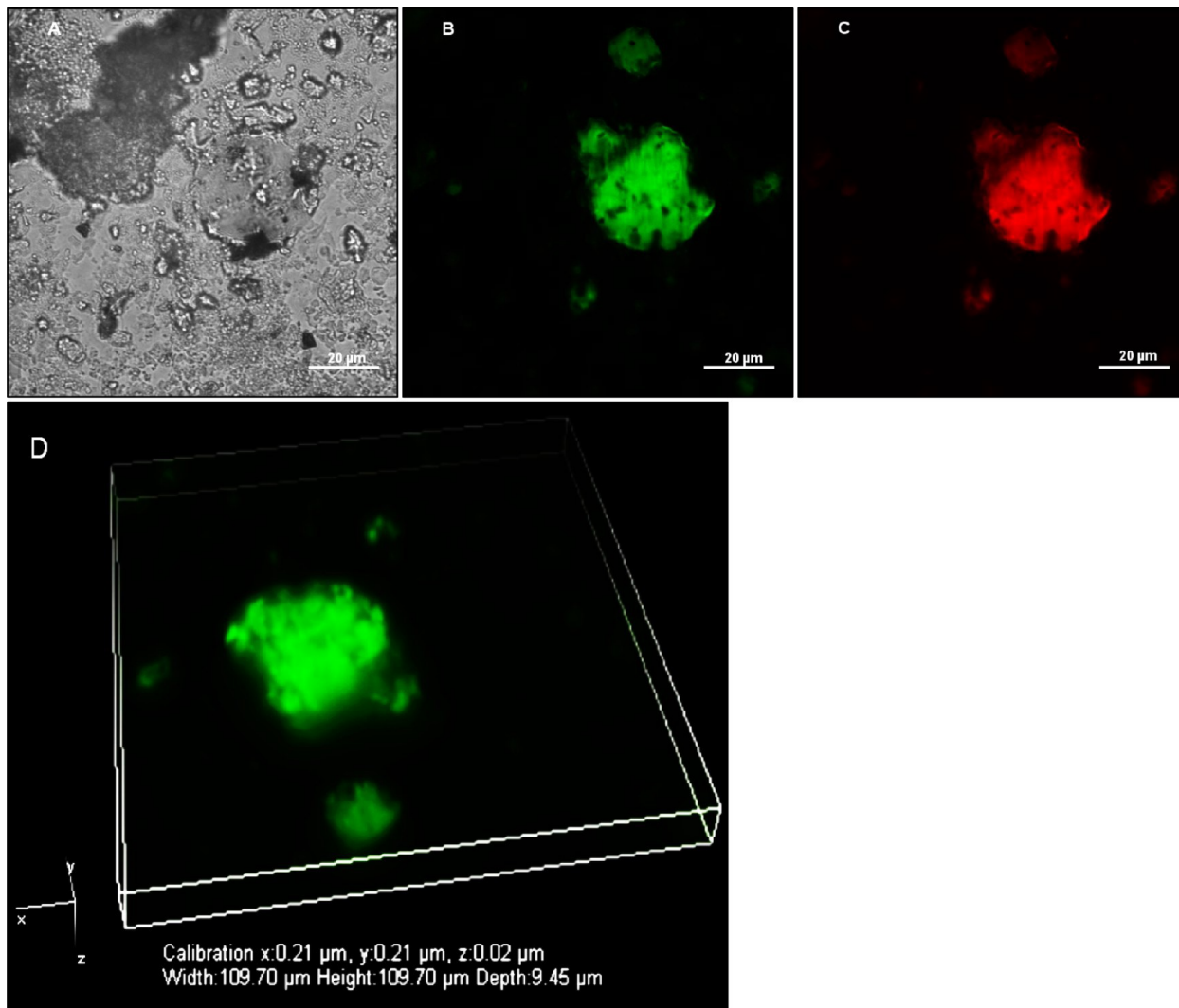


Figure 3-11: Image A shows a bright-field image of the diluted MFT sample. Image B shows the TIRF images of the diluted MFT sample for an excitation laser of 488 nm and emission filter of 500–550 nm, and image C shows the TIRF image of the diluted MFT sample for an excitation laser of 543 nm and emission filter of 560–640 nm. The diluted MFT sample fluorescence image shows fluorescing bitumen particles near the clay particle location in the bright-field image. Image D shows 3D reconstruction of the diluted MFT sample at the same location and settings as image B.

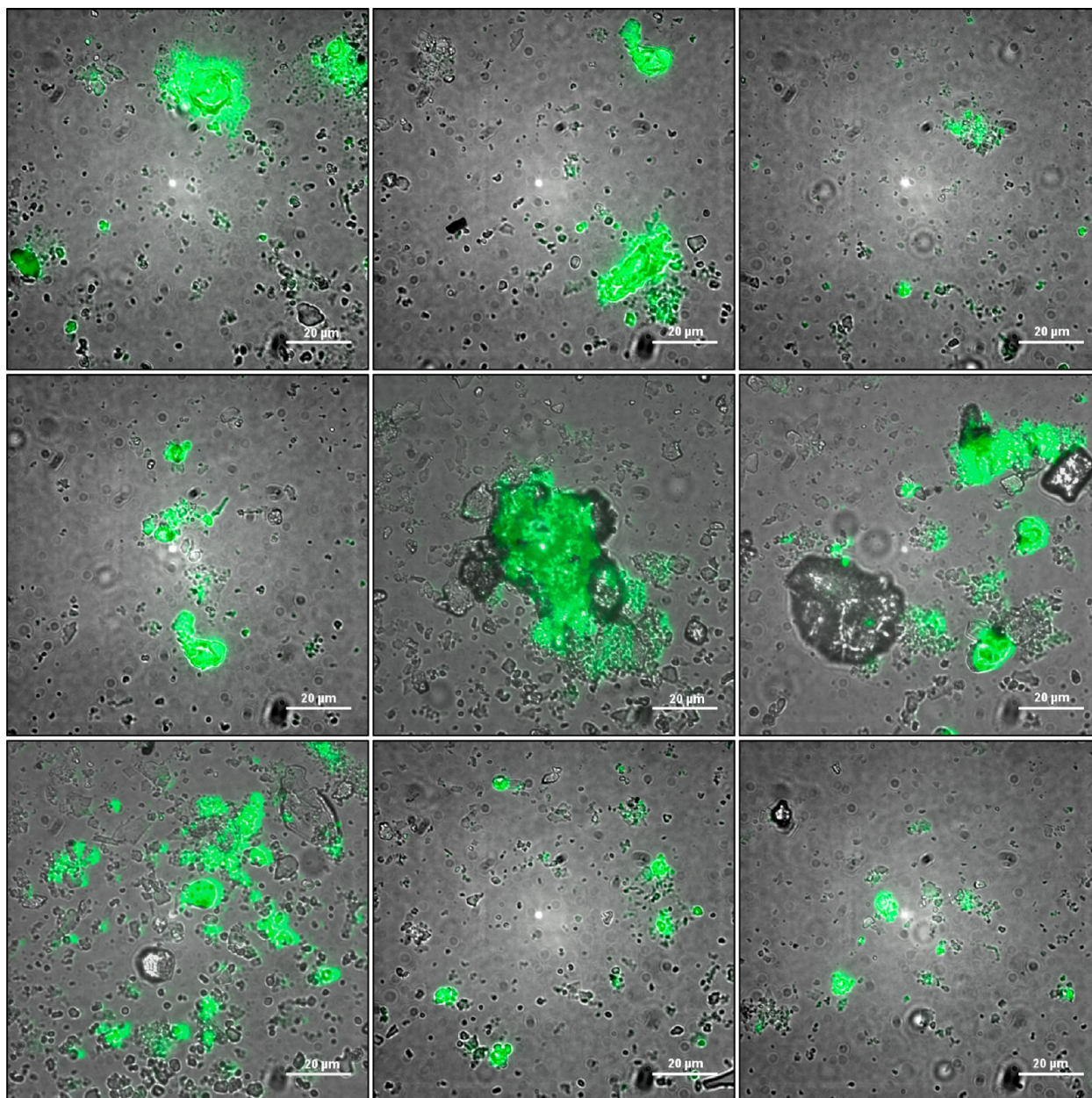


Figure 3-12: Superimposed bright-field and 488 nm excitation laser TIRF images of the diluted MFT sample. The dark gray particles in these images are clay particles, while the green dots are bitumen.

The fluorescence images *B* and *C* of *Figure 3-11* show the bitumen near the clay particles in the bright-field image. *Figure 3-11D* shows a 3D reconstruction of the diluted MFT sample at the same location as the 2D images. This image gives an idea of the shape of the bitumen-coated clay aggregates. The 3D images can be used for future image analysis to find the surface coverage of bitumen on clay aggregates.

All of the fluorescence images in this paper were taken at the same camera settings, with exposure time set at 200 ms and exposure multiplier set at 100, to help maintain consistency in the results.

Figure 3-12 shows various bright-field images and fluorescence images of diluted MFT samples, which were superimposed using ImageJ software to observe the bitumen surface coverage on the clay particles. In *Figure 3-12*, the dark gray particles are clay (“Hande, Aharnish. Accelerated Dewatering and Drying Treatment of Oil Sands Tailings by Electrical Resonant Auto-Transformer. Master of Science Dissertation, University of Alberta, Canada,” 2014) and green dots are bitumen. In this sample of MFT, bitumen is not suspended freely in water. Residual bitumen is bridging and coating the clay agglomerates. It can also be seen that only some percentage of clay aggregates is associated with bitumen, confirming the presence of water-wet and bitumen-wet clays in MFT.

3.4 Conclusion

Most previous methods have been able to map MFT samples with only predictions about the bitumen location. This was mainly due to the use of inorganic-specific techniques (Masliyah, Jacob H. (Jacob Heskell), Xu, Z. (Zhenghe), Czarnecki, Jan A. (Jan Adam), Dabros, 2011). The high-resolution and organic-specific TIRF microscope images discussed in this paper help to map the exact location and surface coverage of bitumen on fine clay in MFT. These images also make it possible to observe the presence of water-wet clay particles, along with the bitumen-wet clay particles. They also shed light on the bitumen–clay particle boundaries and surfaces, which can be even more clearly visualized with the aid of edge detection techniques in image analysis. At 0.3 μm resolution, the images also show that bitumen coats some clay and bridges some clay aggregates together, as conceptually visualized in previous literature (Sparks et al., 2003). There was no free bitumen observed in the bulk of the MFT sample at the current resolution.

The resolution of images can be further improved using metamaterial substrate instead of a glass coverslip (R. Starko-Bowes, J. Atkinson, W. Newman, H. Hu, T. Kallos, G. Palikaras, R. Fedosejevs, S. Pramanik, Jacob, 2015). Imaging the bitumen coverage on clay and observing its effect on the clay–clay interaction will aid in the development of techniques to accelerate clay agglomeration/sedimentation and enhance bitumen recovery in the future.

3.5 References

- Amann, K. J., & Pollard, T. D. (2001). Direct real-time observation of actin filament branching mediated by Arp23 complex using total internal reflection fluorescence microscopy. *Pnas*, 98(26), 15009–15013.
- Bearsley, S., Forbes, a., & Haverkamp, R. G. (2004). Direct observation of the asphaltene structure in paving-grade bitumen using confocal laser-scanning microscopy. *Journal of Microscopy*, 215(August), 149–155. doi:10.1111/j.0022-2720.2004.01373.x
- Boulanger, J., Gueudry, C., Münch, D., Cinquin, B., Paul-Gilloteaux, P., Bardin, S., ... Salamero, J. (2014). Fast high-resolution 3D total internal reflection fluorescence microscopy by incidence angle scanning and azimuthal averaging. *Proceedings of the National Academy of Sciences of the United States of America*, 111(48), 17164–9. doi:10.1073/pnas.1414106111
- Boxill, L. (2011). Potential for use of methylene blue index testing to enhance geotechnical characterization of oil sands ores and tailings. *Proceedings of Tailings and Mine Waste*.
- Brandt, M. (2010). Spectrofluorometers and Fluorescence Phenomena. Retrieved January 1, 2015, from http://loci.wisc.edu/files/loci/Introduction_to_Spectrofluorometry.pdf
- Dang-Vu, T., Jha, R., Wu, S.-Y., Tannant, D. D., Masliyah, J., & Xu, Z. (2009b). Effect of solid wettability on processability of oil sands ores. *Energy Fuels*, 23(5), 2628–2636. doi:10.1021/ef9000117
- Folwell, B. D., McGenity, T. J., Price, A., Johnson, R. J., & Whitby, C. (2014). Exploring the capacity for anaerobic biodegradation of polycyclic aromatic hydrocarbons and naphthenic acids by microbes from oil-sands-process-affected waters. *International Biodeterioration and Biodegradation*, 108, 214–221. doi:10.1016/j.ibiod.2014.12.016
- Franco, J. C., Gonçalves, G., Souza, M. S., Rosa, S. B. C., Thiegue, L. M., Atvars, T. D. Z., ... Nome, R. A. (2013). Towards in situ fluorescence spectroscopy and microscopy investigations of asphaltene precipitation kinetics. *Optics Express*, 21(25), 30874. doi:10.1364/OE.21.030874

- Hall, G. (1989). Correction of Polychromatic Luminescence Signals for Inner-Filter Effects. *Applied Spectroscopy*, 43(5), 759–767.
- Hande, Aharnish. Accelerated Dewatering and Drying Treatment of Oil Sands Tailings by Electrical Resonant Auto-Transformer. Master of Science Dissertation, University of Alberta, Canada. (2014). University of Alberta.
- Holden, A. A., Haque, S. E., Mayer, K. U., & Ulrich, A. C. (2013). Biogeochemical processes controlling the mobility of major ions and trace metals in aquitard sediments beneath an oil sand tailing pond: Laboratory studies and reactive transport modeling. *Journal of Contaminant Hydrology*. doi:10.1016/j.jconhyd.2013.04.006
- Hooshar, A., Uhlík, P., Ivey, D. G., Liu, Q., & Etsell, T. H. (2012). Clay minerals in nonaqueous extraction of bitumen from Alberta oil sands: Part 2. Characterization of clay minerals. *Fuel Processing Technology*, 96, 183–194. doi:10.1016/j.fuproc.2011.10.010
- Hooshar, A., Uhlík, P., Kaminsky, H. W., Shinbine, A., Omotoso, O., Liu, Q., ... Etsell, T. H. (2010). High resolution transmission electron microscopy study of clay mineral particles from streams of simulated water based bitumen extraction of Athabasca oil sands. *Applied Clay Science*, 48(3), 466–474. doi:10.1016/j.clay.2010.02.008
- Hung, J., Castillo, J. A., & Reyes, A. (2004). Colloidal structural evolution of asphaltene studied by confocal microscopy, 5622, 154–159. doi:10.1117/12.591036
- Ishikawa-Ankerhold, H. C., Ankerhold, R., & Drummen, G. P. C. (2012). Advanced Fluorescence Microscopy Techniques—FRAP, FLIP, FLAP, FRET and FLIM. *Molecules*, 17(12), 4047–4132. doi:10.3390/molecules17044047
- Johnston, C. T. (2010). Probing the nanoscale architecture of clay minerals. *Clay Minerals*, 45(3), 245–279. doi:10.1180/claymin.2010.045.3.245
- Kaminsky, H. A. W., Etsell, T. H., Ivey, D. G., & Omotoso, O. (2009). Distribution of clay minerals in the process streams produced by the extraction of bitumen from Athabasca oil sands. *The Canadian Journal of Chemical Engineering*, 87(1), 85–93. doi:10.1002/cjce.20133

- Klein, Colin. Effect of Residual Bitumen on Polymer-assisted Flocculation of Fluid Fine Tailings. Master of Science Dissertation, University of Alberta, Canada. (2014). University of Alberta, Canada.
- Knight, A. E. (2014). Single-molecule fluorescence imaging by total internal reflection fluorescence microscopy (IUPAC Technical Report). *Pure and Applied Chemistry*, 86(8), 1303–1320. doi:10.1515/pac-2012-0605
- Li, H., Long, J., Xu, Z., & Masliyah, J. H. (2008). Novel polymer aids for low-grade oil sand ore processing. *Can. J. Chem. Eng.*, 86(Copyright (C) 2010 American Chemical Society (ACS). All Rights Reserved.), 168–176. doi:10.1002/cjce.20030
- Liu, J., Xu, Z., & Masliyah, J. (2004). Role of fine clays in bitumen extraction from oil sands. *AIChE Journal*, 50(8), 1917–1927. doi:10.1002/aic.10174
- Marshall, G. M., Kingston, D. M., Moran, K., & Mercier, P. H. J. (2013). Multivariate factor analysis of heavy minerals concentrate from Athabasca oil sands tailings by X-ray photoelectron spectroscopy. *Surface and Interface Analysis*, (November 2012), n/a–n/a. doi:10.1002/sia.5201
- Masliyah, J., Zhou, Z. J., Xu, Z., Czarnecki, J., & Hamza, H. (2004). Understanding Water-Based Bitumen Extraction from Athabasca Oil Sands. *The Canadian Journal of Chemical Engineering*, 82(4), 628–654. doi:10.1002/cjce.5450820403
- Masliyah, Jacob H. (Jacob Heskell), Xu, Z. (Zhenghe), Czarnecki, Jan A. (Jan Adam), Dabros, M. (2011). *Handbook on theory and practice of bitumen recovery from Athabasca Oil Sands (volume 1:)*. Kingsley Knowledge Publishing.
- Mercier, P. H. J., Ng, S., Moran, K., Sparks, B. D., Kingston, D., Kotlyar, L. S., ... McCracken, T. (2012). Colloidal Clay Gelation: Relevance to Current Oil Sands Operations. *Petroleum Science and Technology*, 30(April 2015), 915–923. doi:10.1080/10916466.2010.495959
- Mikula, R. J., & Munoz, V. a. (2000). Characterization of emulsions and suspensions in the petroleum industry using cryo-SEM and CLSM. *Colloids and Surfaces A:*

- Physicochemical and Engineering Aspects, 174, 23–36. doi:10.1016/S0927-7757(00)00518-5
- Mpofu, P., Addai-Mensah, J., & Ralston, J. (2003). Investigation of the effect of polymer structure type on flocculation, rheology and dewatering behaviour of kaolinite dispersions. *International Journal of Mineral Processing*, 71(1-4), 247–268. doi:10.1016/S0301-7516(03)00062-0
- Muñoz, V. a., Kasperski, K. L., Omotoso, O. E., & Mikula, R. J. (2003). The Use of Microscopic Bitumen Froth Morphology for the Identification of Problem Oil Sand Ores. *Petroleum Science and Technology*, 21(9-10), 1509–1529. doi:10.1081/LFT-120023225
- Nazemifard, N., Bhattacharjee, S., JH, M., & DJ, H. (2013). Nonmonotonous variation of DNA angular separation during asymmetric pulsed field electrophoresis. *Electrophoresis*, 34(17), 2453–2463. doi:10.1002/elps.201300152
- Osacky, M., Geramian, M., Dyar, M. D., Sklute, E. C., Valter, M., Ivey, D. G., ... Etsell, T. H. (2013). Characterisation of petrologic end members of oil sands from the Athabasca region, Alberta, Canada. *The Canadian Journal of Chemical Engineering*, 9999(June), 1–14. doi:10.1002/cjce.21860
- Osacky, M., Geramian, M., Ivey, D. G., Liu, Q., & Etsell, T. H. (2015). Influence of Nonswelling Clay Minerals (Illite, Kaolinite, and Chlorite) on Nonaqueous Solvent Extraction of Bitumen. *Energy & Fuels*, 29(7), 4150–4159. doi:10.1021/acs.energyfuels.5b00269
- R. Starko-Bowes, J. Atkinson, W. Newman, H. Hu, T. Kal-los, G. Palikaras, R. Fedosejevs, S. Pramanik, Jacob, Z. (2015). Optical characterization of epsilon-near-zero, epsilon-near-pole, and hyperbolic response in nanowire metamaterials. *Journal of the Optical Society of America B*, 32(10), 2074–2080. doi:10.1364/JOSAB.32.002074
- Scott, A. C., MacKinnon, M. D., & Fedorak, P. M. (2005). Naphthenic acids in athabasca oil sands tailings waters are less biodegradable than commercial naphthenic acids. *Environmental Science and Technology*, 39(21), 8388–8394. doi:10.1021/es051003k

- Shen, H., Huang, E., Das, T., Xu, H., Ellisman, M., & Liu, Z. (2014). TIRF microscopy with ultra-short penetration depth. *Optics Express*, 22(9), 10728–34. doi:10.1364/OE.22.010728
- Sparks, B. D., Kotlyar, L. S., Carroll, J. B., & Chung, K. H. (2003). Athabasca oil sands: Effect of organic coated solids on bitumen recovery and quality. *Journal of Petroleum Science and Engineering*, 39(3-4), 417–430. doi:10.1016/S0920-4105(03)00080-9
- Stasiuk, L. D., Gentzis, T., & Rahimi, P. (2000). Application of spectral fluorescence microscopy for the characterization of Athabasca bitumen vacuum bottoms. *Fuel*, 79(7), 769–775. doi:10.1016/S0016-2361(99)00198-2
- Tamiz Bakhtiari, M., Harbottle, D., Curran, M., Ng, S., Spence, J., Siy, R., ... Xu, Z. (2015). Role of Caustic Addition in Bitumen–Clay Interactions. *Energy & Fuels*, 29(1), 58–69. doi:10.1021/ef502088z
- Wang, X. W., Feng, X., Xu, Z., & Masliyah, J. H. (2010). Polymer aids for settling and filtration of oil sands tailings. *Canadian Journal of Chemical Engineering* (Vol. 88). doi:10.1002/cjce.20283
- Yang, W. Y., Qian, J. W., & Shen, Z. Q. (2004). A novel flocculant of Al(OH)₃-polyacrylamide ionic hybrid. *Journal of Colloid and Interface Science*, 273(2), 400–405. doi:10.1016/j.jcis.2004.02.002
- Yin, X., & Miller, J. D. (2012). Wettability of kaolinite basal planes based on surface force measurements using atomic force microscopy. *Minerals & Metallurgical Processing*, 29(1), 8.

Chapter 4: Total Internal Reflection Fluorescence Tomography to Study Bitumen and Clay interaction in Oil Sands Tailings²

4.1 Introduction

Oil sands deposits covering over 14000 km² and estimated recoverable oil reserves over 300 billion barrels makes this non-conventional oil a major economic driver of Alberta. Oil sands composition can be described as 55-80 wt% sands, 4-18 wt% bitumen, 5-34 wt% fine solids (less than 45 µm), and 2-15 wt% water (Bichard, 1987). Bitumen and fine content of the ore dictate if the ore can be economically processed. Oil sands with bitumen less than 7% is considered uneconomical for mining while ore with bitumen content greater than 10% is considered a rich (Masliyah et al., 2004). Processability of ore can be determined by ease of bitumen detachment from clays and ease of bitumen attachment to the air bubbles (J. Liu et al., 2004). Fines content is important because the fines are known to form a slime coating on bitumen surface and hinder bitumen attachment to air bubbles (Adegoye et al., 2010). Oil sands ore is mined and then the processing is performed by ore preparation, extraction treatment and upgrading. Water based extraction techniques such as Clark Hot Water Extraction (CHWE) Process and Low Energy Extraction (LEE) Process (Fine Tailings Fundamentals Consortium Alberta Energy, 1995) are used commercially. An important parameter for these water based techniques is hydrophobic nature of the minerals that are separated from the bitumen by an aqueous layer (Takamura, 1982). However, it has been confirmed that biwettable and hydrophobic minerals are present in oil sand ores (Sparks et al., 2003). The presence of these biwettable and hydrophobic minerals in oil sands are known to impact bitumen recovery and froth quality (Dang-Vu et al., 2009b). Studies have also shown that bitumen recovery from the oil sands is inversely related to the amount of the organic-coated clays in the raw oil sands ore (Adegoye et al., 2010). Clay characteristics such as high specific surface area, isomorphic substitution, and high cation exchange capacity play an important role in deciding if these clay are problem clays. Swelling of various clays also creates problems by trapping water and preventing speedy settling. Water pH, particle distribution and CEC also affect the swelling in clays (Masliyah, Jacob H. (Jacob Heskell), Xu, Z. (Zhenghe), Czarnecki, Jan A. (Jan Adam), Dabros, 2011). Methods such as Transmission Electron Microscopy (TEM) (Arbor, 1986) and X-ray

² A version of this chapter has been submitted to Elsevier Publications, Fuel journal.

Diffraction (XRD) (H. Liu, Tan, Yu, & Liu, 2015)(Omotoso, Munoz, & Mikula, 2002) have been used to characterize various clays in oil sands. Much work is performed to identify the oil sands minerals but enough research is not performed to understand their surface chemistry.

During oil sands extraction about 10% bitumen is either left in deposits or lost to the tailings. Efficient recovery of Bitumen from oil sands is important economically as well as environmentally. Bitumen extraction process is very water intensive. Each cubic meter of ore uses approximately 3 m³ water (Moore, 1997). Although most of the water is recycled, some of it ends up in tailings ponds. Over 500 million m³ of tailings are being held in tailings ponds (Chalaturnyk & Scott, 2002). Tailings eventually settling into a top water layer, middle layer containing mainly sand and water and a bottom layer called mature fine tailings (MFT) which has about 30 wt% solids (H. Kaminsky, Etsell, Ivey, & Omotoso, 2006). MFT can take several decades to further dewater. It is known to have about 1–5 wt% bitumen. Absence of bitumen in tailings could potentially reduce the severity of failure of containment events due to relatively reduced toxicity of the tailings. Presence of bitumen in tailings is believed to reduce its hydraulic conductivity, consolidation and strength due to complex organic-inorganic interactions. But since direct data for performance with and without bitumen is limited, more research need to be performed in this direction (Chow, McKenna, Win, & Journault, 2014). Bitumen in MFT is suspected to hinder settling of mature fine tailings (MFT) by associating with biwetable and oleophilic clays (R. J. Mikula & Munoz, 2000). These bitumen-clay interactions take place at a nanoscale (Johnston, 2010). Several techniques involving high resolution electron microscope such as Scanning Electron Microscope (SEM), Transmission Electron Microscope (TEM) and Atomic Force Microscope (AFM) have been employed to study these interactions. But extensive sample preparation and highly altered temperature and pressure conditions are suspected to affect sample chemistry and introduce artifacts in the acquired images (Hooshier et al., 2012). These techniques are also not successful in detecting organic materials. Hence bitumen locations and interaction needs to be inferred in these studies (Li et al., 2008).

Since bitumen has been proved to show natural fluorescence (R. J. Mikula & Munoz, 2000), successful detection of bitumen in the MFT samples can be achieved with novel techniques involving fluorescence. Technique such Spectrofluorometer has been engaged in this study in past, to confirm the favorable laser source and filter cubes. Confocal fluorescence microscope was also

used in this study to ensure that only bitumen will show fluorescence while water and clay will not show any fluorescence (Shende, Pendharker, Nazemifard, & Jacob, 2016). These techniques have been mainly utilized in the cell biology field but are recently gaining pace in other area as well. In this study, Total Internal Reflection Fluorescence Microscope (TIRF) has been applied to obtain the first ever TIRF images and tomography of MFT to understand the bitumen and clay surface interaction which will benefit in improving the techniques used for tailings treatment. TIRF provides advantages such as high signal to noise ratio, high depth resolution beyond diffraction limit and high-contrast images due to elimination of background noise (Mattheyses, Simon, & Rappoport, 2010)(Schneckenburger, 2005).

4.2 Experimental Section

Mature fine tailings (MFT) taken in 2012 and 2014 from Syncrude tailings ponds, and in 2016 from CNRL tailings pond were provided by Institute of Oil Sands Innovation (IOSI), University of Alberta. The Syncrude MFT 2012 and 2014 samples contain approximately 31.4 wt% solids, 3.9 wt% bitumen and 64.7 wt% water. The CNRL MFT 2016 contained approximately 67.6 wt% water, 28.8 wt% solids, and 3.6 wt% bitumen.

Total Internal Reflection Fluorescence (TIRF) microscope was used to study MFT samples. Confocal Laser Scanning Microscope (CLSM) was also used to ensure repeatability of the image findings. These techniques do not require elaborate procedure for sample preparation. The sample preparations simply involved preparing the glass slides. The CLSM and TIRF used here are epifluorescence microscopes. Their objectives are at the bottom of sample holder. Hence the glass cover was placed on the bottom side. This is a general practice. If the glass slides were to be placed at the bottom, image deformations would increase due to increased interference from higher glass thickness of glass slides. All images were taken using 100X objective.

Six different dilute MFT samples were made by combination of Syncrude MFT 2012, 2014 and CNRL MFT 2016 with deionized water and process water. These samples were made by adding 0.05~gm MFT to 10~ml water. These dilute MFT samples aided in clearly observing clay particle boundaries in the bright field images.

MFT and dilute MFT samples were observed without drying to ensure that they are observed in their original state. To enable this, well type coverslips were manufactured by gluing the coverslip

with a glass slide with an approximately 10 mm diameter circular aperture created in the center. MFT and dilute MFT samples were placed in these wells and sealed from the top with another glass cover to prevent drying or contamination as seen in *Figure 4-1*.



Figure 4-1: Well type slide with glass coverslip bottom for imaging wet MFT and dilute MFT samples in epifluorescence microscope.

4.2.1 Total Internal Reflection Fluorescence (TIRF) Microscope

Nikon eclipse Ti TIRF was used in this study. It was facilitated with 488~nm, 543~nm and 633~nm lasers manufactured by Melles Griot. The associated excitation filters were in range 500-550~nm, 560-640~nm and 650-730~nm.

Highly sensitive QuantEM 512sc CCD camera using 512x512 back-illumination and 16 μ mX16 μ m pixels was employed for capturing TIRF images. It is mainly favorable for low-light applications and single molecule detection.

As depicted in *Figure 4-2* Total internal reflection occurs at angles greater than the critical angle between the interface of optically higher density medium and optically lower density medium. For total internal reflection to take place, it is preferred that the sample is in aqueous solution or is a water based emulsion. Water (refractive index ~ 1.33) based emulsions ensure that the refractive index of the sample is relatively lower than that of glass (refractive index ~ 1.55) (Kudalkar, Davis, & Asbury, 2016). This condition is satisfied by the MFT and dilute MFT samples.

While total internal reflection ensures that all the incident light is reflected, an evanescent wave which is an electromagnetic field is generated. This wave propagates parallel to the interface and has identical frequency as the incident light. Its intensity decreases exponentially away from the glass cover. Illumination with evanescent wave provides increased axial resolution (z-plane)

between 60~nm-100~nm. This illumination distance can be adjusted by changing the incidence angle. This feature of incidence angle manipulation aided the tomography in this study.

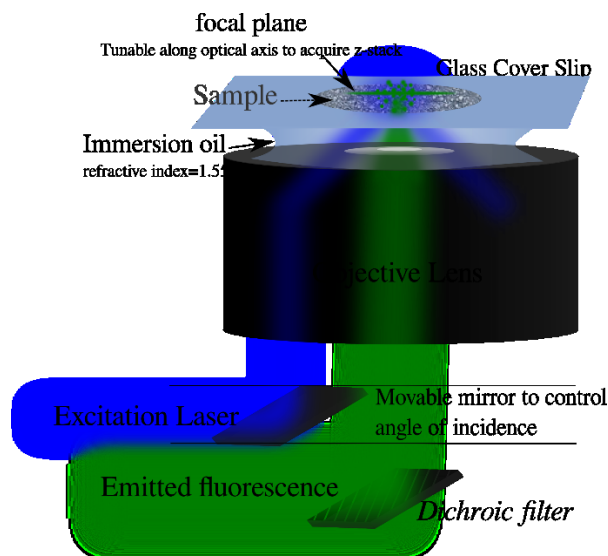


Figure 4-2: Sample illuminated by evanescent water in TIRF microscope using objective lens technique to direct the laser beam.

The TIRF used for this study uses objective lens technique with high numerical aperture (>1.4) to get angles higher than critical angle (Geddes & Lakowicz, 2006). In order to increase the laser angle above critical angle, the laser beam distance from the lens axis was increased between the ranges of 0 to 7000 μm . When the laser beam is at 3500 μm , it is parallel to the lens axis. While moving either towards 0 μm or 7000 μm reduced the penetration of the beam. For all the sample images these values were noted for crucial information regarding the depth of view. Further increasing angle beyond the critical angle, decreased the penetration depth of the evanescent wave, giving images with thinner sections in focus and sharper features.

4.2.2 Confocal laser scanning Microscope (CLSM)

Olympus Fluoview FV300 confocal laser scanning microscope was used in this study. It was mainly helpful in supporting the information obtained from TIRF MFT images. CLSM has various advantages such as capability to collect scans of optical sections from thick specimens with low background noise and controlled depth of field. The illumination technique of the CLSM is different compared to TIRF. The illumination is obtained by laterally scanning the sample with

laser beam. The output from the sample is collected through the pinhole by the photomultiplier tube (PMT) and build into an image in computer (Paddock, 1999).

The Syncrude 2014 dilute MFT sample was imaged using CLSM 488 nm laser to detect fluorescence from bitumen and 632 nm laser and detection between 530 nm–660 nm to collect reflection from non-fluorescing solids such as clay.

4.2.3 Post Dean Stark Analysis Imaging

Dean stark method is usually used to determine the quantity of hydrocarbon and water in a sample (Bertouche et al., 2012). This method was used in this case to image the difficult to recover bitumen in the MFT. Water and bitumen was removed from the MFT samples using the toluene in a reflux method. The experiment was run over 8 hours separately on Syncrude 2014 MFT and CNRL 2016 MFT. All the water and bitumen was removed from the solids left in the thimble which were of the main interest for this study. The toluene was allowed to evaporate from these solids before imaging. Small quantities of these solids were placed in the well type slide and sealed with glass cover.

4.3 Results and Discussion

A simple calculation was performed to estimate approximate bitumen coating thickness for the sample with known quantity of clay and bitumen. It was mainly done to roughly estimate the size of fluorophores. In this calculation it was assumed that all clay particles are uniformly coated with bitumen. This calculation was performed using following information about the oil sands clays:

- Relative quantities of clays in sample are kaolinite: 69%, illite: 28%, montmorillonite: 0.3%, Chlorite: 1%, mixed-layer clays: 1.7% (Masliyah, Jacob H. (Jacob Heskell), Xu, Z. (Zhenghe), Czarnecki, Jan A. (Jan Adam), Dabros, 2011)
- Specific surface areas of clays in sample are kaolinite: 10-20 m²/g, illite: 65-100 m²/g, montmorillonite: 50-120 m²/g, Chlorite: 42 m²/g (Masliyah, Jacob H. (Jacob Heskell), Xu, Z. (Zhenghe), Czarnecki, Jan A. (Jan Adam), Dabros, 2011)

In case of Syncrude 2014 sample, there are 31.4 wt% solids, 3.9 wt% bitumen and 64.7 wt% water. Calculating for 1 g sample. Assuming bitumen density 1000 kg/m³. Also assuming that all clays particles are spherical. Taking the specific surface area of mixed layer clays 50 m²/g and

considering average specific area of all clays, total specific area of clay comes to be approximately $11 \text{ m}^2/\text{g}$. Using this specific surface area the bitumen coating values roughly come to be 3.5 nm .

Since the clay particles were considered to be spherical, which is not the case, bitumen coating will be thinner than the values obtained in the table. The possibility of aggregation of clays is also not considered, which will increase the bitumen coating thickness.

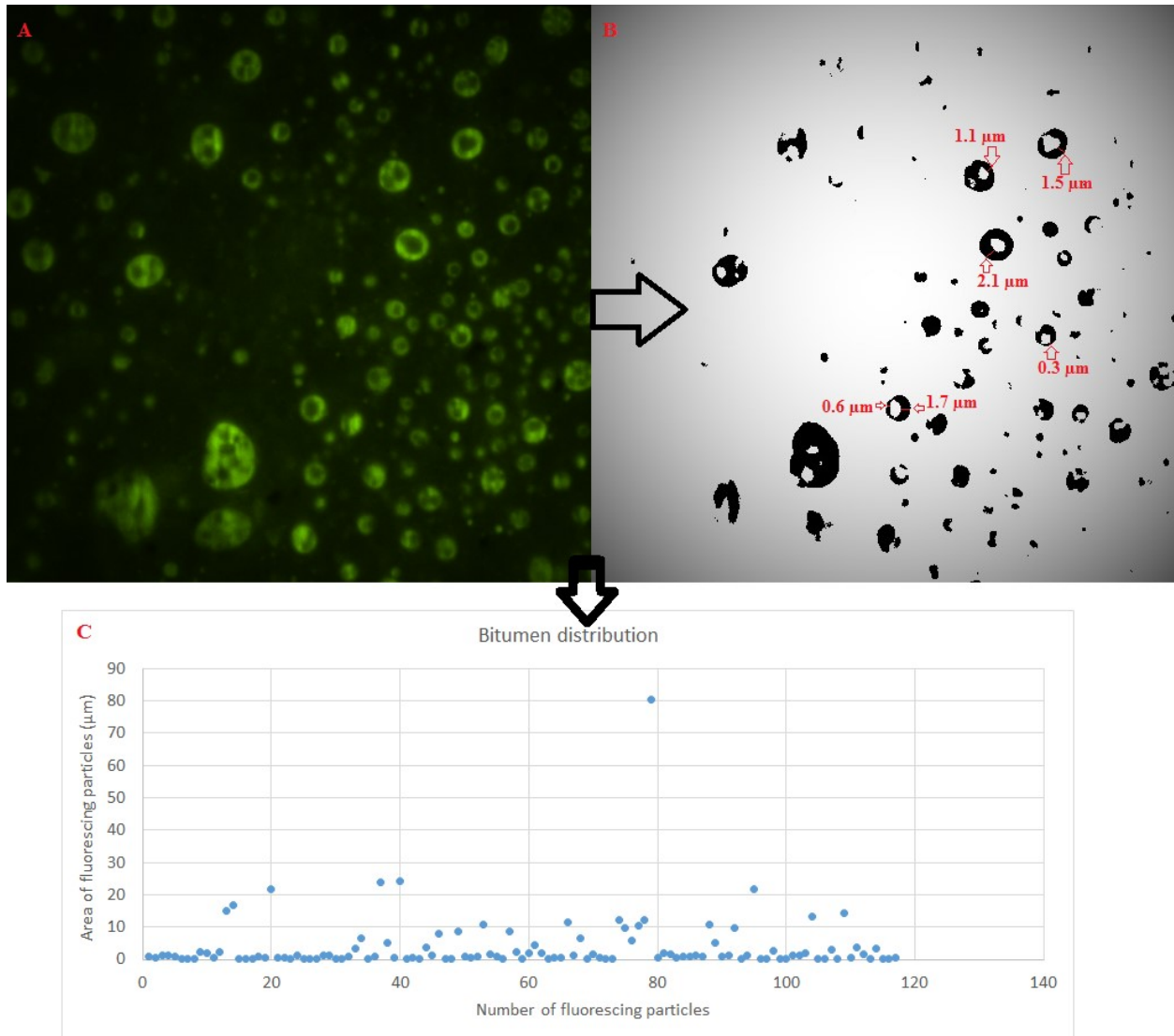


Figure 4-3: Image A is TIRF image of MFT sample. Fluorescing bitumen can be clearly seen in the non-fluorescing medium. Image B is the grayscale image of image A developed using yen algorithm for thresholding. Thresholding gives clear boundaries of bitumen but the low intensity bitumen particles are lost in this image. The thickness of bitumen coating for few particles is shown here. Image C is the graph with number of bitumen particles on x axis and area of bitumen on y axis. This graph roughly shows the bitumen distribution.

Figure 4-3 shows image processing on MFT sample TIRF image provided information about the bitumen coating thickness and a rough idea about bitumen particle distribution. The bitumen thickness is larger than above calculated value due to larger size of clay aggregate. The total area of bitumen coating in this image is $460 \mu\text{m}^2$. This image is 512×512 pixels where $1 \text{ pixel} = 0.21 \mu\text{m}$. Based on this information, 3.9% bitumen is present in this image.

Using spectrofluorometer it was confirmed that 488-nm laser would be appropriate for the MFT sample study. Using confocal fluorescence microscope it was established that in MFT sample clay and water does not show fluorescence. The TIRF images of MFT sample showed the presence of fluorescing bitumen in pool of non-fluorescing water and clay. To understand the bitumen distribution in MFT sample, the constraint was the bright field images which did not clearly show the boundaries of clay. MFT sample was diluted with deionized water which significantly improved the clarity of the bright field images. The dilute MFT images confirmed that bitumen coated and bridged the clay aggregates. These samples did not show any free bitumen (Shende et al., 2016). The discrepancy in these images was that the sample had to be dried before imaging. Hence there was some modification in the chemistry of the sample. To resolve this problem, well type slides were manufactured which could aid with wet sample imaging.

The question that remained was, whether the bitumen coated clay surface completely or partially and why. Answering these question would help to better understand bitumen and clay interaction.

To ensure repeatability of the results, three different MFT samples from Syncrude MFT 2012, Syncrude MFT 2014 and CNRL MFT 2016 were imaged. The TIRF images of these samples showed that CNRL MFT 2016 formed smaller aggregates compared to both the Syncrude MFT samples as seen in *Figure 4-4*. In *Figure 4-4* the image *A*, *B* and *C* of Syncrude 2012 and 2014 MFT samples have larger fluorescing aggregates compared to image *D* of CNRL 2016 MFT sample.

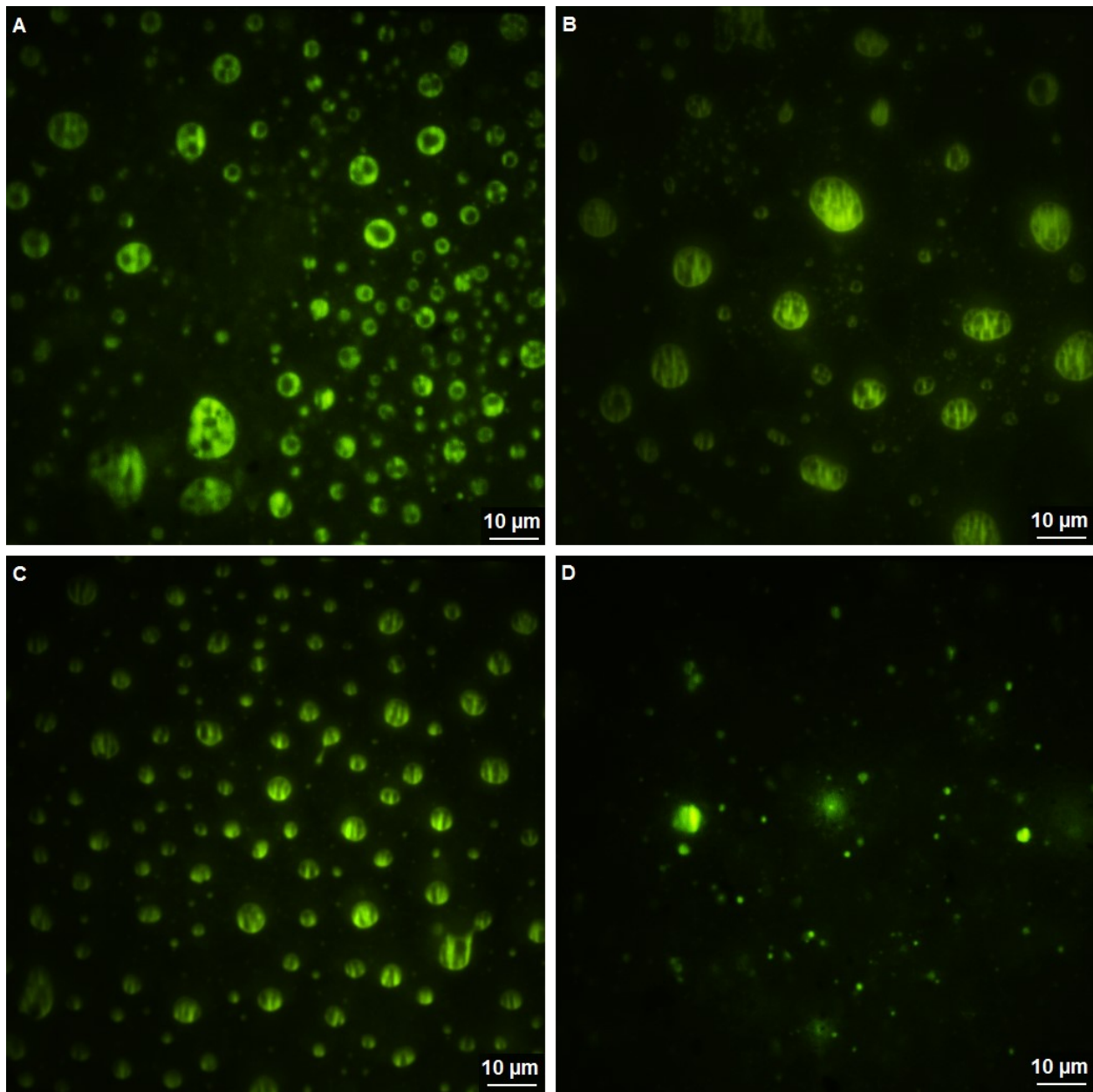


Figure 4-4: Images A and B are the TIRF image of Syncrude MFT 2014. Image C is the TIRF image of Syncrude 2012 and image D is TIRF image of CNRL MFT 2016. These images were taken with reduced laser intensity. They show the features within the fluorescing bitumen coating. CNRL MFT 2016 show smaller fluorescing aggregates compared the Syncrude MFT 2012 and 2014.

4.3.1 Total Internal Reflection Fluorescence (TIRF) Microscope

Since the past MFT images showed strongly fluorescing particles, it was realized that reducing the laser intensity could aid in imaging minute features within the fluorescing particles. This also

reduced photo-bleaching of the sample, resulting in better subsequent 3D imaging. The intensity of laser on the samples was reduced using a manual slider. The images obtained after laser intensity reduction, as seen in *Figure 4-4*, clearly show the presence of non-uniform bitumen coating. The presence of non-fluorescing clay aggregates is seen within the fluorescing bitumen coating in these images taken using TIRF. This non-uniform bitumen coating can be even more clearly visualized in the image *A* of *Figure 4-5*, where individual fluorescing aggregates along with their cross-sectional view are accentuated using colors that are more easily detected by human eyes. In image *B*, *C* and *D* of *Figure 4-5* and image *C* of *Figure 4-6* show three-dimensional tomographic reconstruction from the 3D image. Three-dimensional images of the samples were acquired by z-stacking multiple focal-plane optical sections. These 3D image reconstructions of individual particles were created by thresholding and segmenting the image over selected region-of-interest. These images emphasize and prove the heterogeneity of surface properties of clay aggregates in oil sands MFT (Tombacz & Szekeres, 2006). In these images the presence of clay surfaces with and without bitumen coating can be noted. These images are an evidence of presence of biwetttable clays in oil sands.

Dilute MFT samples were also prepared to obtain bright field images showing clear clay boundaries. All three MFT samples were diluted separately using deionized water and process water with concentration 0.05 gm MFT/10 ml water. These six samples were images in wet condition using TIRF. The images of MFT samples diluted with deionized water had visible bitumen coated clay aggregated settling on the bottom coverslip. Larger fluorescing aggregates were also noted in the TIRF images of these sample as seen in image *A* and *B* of *Figure 4-7*. These TIRF images were taken while keeping diasopic lamp on to simultaneously capture the bright field and TIRF images. This method avoided the errors introduced due to Brownian motion of these dilute samples.

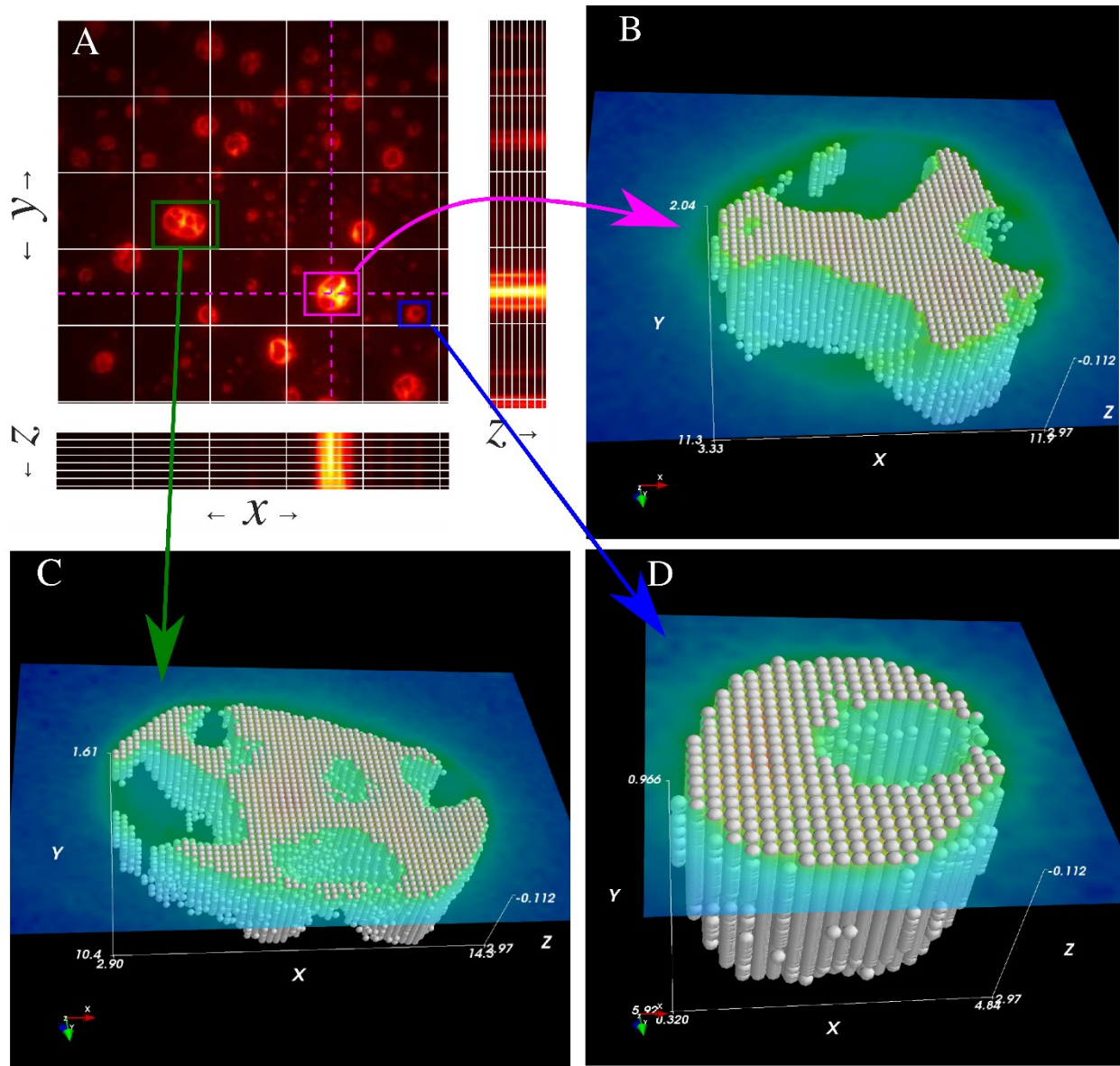


Figure 4-5: Image A is the optical section of the TIRF z-stack images for Syncrude MFT 2014 sample. Image B, C and D show the 3D reconstruction of an aggregate in the image A. It is apparent from these images that bitumen coating on these clay aggregates is non-uniform. There are regions on some of the clay surfaces where bitumen coating is absent.

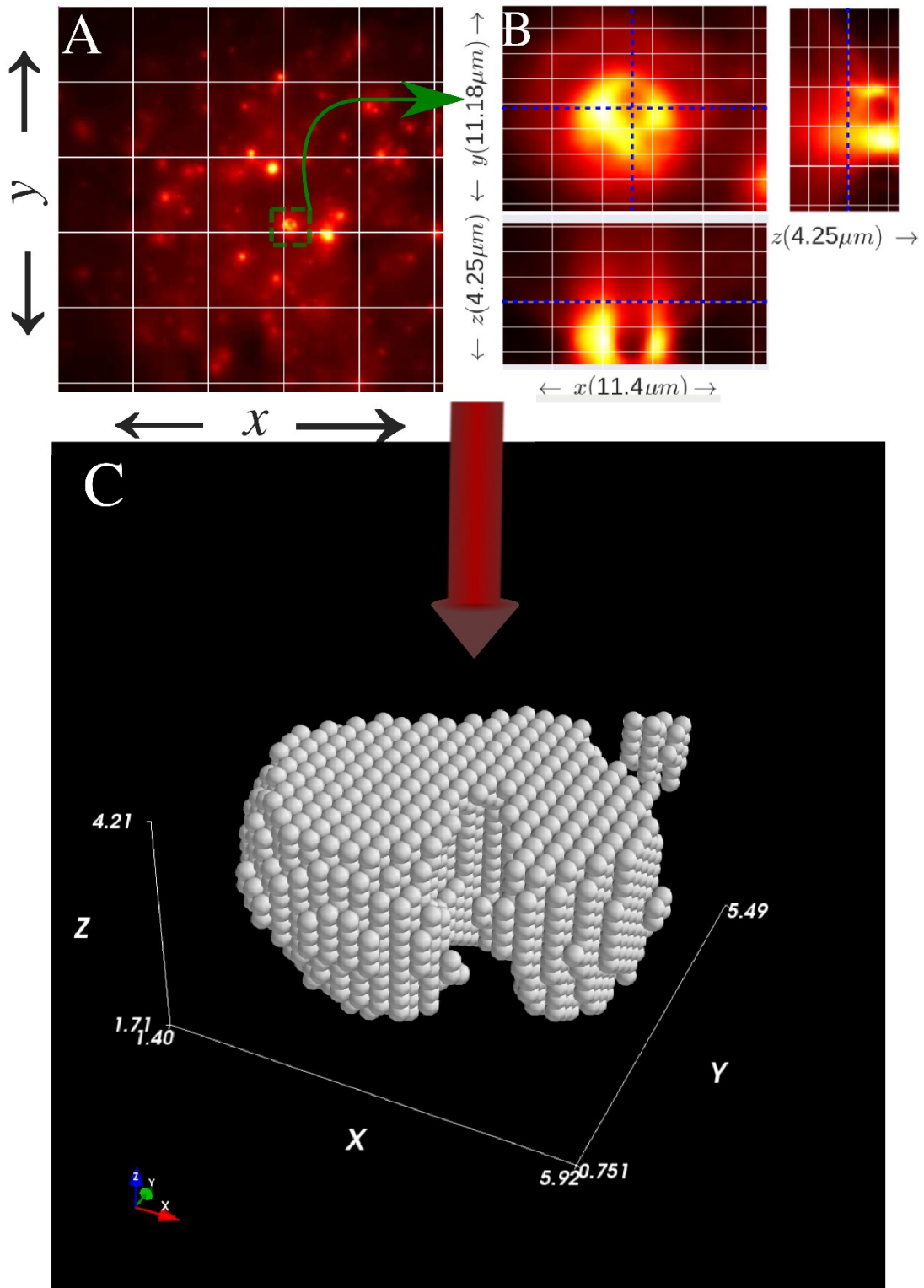


Figure 4-6: Image A is the optical section of the TIRF z-stack images for Syncrude MFT 2014 sample. Image B depicts region of interest with focus on a single aggregate. Image C is the 3D reconstruction of the single aggregate in image B. The uneven bitumen coating can be clearly seen in these images.

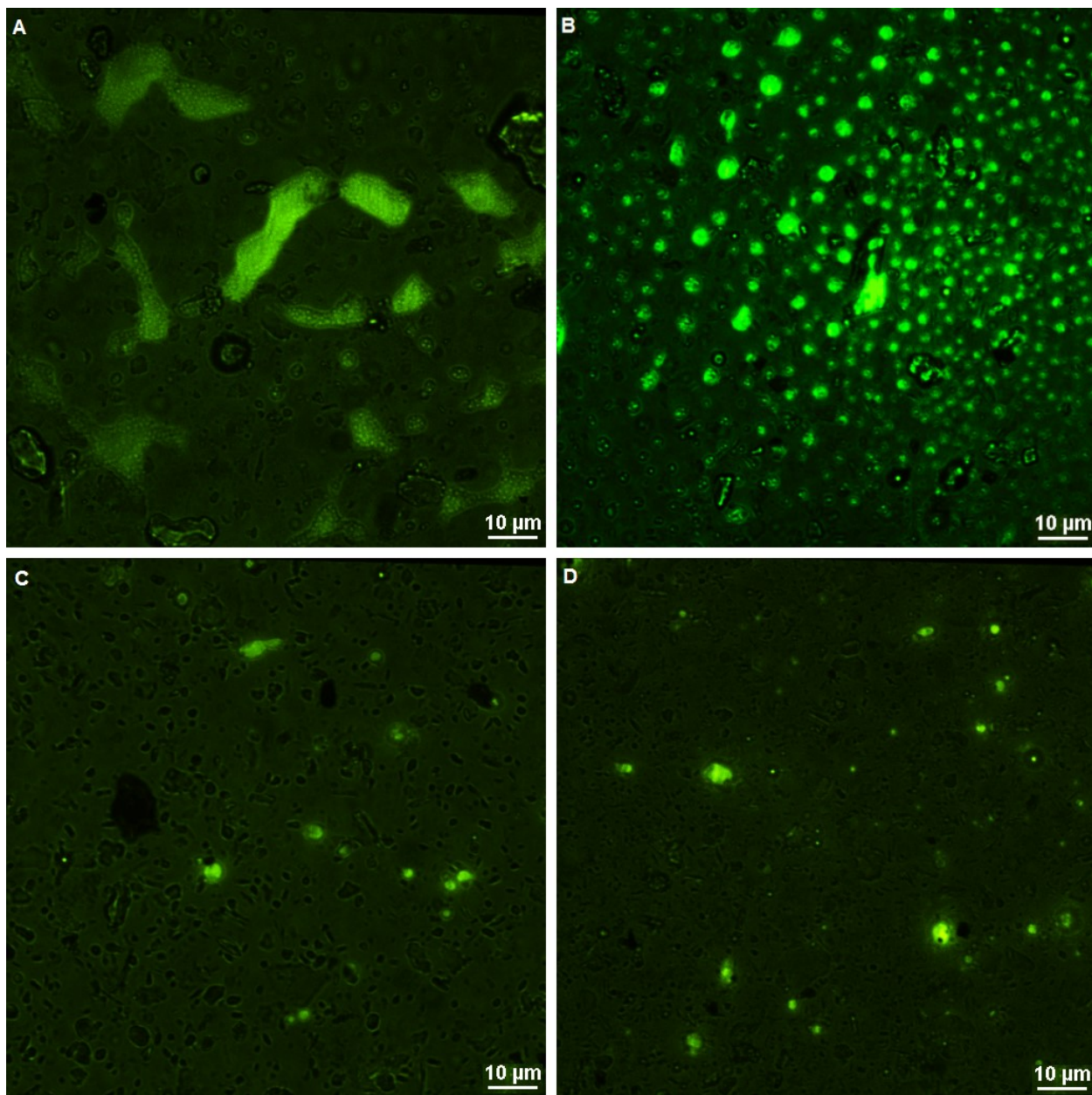


Figure 4-7: Images A and B are Syncrude MFT 2014 in deionized water sample taken while the laser and diascope lamp were simultaneously on. These images show the presence of bitumen coated clay aggregates that have settled on the glass coverslip. Images C and D are Syncrude MFT 2014 in process water sample taken while the laser and diascope lamp were simultaneously on. These images show that not all clay particles are coated with bitumen. They also show the uneven bitumen coating on clay with some sections having higher fluorescence intensity while others with slightly lower fluorescence intensity.

4.3.2 Confocal Laser Scanning Microscope (CLSM)

Images of dilute Syncrude 2014 MFT sample were taken using CLSM. The image A and D in *Figure 4-8* shows the fluorescing particles in the dilute MFT sample. These images were taken using 488 nm laser. This instrument did not allow bright field imaging with PMT. Hence 632 nm laser was used. The emitted light was reflected light from clay showing clear clay boundaries. The images B and E in *Figure 4-8* were taken using 632 nm laser.

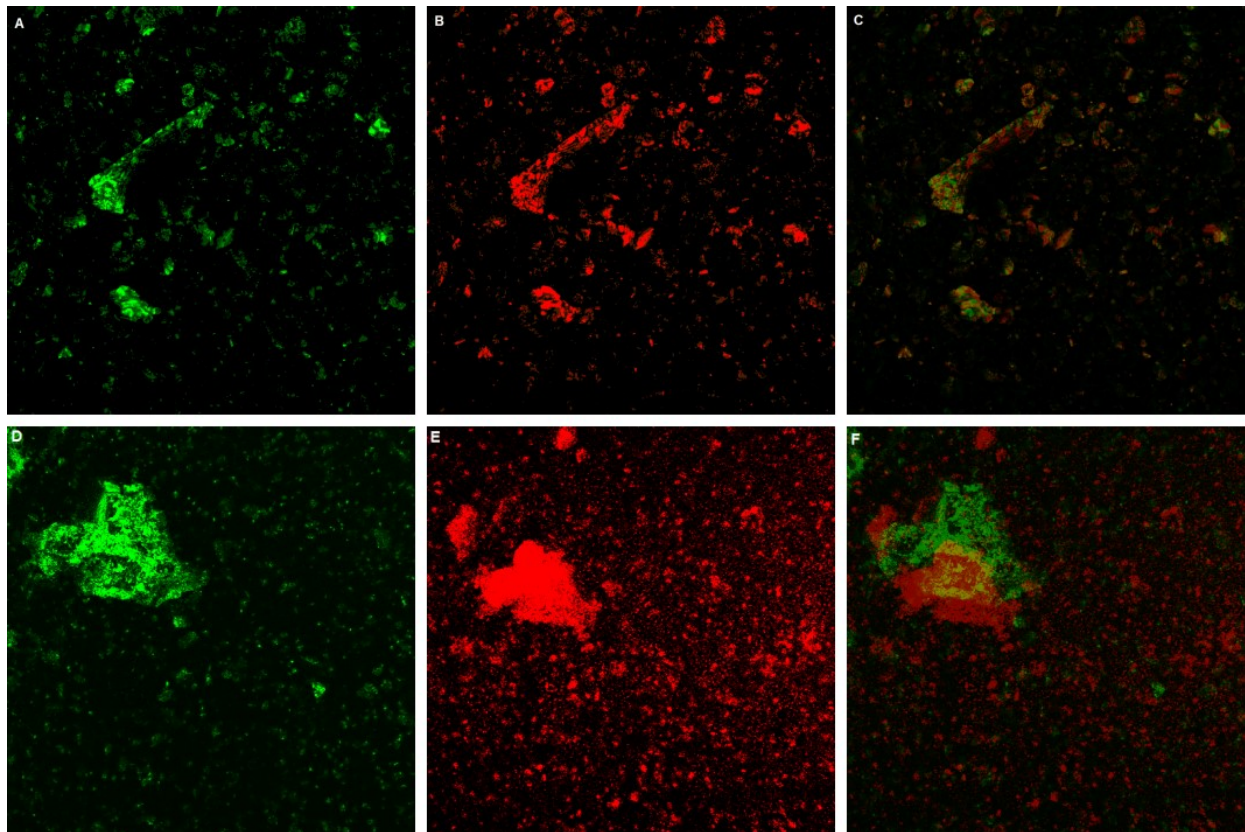


Figure 4-8: Images A and D are dilute Syncrude MFT 2014 sample images taken with Confocal Laser Scanning Microscope (CLSM) 488nm laser. Images B and E are Syncrude MFT 2014 sample images taken with Confocal Laser Scanning Microscope (CLSM) 632nm laser and emission below 530nm and above 660nm are blocked so that no fluorescence is captured by reflection from clay particles are captured. Image C and F shows the superposed images of fluorescence from bitumen and reflection from clay. In the superimposed images the yellow portion shows the overlap while the red part is clay and green part is the bitumen.

Bitumen shows negligible fluorescence when illuminates with this laser. While taking these images emissions below 530 nm and above 660 nm were blocked mainly because these were the

only suitable filters available. These filters mostly blocked any possible fluorescence and only collect reflected light from clay. Images *C* and *F* in *Figure 4-8* show the superimposed images of bitumen and clay. The yellow portion in these images show the overlap between clay and bitumen. It can be observed in these images that not all clay aggregates are coated with bitumen. The presence of non-uniform bitumen coating is also further reinforced (Mercier et al., 2012).

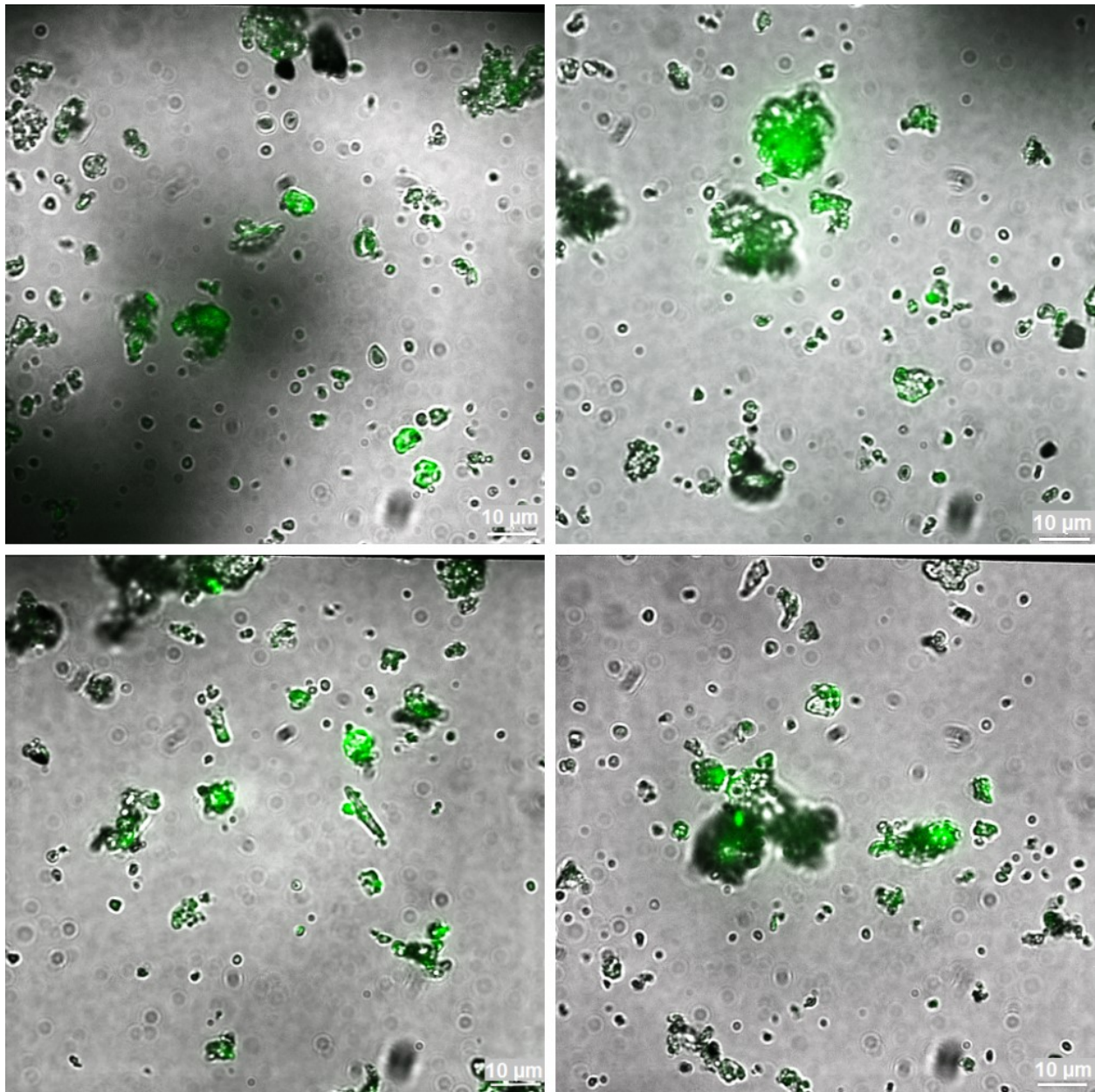


Figure 4-9: These superimposed bright field and TIRF images of Syncrude MFT 2014 after deaerating was performed on it. These images show the presence of low percentage of bitumen still present in the dried solids after the deaerating. This represents the difficulty of removing bitumen.

4.3.3 Post Dean Stark Analysis Imaging

Post dean stark imaging was performed on the leftover solids in the thimble from 8 hours dean stark analysis. Toluene was allowed to evaporate from these solids. The aim of this exercise was to image bitumen which is strongly associated with clay and is difficult to recover during extraction process (Wallwork, Xu, & Masliyah, 2003)(Ding, Repka, Xu, & Masliyah, 2006). These images were observed for presence of specific structure or change in excitation or emission wavelength. The TIRF images were superimposed with bright field images to get a better idea about their relative distribution as seen in *Figure 4-9* A significant reduction in fluorescence intensity was observed. Hence these images were digitally brightened. This shows that very low percentage of bitumen remained in these solids. Negligible change in the excitation and emission wavelength were observed. No repeating or specific shapes of bitumen coating were observed in these samples at this resolution.

4.4 Conclusion

In order to reduce the economic and environmental impact of tailings, research is being performed to reduce its reclamation time to the order of weeks, recycle water while it is still at process temperature and reduce the amount of additional fresh water requirement. Multiple studies have advised that bitumen in tailings has detrimental effect on the aggregation and consolidation of clays in tailings. High resolution electron microscopes have been used to understand the clay and bitumen interaction. Since these techniques are inorganic material specific, they can only infer the bitumen location. The first ever TIRF tomography performed in this study, has paved way towards clear visualization of bitumen location and interaction in MFT.

The results from this study, confirm the presence of hydrophobic and biwetable clay aggregate by showing the presence clay surfaces which are fully as well as partially coated with bitumen. These images give evidence of the presence of non-uniform bitumen coating on the clay surface. The images from CLSM supported these conclusions. The well type slides ensure that these samples are imaged in their original state.

By imaging MFT solids after dean stark, the difficult to recover bitumen which strongly associates with problem clays could be seen. The fluorescence intensity of these images was very low but

there was no noticeable shift in the excitation or emission wavelength. No specific repeating shapes or structure of bitumen coating could be observed at this 0.3 μm resolution.

Collaboratively studying MFT samples with TIRF and other high resolution techniques such as He-ion microscopy which allows imaging with minimal sample alteration and gives sub-nanometer resolution, targeted study of clay surface with partial bitumen coating can be performed. This will aid in realizing whether the basal plane or edge on clay surface is interacting with bitumen. This will give better understanding about the bitumen–clay interactions in MFT and help in development of improved tailings treatments and/ or polymer flocculants.

4.5 References

- Adegoroye, A., Wang, L., Omotoso, O., Xu, Z., & Masliyah, J. (2010). Characterization of organic-coated solids isolated from different oil sands. *Canadian Journal of Chemical Engineering*, 88(3), 462–470. doi:10.1002/cjce.20294
- Arbor, A. (1986). Transmission and Analytical Electron Microscopy of the Smectite-To-Illite Transition. *Clays and Clay Minerals*, 34(2), 165–179.
- Bertouche, S., Tomao, V., Ruiz, K., Hellal, A., Boutekedjiret, C., & Chemat, F. (2012). First approach on moisture determination in food products using alpha-pinene as an alternative solvent for Dean-Stark distillation. *Food Chemistry*, 134(1), 602–605. doi:10.1016/j.foodchem.2012.02.158
- Bichard, J. A. (1987). Oil sands composition and behaviour research the research papers of John A. Bichard 1957-1965. Alta: AOSTRA.
- Chalaturnyk, R. J., & Scott, D. (2002). Management of oil sands tailings. *Petroleum Science and Technology*, 20, 1025–1046.
- Chow, R., McKenna, G., Win, S. M. K., & Journault, J. (2014). Recovery of bitumen from oil sands tailings streams and deposits: Potential opportunities and benefits. Retrieved from http://www.ai-ees.ca/media/12375/aitf_bgc_bitumen_from_tailings_for_ae-ees_and_cosia_dec__2013.pdf

- Dang-Vu, T., Jha, R., Wu, S.-Y., Tannant, D. D., Masliyah, J., & Xu, Z. (2009b). Effect of solid wettability on processability of oil sands ores. *Energy Fuels*, 23(5), 2628–2636. doi:10.1021/ef9000117
- Ding, X., Repka, C., Xu, Z., & Masliyah, J. (2006). Effect of Illite Clay and Divalent Cations on Bitumen Recovery. *The Canadian Journal of Chemical Engineering*, 84(December), 643–650. doi:10.1002/cjce.5450840602
- Fine Tailings Fundamentals Consortium Alberta Energy. (1995). *Advances in oil sands tailings research*. Edmonton, Alta: Alberta Dept. of Energy.
- Geddes, C. D., & Lakowicz, J. R. (2006). *Reviews in fluorescence*. Springer.
- Hooshiar, A., Uhlik, P., Ivey, D. G., Liu, Q., & Etsell, T. H. (2012). Clay minerals in nonaqueous extraction of bitumen from Alberta oil sands: Part 2. Characterization of clay minerals. *Fuel Processing Technology*, 96, 183–194. doi:10.1016/j.fuproc.2011.10.010
- Johnston, C. T. (2010). Probing the nanoscale architecture of clay minerals. *Clay Minerals*, 45(3), 245–279. doi:10.1180/claymin.2010.045.3.245
- Kaminsky, H., Etsell, T., Ivey, D. G., & Omotoso, O. (2006). Fundamental particle size of clay minerals in athabasca oil sands tailings. *Clay Science*, 12, 217–222.
- Kudalkar, E. M., Davis, T. N., & Asbury, C. L. (2016). Single-Molecule Total Internal Reflection Fluorescence Microscopy. *Cold Spring Harbor Protocols*, 2016(5), pdb.top077800. doi:10.1101/pdb.top077800
- Li, H., Long, J., Xu, Z., & Masliyah, J. H. (2008). Novel polymer aids for low-grade oil sand ore processing. *Can. J. Chem. Eng.*, 86(Copyright (C) 2010 American Chemical Society (ACS). All Rights Reserved.), 168–176. doi:10.1002/cjce.20030
- Liu, H., Tan, S., Yu, T., & Liu, Y. (2015). Sulfate reducing bacterial community and in situ activity in mature fine tailings analyzed by real time qPCR and microsensor. *Journal of Environmental Sciences (China)*, 44, 141–147. doi:10.1016/j.jes.2015.08.025

- Liu, J., Xu, Z., & Masliyah, J. (2004). Role of fine clays in bitumen extraction from oil sands. *AIChE Journal*, 50(8), 1917–1927. doi:10.1002/aic.10174
- Masliyah, J., Zhou, Z. J., Xu, Z., Czarnecki, J., & Hamza, H. (2004). Understanding Water-Based Bitumen Extraction from Athabasca Oil Sands. *The Canadian Journal of Chemical Engineering*, 82(4), 628–654. doi:10.1002/cjce.5450820403
- Masliyah, Jacob H. (Jacob Heskell), Xu, Z. (Zhenghe), Czarnecki, Jan A. (Jan Adam), Dabros, M. (2011). *Handbook on theory and practice of bitumen recovery from Athabasca Oil Sands (volume 1:)*. Kingsley Knowledge Publishing.
- Mattheyses, A. L., Simon, S. M., & Rappoport, J. Z. (2010). Imaging with total internal reflection fluorescence microscopy for the cell biologist. *Journal of Cell Science*, 123(Pt 21), 3621–8. doi:10.1242/jcs.056218
- Mercier, P. H. J., Ng, S., Moran, K., Sparks, B. D., Kingston, D., Kotlyar, L. S., ... McCracken, T. (2012). Colloidal Clay Gelation: Relevance to Current Oil Sands Operations. *Petroleum Science and Technology*, 30(April 2015), 915–923. doi:10.1080/10916466.2010.495959
- Mikula, R. J., & Munoz, V. a. (2000). Characterization of emulsions and suspensions in the petroleum industry using cryo-SEM and CLSM. *Colloids and Surfaces A: Physicochemical and Engineering Aspects*, 174, 23–36. doi:10.1016/S0927-7757(00)00518-5
- Moore, D. M. (1997). *X-ray diffraction and the identification and analysis of clay minerals*, 2nd ed. Oxford: Oxford University Press.
- Omotoso, O. E., Munoz, V. A., & Mikula, R. J. (2002). Mechanisms of Crude Oil-Mineral Interactions. *Spill Science and Technology Bulletin*, 8(1), 45–54. doi:10.1016/S1353-2561(02)00116-0
- Paddock, S. W. (1999). Confocal laser scanning microscopy. *Biotechniques*, 27, 992–1007.
- Schneckenburger, H. (2005). Total internal reflection fluorescence microscopy: Technical innovations and novel applications. *Current Opinion in Biotechnology*, 16(1 SPEC. ISS.), 13–18. doi:10.1016/j.copbio.2004.12.004

- Shende, S., Pendharker, S., Nazemifard, N., & Jacob, Z. (2016). Total Internal Reflection Fluorescence Microscopy To Investigate the Distribution of Residual Bitumen in Oil Sands Tailings. *Energy & Fuels*.
- Sparks, B. D., Kotlyar, L. S., Carroll, J. B., & Chung, K. H. (2003). Athabasca oil sands: Effect of organic coated solids on bitumen recovery and quality. *Journal of Petroleum Science and Engineering*, 39(3-4), 417–430. doi:10.1016/S0920-4105(03)00080-9
- Takamura, K. (1982). Microscopic structure of Athabasca oil sand. *Canadian Journal of Chemical Engineering*, 60(4), 538–545.
- Tombacz, E., & Szekeres, M. (2006). Surface charge heterogeneity of kaolinite in aqueous suspension in comparison with montmorillonite. *Applied Clay Science*, 34(1-4), 105–124. doi:10.1016/j.clay.2006.05.009
- Wallwork, V., Xu, Z., & Masliyah, J. (2003). Bitumen Recovery with Oily Air Bubbles. *The Canadian Journal of Chemical Engineering*, 81(5), 993–997. Retrieved from <http://dx.doi.org/10.1002/cjce.5450810510>

Chapter 5: Conclusion and future work

To study bitumen-clay interaction in MFT samples, samples from Syncrude 2012 tailings, Syncrude 2014 tailings and CNRL 2016 tailings were investigated with Total Internal reflection Fluorescence (TIRF) microscope and other support techniques such as spectrofluorometer, confocal fluorescence microscope and Confocal Laser Scanning Microscope (CLSM). MFT samples diluted with deionised water and process water were also observed using bright field microscope to get better idea about clay boundaries.

Spectrofluorometer provided information regarding bitumen fluorescence excitation and emission spectrum. These results helped to narrow down suitable laser source and filter cube for other fluorescence microscopes.

Experiments were started with confocal fluorescence microscope to observe extracted bitumen samples provided by IOSI. Bitumen gave best images with the 488nm laser and corresponding filter cube. Bitumen-water and bitumen-clay interface samples were also made and observed to ensure that these interfaces could be clearly seen using fluorescence methods.

First ever TIRF images of MFT and dilute MFT were presented in this study. Imaging at angles above critical angle gave high clarity for near surface features. Reducing the laser intensity made it possible to see minute features inside and near boundaries of fluorescence particles which were formerly dabbed out from high glare due to fluorescence from these particles. CLSM supported the conclusions drawn from the TIRF images. Following major conclusions were drawn from this work:

- Hydrophilic clay were clearly seen in the superimposed images from TIRF and bright field taken at same location in the sample.
- Rough calculation for bitumen coating thickness on clay gave a ballpark value of 230nm.
- Oleophilic clay were also observed in these superimposed images. These clays were completely coated with bitumen. This could be confirmed with 3-D constructions from TIRF 2-D z-stack images. These types of clays have been identified in literature as problem clays.

- It was evident that bitumen was bridging many clay aggregates. This phenomena where bitumen bridges clay aggregates has been suspected to be responsible for increase in tailings viscosity and hence delay their settling.
- Clay surfaces with partial bitumen coverage were noted in the MFT and dilute MFT samples. These surfaces were carefully reconstructed using image processing techniques to get better visuals. This tomography proved the presence of biwetttable clays. These images showed that clay surface properties vary.

Possible future progress in research can be stated as follows:

- By correlative studies of the partially bitumen coated surfaces using inorganic specific techniques such as he-ion microscope, information can be obtained about their surface properties.
- The real-time imaging possibility of TIRF can be used to obtain real-time videos of change in aggregation speed and aggregate size of clays in MFT with variation of ambient condition and flocculants. Its impact variation of ambient condition and flocculants can also be studied on bitumen-clay attachment.
- Resolution of TIRF can be improved to nanoscale with the help of plasmonic substrate in which our group has experience.
- Analysis can be performed to obtain the percentage of bitumen which is in the bulk of clay. This information will provide data about impact of bitumen attachment on delamination of clays.
- Dilute MFT samples show Brownian motion. The relative speed of various particles can be considered to find if the particles is bitumen coat clay/ free bitumen/ uncoated clay.

References (All)

- Adegoroye, A., Wang, L., Omotoso, O., Xu, Z., & Masliyah, J. (2010). Characterization of organic-coated solids isolated from different oil sands. *Canadian Journal of Chemical Engineering*, 88(3), 462–470. doi:10.1002/cjce.20294
- Alberta issuing body. (2015). *Lower Athabasca Region: tailings management framework for the mineable Athabasca oil sands*. Edmonton: Government of Alberta.
- Amann, K. J., & Pollard, T. D. (2001). Direct real-time observation of actin filament branching mediated by Arp23 complex using total internal reflection fluorescence microscopy. *Pnas*, 98(26), 15009–15013.
- Arbor, A. (1986). Transmission and Analytical Electron Microscopy of the Smectite-To-Illite Transition. *Clays and Clay Minerals*, 34(2), 165–179.
- Axelrod, D. (2014). *Evanescent Excitation and Emission. Fluorescence Microscopy: Super-Resolution and other Novel Techniques*. Elsevier Inc. doi:10.1016/B978-0-12-409513-7.00001-4
- Bearsley, S., Forbes, a., & Haverkamp, R. G. (2004). Direct observation of the asphaltene structure in paving-grade bitumen using confocal laser-scanning microscopy. *Journal of Microscopy*, 215(August), 149–155. doi:10.1111/j.0022-2720.2004.01373.x
- Bertouche, S., Tomao, V., Ruiz, K., Hellal, A., Boutekedjiret, C., & Chemat, F. (2012). First approach on moisture determination in food products using alpha-pinene as an alternative solvent for Dean-Stark distillation. *Food Chemistry*, 134(1), 602–605. doi:10.1016/j.foodchem.2012.02.158
- Bichard, J. A. (1987). *Oil sands composition and behaviour research the research papers of John A. Bichard 1957-1965*. Alta: AOSTRA.
- Boulanger, J., Gueudry, C., Münch, D., Cinquin, B., Paul-Gilloteaux, P., Bardin, S., ... Salamero, J. (2014). Fast high-resolution 3D total internal reflection fluorescence microscopy by incidence angle scanning and azimuthal averaging. *Proceedings of the National Academy of Sciences of the United States of America*, 111(48), 17164–9.

doi:10.1073/pnas.1414106111

- Boxill, L. (2011). Potential for use of methylene blue index testing to enhance geotechnical characterization of oil sands ores and tailings. *Proceedings of Tailings and Mine Waste*.
- Brandt, M. (2010). Spectrofluorometers and Fluorescence Phenomena. Retrieved January 1, 2015, from http://loci.wisc.edu/files/loci/Introduction_to_Spectrofluorometry.pdf
- Butler, R. M., & Mokrys, I. J. (1998). Closed-loop extraction method for the recovery of heavy oils and bitumens underlain by aquifers: The vapex process. *Journal of Canadian Petroleum Technology*, 37(4), 41–50. doi:10.2118/98-04-04
- Camp, F. W. (1976). *The Tar Sands of Alberta, Canada 3rd ed.* Cameron Engineers Denver.
- Caughill, D. L., Morgenstern, N., & Scott, J. (1993). Geotechnics of nonsegregating oil sand tailings. *Canadian Geotechnical Journal*, 30(5), 801–811.
- Chalaturnyk, R. J., & Scott, D. (2002). Management of oil sands tailings. *Petroleum Science and Technology*, 20, 1025–1046.
- Chow, R., McKenna, G., Win, S. M. K., & Journault, J. (2014). *Recovery of bitumen from oil sands tailings streams and deposits: Potential opportunities and benefits*. Retrieved from http://www.ai-ees.ca/media/12375/aitf_bgc_bitumen_from_tailings_for_ae-ees_and_cosia_dec__2013.pdf
- Clementz, D. M. (1976). Interaction of petroleum heavy ends with montmorillonite. *Clays and Clay Minerals*, 24(6), 312–319. doi:10.1346/CCMN.1976.0240607
- COSIA. (n.d.-a). Composite Tailings Process Addresses Challenging Tailings Material. Retrieved from <http://www.cosia.ca/uploads/files/Media Resources/Media Kit/Composite Tailings Process Addresses Challenging Tailings Material.pdf>
- COSIA. (n.d.-b). Tailings Reduction Technology. Retrieved from <http://www.cosia.ca/tailings-reduction-technology>
- Dang-Vu, T., Jha, R., Wu, S. Y., Tannant, D. D., Masliyah, J., & Xu, Z. (2009a). Wettability determination of solids isolated from oil sands. *Colloids and Surfaces A: Physicochemical*

- and Engineering Aspects*, 337(1-3), 80–90. doi:10.1016/j.colsurfa.2008.11.055
- Dang-Vu, T., Jha, R., Wu, S.-Y., Tannant, D. D., Masliyah, J., & Xu, Z. (2009b). Effect of solid wettability on processability of oil sands ores. *Energy Fuels*, 23(5), 2628–2636. doi:10.1021/ef9000117
- Ding, X., Repka, C., Xu, Z., & Masliyah, J. (2006). Effect of Illite Clay and Divalent Cations on Bitumen Recovery. *The Canadian Journal of Chemical Engineering*, 84(December), 643–650. doi:10.1002/cjce.5450840602
- Dobrucki, J. W. (2013). *Fluorescence Microscopy. Fluorescence Microscopy- From Principles to Biological Applications*. doi:10.1002/9783527671595
- Dyer, S., & Huot, M. (2010). Mining vs In Situ Fact Sheet. What is the highest environmental impact oil? *Pembina Institute*. Retrieved from <https://www.pembina.org/reports/mining-vs-in-situ.pdf>
- Fine Tailings Fundamental Consortium and Alberta. Dept. of Energy. Oil Sands and Research Division and others. (1995). *Advances in oil sands tailings research*. Edmonton: Alberta Dept. of Energy.
- Fine Tailings Fundamentals Consortium Alberta Energy. (1995). *Advances in oil sands tailings research*. Edmonton, Alta: Alberta Dept. of Energy.
- Fine Tailings Symposium (1993 : Edmonton, A. (1993). *Oil Sands : Our Petroleum Future Conference Proceedings*.
- Folwell, B. D., McGenity, T. J., Price, A., Johnson, R. J., & Whitby, C. (2014). Exploring the capacity for anaerobic biodegradation of polycyclic aromatic hydrocarbons and naphthenic acids by microbes from oil-sands-process-affected waters. *International Biodeterioration and Biodegradation*, 108, 214–221. doi:10.1016/j.ibiod.2014.12.016
- Franco, J. C., Gonçalves, G., Souza, M. S., Rosa, S. B. C., Thiegue, L. M., Atvars, T. D. Z., ... Nome, R. A. (2013). Towards in situ fluorescence spectroscopy and microscopy investigations of asphaltene precipitation kinetics. *Optics Express*, 21(25), 30874. doi:10.1364/OE.21.030874

- Geddes, C. D., & Lakowicz, J. R. (2006). *Reviews in fluorescence*. Springer.
- Gray, M. R. (1998). *Extraction and upgrading of oilsands bitumen: Intensive short course*. University of Alberta Edmonton.
- Gregory, J., & Barany, S. (2011). Adsorption and flocculation by polymers and polymer mixtures. *Advances in Colloid and Interface Science*, 169(1), 1–12.
doi:10.1016/j.cis.2011.06.004
- Hall, G. (1989). Correction of Polychromatic Luminescence Signals for Inner-Filter Effects. *Applied Spectroscopy*, 43(5), 759–767.
- Hande, Aharnish. *Accelerated Dewatering and Drying Treatment of Oil Sands Tailings by Electrical Resonant Auto-Transformer*. Master of Science Dissertation, University of Alberta, Canada. (2014). University of Alberta.
- Harris, M., Hill, C., & Vaughan, J. (1994). Optical helices and spiral interference fringes. *Optics Communications*, 106(4), 161–166.
- Hepler, L. G., & Smith, R. G. (1994). *Alberta oil sands: Industrial procedures for extraction and some recent fundamental research*.
- Holden, A. A., Haque, S. E., Mayer, K. U., & Ulrich, A. C. (2013). Biogeochemical processes controlling the mobility of major ions and trace metals in aquitard sediments beneath an oil sand tailing pond: Laboratory studies and reactive transport modeling. *Journal of Contaminant Hydrology*. doi:10.1016/j.jconhyd.2013.04.006
- Hooshar, A., Uhlík, P., Ivey, D. G., Liu, Q., & Etsell, T. H. (2012). Clay minerals in nonaqueous extraction of bitumen from Alberta oil sands: Part 2. Characterization of clay minerals. *Fuel Processing Technology*, 96, 183–194. doi:10.1016/j.fuproc.2011.10.010
- Hooshar, A., Uhlík, P., Kaminsky, H. W., Shinbine, A., Omotoso, O., Liu, Q., ... Etsell, T. H. (2010). High resolution transmission electron microscopy study of clay mineral particles from streams of simulated water based bitumen extraction of Athabasca oil sands. *Applied Clay Science*, 48(3), 466–474. doi:10.1016/j.clay.2010.02.008

- Hooshiar Fard, M. A. (2011). *Characterization of Clay Minerals in the Athabasca Oil Sands in Water Extraction and Nonaqueous Solvent Extraction Processes (PhD Thesis)*. University of Alberta.
- Hung, J., Castillo, J. A., & Reyes, A. (2004). Colloidal structural evolution of asphaltene studied by confocal microscopy, *5622*, 154–159. doi:10.1117/12.591036
- Ignasiak, T. M., Kotlyar, L., Longstaffe, F. J., Strausz, O. P., & Montgomery, D. S. (1983). Separation and characterization of clay from Athabasca asphaltene. *Fuel*, *62*(3), 353–362.
- Ishikawa-Ankerhold, H. C., Ankerhold, R., & Drummen, G. P. C. (2012). Advanced Fluorescence Microscopy Techniques—FRAP, FLIP, FLAP, FRET and FLIM. *Molecules*, *17*(12), 4047–4132. doi:10.3390/molecules17044047
- Johnston, C. T. (2010). Probing the nanoscale architecture of clay minerals. *Clay Minerals*, *45*(3), 245–279. doi:10.1180/claymin.2010.045.3.245
- Kaminsky, H. A. W., Etsell, T. H., Ivey, D. G., & Omotoso, O. (2009). Distribution of clay minerals in the process streams produced by the extraction of bitumen from Athabasca oil sands. *The Canadian Journal of Chemical Engineering*, *87*(1), 85–93. doi:10.1002/cjce.20133
- Kaminsky, H., Etsell, T., Ivey, D. G., & Omotoso, O. (2006). Fundamental particle size of clay minerals in athabasca oil sands tailings. *Clay Science*, *12*, 217–222.
- Kasperski, K. L. (2001). *Review of research on aqueous extraction of bitumen from mined oil sands*. Edmonton, Alta: CANMET, Western Research Centre.
- Kaura, A. (2014). *Understanding and Developing New Methods for Treating Oil Sands Tailings*. University of Alberta.
- Khursheed, A. (2011). *Scanning Electron Microscope Optics And Spectrometers*. World Scientific Publishing Company.
- Klein, C., Harbottle, D., Alagha, L., & Xu, Z. (2013). Impact of fugitive bitumen on polymer-based flocculation of mature fine tailings. *The Canadian Journal of Chemical Engineering*,

91(8), 1427–1432.

- Klein, Colin. *Effect of Residual Bitumen on Polymer-assisted Flocculation of Fluid Fine Tailings*. Master of Science Dissertation, University of Alberta, Canada. (2014). University of Alberta, Canada.
- Knight, A. E. (2014). Single-molecule fluorescence imaging by total internal reflection fluorescence microscopy (IUPAC Technical Report). *Pure and Applied Chemistry*, 86(8), 1303–1320. doi:10.1515/pac-2012-0605
- Kotlyar, L., Sparks, B., LePage, Y., & Woods, J. (1998). Effect of Particle Size on Clay Flocculation Behavior of Ultra-Fine Clays in Salt Solutions. *Clay Minerals*, 33(1), 103–107.
- Krishnan, R. V, Varma, R., & Mayor, S. (2001). Fluorescence methods to probe nanometre-scale organization of molecules in living cell membranes. *J. Fluor.*, 11(3), 211–226.
- Kudalkar, E. M., Davis, T. N., & Asbury, C. L. (2016). Single-Molecule Total Internal Reflection Fluorescence Microscopy. *Cold Spring Harbor Protocols*, 2016(5), pdb.top077800. doi:10.1101/pdb.top077800
- Li, H., Long, J., Xu, Z., & Masliyah, J. H. (2008). Novel polymer aids for low-grade oil sand ore processing. *Can. J. Chem. Eng.*, 86(Copyright (C) 2010 American Chemical Society (ACS). All Rights Reserved.), 168–176. doi:10.1002/cjce.20030
- Liu, H., Tan, S., Yu, T., & Liu, Y. (2015). Sulfate reducing bacterial community and in situ activity in mature fine tailings analyzed by real time qPCR and microsensor. *Journal of Environmental Sciences (China)*, 44, 141–147. doi:10.1016/j.jes.2015.08.025
- Liu, J., Xu, Z., & Masliyah, J. (2004). Role of fine clays in bitumen extraction from oil sands. *AIChE Journal*, 50(8), 1917–1927. doi:10.1002/aic.10174
- Majid, A., & Sparks, B. D. (1996). Role of hydrophobic solids in the stability of oil sands fine tailings. *Fuel*, 75(7), 879–884.
- Marshall, G. M., Kingston, D. M., Moran, K., & Mercier, P. H. J. (2013). Multivariate factor analysis of heavy minerals concentrate from Athabasca oil sands tailings by X-ray

- photoelectron spectroscopy. *Surface and Interface Analysis*, (November 2012), n/a–n/a. doi:10.1002/sia.5201
- Masliyah, J., Zhou, Z. J., Xu, Z., Czarnecki, J., & Hamza, H. (2004). Understanding Water-Based Bitumen Extraction from Athabasca Oil Sands. *The Canadian Journal of Chemical Engineering*, 82(4), 628–654. doi:10.1002/cjce.5450820403
- Masliyah, Jacob H. (Jacob Heskell), Xu, Z. (Zhenghe), Czarnecki, Jan A. (Jan Adam), Dabros, M. (2011). *Handbook on theory and practice of bitumen recovery from Athabasca Oil Sands* (volume 1:). Kingsley Knowledge Publishing.
- Matthews, J., Shaw, W., MacKinnon, M., & Cuddy, R. (2002). Development of composite tailings technology at Syncrude. *International Journal of Surface Mining, Reclamation and Environment*, 16(1), 24–39.
- Mattheyses, A. L., Simon, S. M., & Rappoport, J. Z. (2010). Imaging with total internal reflection fluorescence microscopy for the cell biologist. *Journal of Cell Science*, 123(Pt 21), 3621–8. doi:10.1242/jcs.056218
- McFadyen, D. (2009). Directive 074: Tailings Performance Criteria and Requirements for Oil Sands Mining Schemes. *Energy Resources Conservation Board, Calgary, AB, Canada*.
- Meadus, F., Chevrier, P., & Sparks, B. (1982). Solvent extraction of athabasca oil-sand in a rotating mill Part 1. Dissolution of bitumen. *Fuel Processing Technology*, 6(3), 277–287.
- Mercier, P. H. J., Ng, S., Moran, K., Sparks, B. D., Kingston, D., Kotlyar, L. S., ... McCracken, T. (2012). Colloidal Clay Gelation: Relevance to Current Oil Sands Operations. *Petroleum Science and Technology*, 30(April 2015), 915–923. doi:10.1080/10916466.2010.495959
- Mikula, R. J., & Munoz, V. a. (2000). Characterization of emulsions and suspensions in the petroleum industry using cryo-SEM and CLSM. *Colloids and Surfaces A: Physicochemical and Engineering Aspects*, 174, 23–36. doi:10.1016/S0927-7757(00)00518-5
- Mikula, R., & Omotoso, O. (2006). Role of Clays in Controlling Oil Sands Tailings Processing Behaviour in Oil Sands Processing. *Clay Science*, 12(2), 177–182. doi:10.11362/jcssjclayscience1960.12.Supplement2_177

- Mondal, P. P. (2014). *Fundamentals of fluorescence microscopy: exploring life with light. Statewide Agricultural Land Use Baseline 2015* (Vol. 1). Dordrecht: Springer.
- Moore, D. M. (1997). *X-ray diffraction and the identification and analysis of clay minerals, 2nd ed.* Oxford: Oxford University Press.
- Mpofu, P., Addai-Mensah, J., & Ralston, J. (2003). Investigation of the effect of polymer structure type on flocculation, rheology and dewatering behaviour of kaolinite dispersions. *International Journal of Mineral Processing*, 71(1-4), 247–268. doi:10.1016/S0301-7516(03)00062-0
- Muñoz, V. a., Kasperski, K. L., Omotoso, O. E., & Mikula, R. J. (2003). The Use of Microscopic Bitumen Froth Morphology for the Identification of Problem Oil Sand Ores. *Petroleum Science and Technology*, 21(9-10), 1509–1529. doi:10.1081/LFT-120023225
- Nazemifard, N., Bhattacharjee, S., JH, M., & DJ, H. (2013). Nonmonotonous variation of DNA angular separation during asymmetric pulsed field electrophoresis. *Electrophoresis*, 34 (17), 2453–2463. doi:10.1002/elps.201300152
- Omotoso, O. E., Munoz, V. A., & Mikula, R. J. (2002). Mechanisms of Crude Oil-Mineral Interactions. *Spill Science and Technology Bulletin*, 8(1), 45–54. doi:10.1016/S1353-2561(02)00116-0
- Osacky, M., Geramian, M., Dyar, M. D., Sklute, E. C., Valter, M., Ivey, D. G., ... Etsell, T. H. (2013). Characterisation of petrologic end members of oil sands from the Athabasca region, Alberta, Canada. *The Canadian Journal of Chemical Engineering*, 9(June), 1–14. doi:10.1002/cjce.21860
- Osacky, M., Geramian, M., Ivey, D. G., Liu, Q., & Etsell, T. H. (2015). Influence of Nonswelling Clay Minerals (Illite, Kaolinite, and Chlorite) on Nonaqueous Solvent Extraction of Bitumen. *Energy & Fuels*, 29(7), 4150–4159. doi:10.1021/acs.energyfuels.5b00269
- Paddock, S. W. (1999). Confocal laser scanning microscopy. *Biotechniques*, 27, 992–1007.
- Powter, C., Biggar, K., Silva, M., McKenna, G., & Scordo, E. (2011). *Review of oil sands*

tailings technology options.

- R. Starko-Bowes, J. Atkinson, W. Newman, H. Hu, T. Kallos, G. Palikaras, R. Fedosejevs, S. Pramanik, Jacob, Z. (2015). Optical characterization of epsilon-near-zero, epsilon-near-pole, and hyperbolic response in nanowire metamaterials. *Journal of the Optical Society of America B*, 32(10), 2074–2080. doi:10.1364/JOSAB.32.002074
- Schneckenburger, H. (2005). Total internal reflection fluorescence microscopy: Technical innovations and novel applications. *Current Opinion in Biotechnology*, 16(1 SPEC. ISS.), 13–18. doi:10.1016/j.copbio.2004.12.004
- Schramm, L. L., & Smith, R. G. (1985). The influence of natural surfactants on interfacial charges in the hot-water process for recovering bitumen from the Athabasca oil sands. *Colloids and Surfaces*, 14(1), 67–85.
- Scott, A. C., MacKinnon, M. D., & Fedorak, P. M. (2005). Naphthenic acids in athabasca oil sands tailings waters are less biodegradable than commercial naphthenic acids. *Environmental Science and Technology*, 39(21), 8388–8394. doi:10.1021/es051003k
- Scott, J. D., Dusseault, M. B., & Carrier, W. D. (1985). Behaviour of the clay/bitumen/water sludge system from oil sands extraction plants. *Applied Clay Science*, 1(1-2), 207–218.
- Sepulveda, J., & Miller, J. D. (1978). Separation Of Bitumen From Utah Tar Sands By A Hot Water Digestion-Flotation Technique. *Min. Eng*, 30(9), 1311–1320.
- Seward, G. H. (2010). *Optical Design of Microscopes*. Bellingham, Wash. (1000 20th St. Bellingham WA 98225-6705 USA): SPIE.
- Shen, H., Huang, E., Das, T., Xu, H., Ellisman, M., & Liu, Z. (2014). TIRF microscopy with ultra-short penetration depth. *Optics Express*, 22(9), 10728–34. doi:10.1364/OE.22.010728
- Shende, S., Pendharker, S., Nazemifard, N., & Jacob, Z. (2016). Total Internal Reflection Fluorescence Microscopy To Investigate the Distribution of Residual Bitumen in Oil Sands Tailings. *Energy & Fuels*.
- Sparks, B. D., Kotlyar, L. S., Carroll, J. B., & Chung, K. H. (2003). Athabasca oil sands: Effect

- of organic coated solids on bitumen recovery and quality. *Journal of Petroleum Science and Engineering*, 39(3-4), 417–430. doi:10.1016/S0920-4105(03)00080-9
- Stasiuk, L. D., Gentzis, T., & Rahimi, P. (2000). Application of spectral fluorescence microscopy for the characterization of Athabasca bitumen vacuum bottoms. *Fuel*, 79(7), 769–775. doi:10.1016/S0016-2361(99)00198-2
- Stolojan, V. (2015). *Nanometrology Using the Transmission Electron Microscope*. Morgan & Claypool Publishers Institute of Physics.
- Takamura, K. (1982). Microscopic structure of Athabasca oil sand. *Canadian Journal of Chemical Engineering*, 60(4), 538–545.
- Tamiz Bakhtiari, M., Harbottle, D., Curran, M., Ng, S., Spence, J., Siy, R., ... Xu, Z. (2015). Role of Caustic Addition in Bitumen–Clay Interactions. *Energy & Fuels*, 29(1), 58–69. doi:10.1021/ef502088z
- Tombacz, E., & Szekeres, M. (2006). Surface charge heterogeneity of kaolinite in aqueous suspension in comparison with montmorillonite. *Applied Clay Science*, 34(1-4), 105–124. doi:10.1016/j.clay.2006.05.009
- Van Olphen, H. (1991). *An introduction to clay colloid chemistry: for clay technologists, geologists, and soil scientists, 2nd ed.* Malabar, FL: Krieger Publishing Co.
- Wallwork, V., Xu, Z., & Masliyah, J. (2003). Bitumen Recovery with Oily Air Bubbles. *The Canadian Journal of Chemical Engineering*, 81(5), 993–997. Retrieved from <http://dx.doi.org/10.1002/cjce.5450810510>
- Wang, X. W., Feng, X., Xu, Z., & Masliyah, J. H. (2010). *Polymer aids for settling and filtration of oil sands tailings*. *Canadian Journal of Chemical Engineering* (Vol. 88). doi:10.1002/cjce.20283
- Webb, D. J., & Brown, C. M. (2013). Epi-Fluorescence Microscopy. doi:10.1007/978-1-62703-056-4_2
- Xia, T. X., Greaves, M., Turta, A. T., & Ayasse, C. (2003). THAI-A “Short-distance

Displacement” In Situ Combustion Process for the Recovery and Upgrading of Heavy Oil. *Oil and Natural Gas Production*, 81(March).

Yang, W. Y., Qian, J. W., & Shen, Z. Q. (2004). A novel flocculant of Al(OH)₃-polyacrylamide ionic hybrid. *Journal of Colloid and Interface Science*, 273(2), 400–405.
doi:10.1016/j.jcis.2004.02.002

Yin, X., & Miller, J. D. (2012). Wettability of kaolinite basal planes based on surface force measurements using atomic force microscopy. *Minerals & Metallurgical Processing*, 29(1), 8.

Appendix A: Sample Preparation for Spectrofluorometer and fluorescence microscope

Liquid samples give the best results for the spectrofluorometer. It also gives better results for dilute sample. If the sample is not diluted, quenching of fluorophores results in inaccurate resulting spectrums. The samples were prepared using the following method:

- A vial provided by the manufacturer was used for the observation of the sample. This vial could hold 4 ml of the sample.
- Three samples of dilute bitumen with different concentration were made.
- First sample was mixed with toluene for a concentration of 0.1 g/L. About 4 ml of this sample was added to the vial.
- Similarly samples with concentrations of 0.1, 0.3, and 0.5 g/L bitumen in toluene were made.

Sample preparation for TIRF and confocal fluorescence microscope for dry samples involved the following steps:

- Since both these microscopes were inverted epi-fluorescence type microscopes, the samples needed to be placed on the glass cover instead of glass slide. Placing the sample on glass cover, ensured that there was no air gap between the sample and glass.
- Bitumen samples were prepared by carefully placing thin strand of bitumen using a spatula. Thin strands mainly helped in imaging with the bright field. Since bright field imaging is done in transmission mode, thick opaque samples are hard to image. Bright field images provided a visual confirmation for the fluorescence images. Since Fluorescence microscopy techniques worked in the epi-fluorescence mode hence even a thick bitumen sample can be easily imaged. The glass cover was covered with the glass slide to protect the sample and equipment before observing it under the microscope.
- Model clay samples were prepared by sprinkling the model clay on the glass slide. In this case again, a thin layer was mainly important for bright field imaging. The glass cover was covered with glass slide. Since this sample was powder, glass slide was secured on the glass

cover using super-glue. It was ensured that the small quantity of glue was used. It did not reach the sample and contaminate it.

- Model clay and bitumen interface samples were prepared by placing strand of bitumen on the glass cover with a spatula. Then some model clay powder was added near the bitumen strand. The sample was carefully covered with glass slide and secured in place with super-glue.
- Water and bitumen interface samples were also prepared by placing a strand of bitumen on the glass cover with spatula. A drop of water was then added near bitumen. This slide was observed without placing the glass slide, to prevent the sample from getting altered.
- MFT samples were prepared by adding a drop of MFT to the glass cover. Allowing it to dry for about 10 minutes and then covering it carefully with glass slide.
- Dilute MFT samples were prepared by first preparing the dilute MFT sample using a known quantity of DI water and MFT and mixing them using manual agitation. Then a drop of this sample is added to the glass cover. It is allowed to dry for as long as it takes. Then it is covered with glass slide and securing with super-glue.

Since dried MFT and dilute MFT samples did not give accurate information about the bitumen distribution in MFT, hence observation of wet sample was crucial. Well type slides are commercially available, but these have glass with thickness of glass slide on the bottom. Since the confocal fluorescence microscope, TIRF and CLSM were all inverted epi-fluorescence microscopes, hence the wet sample needed to be placed on the glass cover instead of glass slide. To make this possible well type arrangement needed to be manufactured with glass cover on the bottom. Following steps were taken to manufacture this slide:

- A through hole was etched in the glass slide using a laser at the machine shop. This hole was made of about half a centimeter diameter. The walls were made vertical.
- The glass slide and glass cover were washed first with soap, then with DI water, and finally with ethanol and dried with instrument air to ensure that they were clean.

- Initially the glass slide was secured onto the glass cover using super-glue but eventually they were allowed to stick with their mutual attraction to reduce the possible contamination caused by super-glue.
- The MFT sample or dilute MFT sample drop was placed in this well. The sample quality was small enough to prevent it from touching the walls of the well.
- It was then covered with glass slide to ensure the safety of sample and equipment.

These samples were observed under TIRF and CLSM.

Appendix B: Code for 3D Reconstruction of fluorescence images Bitumen Coating on Clay in MFT Samples

This section gives the detailed code for the creation of 3D reconstruction of individual particles were created by thresholding and segmenting the image over selected region-of-interest as shown in Figure 4-5 image B, C, D and Figure 4-6 image C in Chapter 4. This code was created by the PDF of our group. It was written in python as follows:

```
# -*- coding: utf-8 -*-  
### Program to perform tomographic analysis of 3D images.  
### For the processing, z frames of the 3D image should be extracted as separate  
*.png files and stored in a folder  
#####  
#####  
### On exccuting the code:  
### 1) A windows will pop-up to select folder containing the z-frames extracted images.  
### 2) Once the folder is selected, a 3D colored image will be formed by stacking the z frames.  
### 3) Green channel from the 3D image will be extracted to create a 3D image of shape  
(z_size,y_size,x_size).  
### 4) Top view (x-y plane at z_index) is plotted in the figure titled 'This is full image. Select  
ROI'.  
### 5) This figure will also show the x-z and y-z planes. The z level of top view can be changed  
by setting the variable 'z_index' in the code.  
### 6) You can select region-of-interest (ROI) on the full image by clicking and drawing a  
rectangle of desired shape. The cross-wires at center of the ROI will update automatically.  
### 7) Press the scroll-click (middle click) on the mouse to update x-z and y-z plane section to the  
cross-wire locations. This enables searching z-direction features throughout the 3D image  
### 8) To perform the 3D tomographic recostruction of the selected ROI, 'right-click' on the  
mouse.  
### 9) A new window named 'mayavi scene 1' will be created with tomographic reconstruction  
and top frame of the 3D image.
```

10) You can repeat steps 6-8 to update the tomographic reconstruction in the same 'mayavi scene 1' window.

11) To save the reconstruction, select the figure of step (4) above (where you selected ROI) and press 'SHIFT + P'.

12) A new window will pop-up to save the reconstruction and 3D image of ROI in python pickle format '*.pkl'.

13) A '*.pkl' file can be later opened in program named "Load_3D_reconstruction_pickle.py", for animation and more customized visualization.

```
#####  
#####
```

Additional libraries required to run the code: skimage (for image handling and processing), mayavi (for 3D tomographic visualization)

The thresholding method can be changed in the function definition

'fun_crop_image' by controlling fun_layer_by_layer_3d_threshold

Important: variable 'dist_per_pixel' is used for converting pixels to physical distances in x-y plane and 'total_dist_z' is required ...

... to scale the z-index to physical axial direction. Therefore it is important that these values are assigned correctly in the code.

```
##### Begin Import Important Libraries #####
```

```
import numpy as np  
import matplotlib.pyplot as plt  
import matplotlib.patches as patches  
from Tkinter import * ## creating gui widgets  
import glob ## for loading file names from directory  
import pickle  
import seaborn  
from skimage import io, filters#, transform, img_as_float  
from mayavi import mlab  
from Tkinter import Tk  
from tkFileDialog import askdirectory, asksaveasfilename
```

```

from os.path import dirname, realpath
import sys

##### End Import Important Libraries #####

##### Begin defination of control parameters #####

flag_manually_select_images=1; # set '1' if you want to manually select fluorescent and bright
fiels images.

flag_crop_image =1 # set '1' to crop image

#threshold_manual=100;

dist_per_pixel=20.0/93 ; # this is the resolution of the image in x-y (focal) plane

total_dist_z=4.55; # This is the total distance
z_start_index=0;
z_index=0;
y_index=0;
x_index=0;

length_draw=0;
x_draw=[];
y_draw=[];

pickle_image=[];
pickle_reconstruction=[];

##### code to load images

start_path=dirname(realpath(sys.argv[0])) ## get path of this code.
root = Tk()

```

```
root.withdraw() ## To delete a default Tk window created which does not close.
```

```
if flag_manually_select_images==1:
```

```
    dir_path=askdirectory(initialdir=start_path,parent=root)
```

```
    dir_path_wildcard=dir_path+'/*.png'
```

```
else:
```

```
    dir_path_wildcard=start_path+'/'
```

```
set1_silica_beads_TIRF1950_zbottom_2597pt70_ztop_2602pt15_zsteps75/*.png'
```

```
file_names=sorted(glob.glob(dir_path_wildcard))
```

```
image_3d_raw=io.ImageCollection(file_names) ### Creates a 3D image for series of images.
```

```
image_3d_raw=image_3d_raw[:, :10]
```

```
#number_of_images=len(file_names)
```

```
number_of_images=len(image_3d_raw)
```

```
print 'number of images in z direction = '+str(number_of_images)
```

```
y_size, x_size, color_size= np.shape(image_3d_raw[0]); # x_size and y_size are the  
size of images.
```

```
z_size=number_of_images
```

```
z_end=z_size-1
```

```
dist_per_layer=total_dist_z/z_size
```

```
z_indez=z_end
```

```
##### End definitions of control parameters #####
```

```
##### begin function definitions #####
```

```
xy_index_start=[];
```

```
xy_index_end=[];
```

```

def fun_get_green_from_3D(colored_image_3D):
    """ Takes a 4D skimage.io.collection.ImageCollection and returns 3D green channel
    image.
    y_number, x_number=colored_image_3D[0].shape[0:2]
    z_number=len(colored_image_3D)
    green_image_3D=np.zeros((z_number,y_number,x_number))
    for z_index in range(z_number):
        green_image_3D[z_index,:,:]=colored_image_3D[z_index][:,:,1];
    return green_image_3D

#-----#
def fun_layer_by_layer_3d_threshold2(image_3d,threshold=0.7):
    """ Takes a 3D image as input, computes Binary image with threshold over over the bulk
    of normalized 3D image.
    """ Returns 3D binary image.
    image_binary=np.zeros(image_3d.shape)
    z_number, y_number, x_number = image_3d.shape

    image_3d_norm=image_3d/image_3d.max()

    image_binary = image_3d_norm>threshold
    print 'thresholding executed'
    return image_binary

def fun_layer_by_layer_3d_threshold(image_3d):
    """ Takes a 3D image as input, computes yen threshold on it over a window in z direction
    (as contrast to single threshold value for 3D)
    """ Returns 3D binary image.

```

```

z_window=5; # z stack from -z_window+z_index to z_index+z_window
image_binary=np.zeros(image_3d.shape)
z_number, y_number, x_number = image_3d.shape
for z_index in range(z_number):

    thresh_index=filters.threshold_yen(image_3d[max(0,z_index-z_window):min
(z_index+z_window,z_number),:,:])
    image_binary[z_index,:,:]=image_3d[z_index,:,:]>thresh_index
return image_binary
#-----#

```

```

class draw_roi(object):
    """ This class creates an object to link figure to mouse for selection of ROI on
the top view of 3D image.
    """
    def __init__(self, draw_fig,draw_axis):
        global xy_index_start, xy_index_end;
        global z_start_index, z_index, y_index, x_index
        self.flag_is_pressed=False;

        self.draw_fig=draw_fig;
        self.draw_axis=draw_axis

        self.cross_wire_h_x=[0, x_size];
        self.cross_wire_h_y=[y_index, y_index]

        self.cross_wire_v_x=[x_index, x_index];
        self.cross_wire_v_y=[0, y_size]

```

```

        self.cross_wire_h, =self.draw_axis.plot
(self.cross_wire_h_x,self.cross_wire_h_y,color=(1,0,1),linestyle='--')
        self.cross_wire_v, =self.draw_axis.plot
(self.cross_wire_v_x,self.cross_wire_v_y,color=
(1,0,1),linestyle='--')
        self.draw_axis.axis([0, x_size, y_size,0])
        self.rect = patches.Rectangle((0,0), 1, 1,fill=False, linewidth=2,color=
(1,0,1))
        self.draw_axis.add_patch(self.rect)
        #xlines=
        #self.press=None;

def connect(self):
    #'connect to all events we need'
    self.cidpress=self.draw_fig.canvas.mpl_connect('button_press_event',
self.mouse_down)
    self.cidrelease=self.draw_fig.canvas.mpl_connect
('button_release_event',self.mouse_release)
    self.cidmove=self.draw_fig.canvas.mpl_connect
('motion_notify_event',self.mouse_move)
    self.cidkey=self.draw_fig.canvas.mpl_connect
('key_press_event',self.fun_key_press)

def fun_key_press(self,event):
    if event.key=='P':
        print 'Pickling image reconstruction'
        fun_pickle_reconstruction()

```

```

def mouse_down(self,event):
    global xy_index_start;
    global xy_index_end;
    global z_start_index, z_index, y_index,x_index;

if event.button ==1: # left click
    self.flag_is_pressed=True;
    xy_index_start=(int(event.xdata),int(event.ydata) )

elif event.button==3: # right click
    self.flag_is_pressed=False;
    print 'Processing selected roi'

    fun_crop_image()

else:
    self.flag_is_pressed=False; # scroll click
    print 'updating x y'
    y_index=int((xy_index_start[1]+xy_index_end[1])/2)
    x_index=int((xy_index_start[0]+xy_index_end[0])/2)
    self.cross_wire_h_x=[0, x_size];
    self.cross_wire_h_y=[y_index, y_index]
    self.cross_wire_v_x=[x_index, x_index];
    self.cross_wire_v_y=[0, y_size]

    self.cross_wire_h.set_data(self.cross_wire_h_x,self.cross_wire_h_y)
    self.cross_wire_v.set_data
(self.cross_wire_v_x,self.cross_wire_v_y)

```

```
print x_index, y_index
fun_update_figures()
```

```
def mouse_release(self,event):
    self.flag_is_pressed=False;
    global xy_index_start
    global xy_index_end
    print 'mouse released'
    print xy_index_start

    print xy_index_end
```

```
def mouse_move(self,event):
    global xy_index_end
    global xy_index_start
    if self.flag_is_pressed==True:
        start_coordinates=xy_index_start;
        h=int(event.ydata)-xy_index_start[1]
        w=int(event.xdata)-xy_index_start[0]
        self.rect.set_width(w)
        self.rect.set_height(h)
        self.rect.set_xy(start_coordinates)

        y_index=int((xy_index_start[1]+event.ydata)/2)
        x_index=int((xy_index_start[0]+event.xdata)/2)
        self.cross_wire_h_x=[0, x_size];
        self.cross_wire_h_y=[y_index, y_index]
        self.cross_wire_v_x=[x_index, x_index];
```

```

self.cross_wire_v_y=[0, y_size]

self.cross_wire_h.set_data(self.cross_wire_h_x,self.cross_wire_h_y)
self.cross_wire_v.set_data
(self.cross_wire_v_x,self.cross_wire_v_y)

plt.draw()
xy_index_end=(int(event.xdata),int(event.ydata))
print xy_index_end

#-----#
class draw_and_measure(object):
    """ This class created an object to draw and measure distances on the linked figure and
axis.
    """
    """ This is can be used if z_index of top view is to be manually updated by user selection.
    """
    def __init__(self, draw_fig,draw_axis):
        global x_draw,y_draw, length_draw, dist_per_pixel
        self.flag_is_pressed=False;
        self.draw_fig=draw_fig;
        self.draw_axis=draw_axis
        self.line_draw_handle,= self.draw_axis.plot(x_draw,y_draw,color=
(1,0,1),linewidth=3)

    def connect(self):
        #'connect tinitialdiro all events we need'
        self.cidpress=self.draw_fig.canvas.mpl_connect('button_press_event',
self.mouse_down)
        self.cidrelease=self.draw_fig.canvas.mpl_connect
('button_release_event',self.mouse_release)

```

```

        self.cidmove=self.draw_fig.canvas.mpl_connect
('motion_notify_event',self.mouse_move);

def mouse_down(self,event):
    global x_draw,y_draw,length_draw;

    if event.button ==1:
        self.flag_is_pressed=True;
        #print 'hahahah'
        x_draw.append(event.xdata);
        y_draw.append(event.ydata);
        self.fun_compute_length()
        self.line_draw_handle.set_data(x_draw,y_draw)
        self.draw_axis.set_title('Length = '+str(length_draw)+'  $\mu\text{m}$ ')
        self.draw_fig.canvas.draw()

    elif event.button==3:
        self.fun_update_z_range()
        print 'right click to update z'

    else: ## event.button=2
        print 'central click to reset line'
        x_draw=[];
        y_draw=[];
        self.line_draw_handle.set_data(x_draw,y_draw)
        self.draw_fig.canvas.draw()

def mouse_release(self,event):

```

```
self.flag_is_pressed=False
```

```
def mouse_move(self,event):
```

```
    if self.flag_is_pressed==True:
```

```
        x_draw.append(event.xdata);
```

```
        y_draw.append(event.ydata);
```

```
        self.fun_compute_length()
```

```
        self.line_draw_handle.set_data(x_draw,y_draw)
```

```
        self.draw_axis.set_title('Length = '+str(length_draw)+'  $\mu\text{m}$ ')
```

```
        self.draw_fig.canvas.draw()
```

```
def fun_compute_length(self):
```

```
    global x_draw,y_draw, length_draw
```

```
    if len(x_draw)>1:
```

```
        dx=np.diff(x_draw);
```

```
        dy=np.diff(y_draw);
```

```
        length_draw=sum(np.sqrt(dy**2+dx**2))*dist_per_pixel;
```

```
def fun_update_z_range(self):
```

```
    global z_start_index, z_index
```

```
    #print x_draw
```

```
    z_start_index=int(min(y_draw))
```

```
    z_index=int(max(y_draw))
```

```
    print z_start_index, z_index
```

```
    fun_update_figures()
```

```
#-----#
```

```
def fun_update_figures():
```

```

    global ax2_full_image, ax3_full_image
    #fig_front_view.clf()
    #ax_front_view=fig_front_view.add_subplot(111)
    ax2_full_image.imshow(image_3d_green[:,y_index:],cmap=color_map_used)
### Update
front view
    plt.show()
    plt.draw()
    #ax2_full_image.axis([0, x_size, y_size,0])
    ax3_full_image.imshow(np.transpose(image_3d_green
[:,x_index]),cmap=color_map_used) ### Update side view
    #ax3_full_image.axis([0, x_size, y_size,0])
    plt.show()
    plt.draw()

#-----#

def fun_crop_image():
    global fig_global_handle
    global axes_global_handle
    global pickle_reconstruction, pickle_image
    if len(xy_index_end)>0:
        print 'Start index =', xy_index_start[1]
        print 'end index= ', xy_index_end[1]
        print 'z range =',(z_start_index,z_end)

        h=xy_index_end[1]-xy_index_start[1];
        w=xy_index_end[0]-xy_index_start[0];
        print 'h=', h
        print 'w=', w
        image_3d_roi=image_3d_green[:, xy_index_start[1]:xy_index_end

```

```

[1],xy_index_start[0]:xy_index_end[0] ]

    print np.shape(image_3d_roi)
    #image_3d_green=fun_get_green_from_3D(image_3d_raw)

    fig_roi=plt.figure('ROI')
    fig_roi.clf()
    ax_roi=fig_roi.add_subplot(111)
    ax_roi.imshow(image_3d_roi[z_index,:,:],cmap='gray')
    plt.draw()

    #hist_3d = exposure.histogram(image_3d_roi);

    image_binary_3d=fun_layer_by_layer_3d_threshold2
(image_3d_roi,threshold=0.45) ## select binary threshold value
    #image_binary_3d=fun_layer_by_layer_3d_threshold(image_3d_roi) ##
Thresholding according to Yen algorithm

    fig_seg=plt.figure('Segmentation (Yen in xy, adaptive in z)')
    fig_seg.clf()
    ax_seg=fig_seg.add_subplot(111)
    ax_seg.imshow(image_binary_3d[z_index,:,:],cmap='gray')
    plt.show()
    plt.draw()

    x_b, y_b, z_b =fun_reconstruct3D_object(image_binary_3d, range
(z_start_index,z_end))
    z_b=z_b+z_start_index*dist_per_layer;

```

```

particle_radius=0.75*np.ones(np.shape(x_b));

##### store reconstructed image into pickle variable #####
pickle_reconstruction=[x_b,y_b,z_b]
### store image into pickle variable ###
pickle_image=image_3d_roi[z_start_index:z_end,:,:]

fig_maya1=mlab.figure(1,bgcolor=(0,0,0))
mlab.clf(fig_maya1)
pts=mlab.points3d

(x_b,y_b,z_b,particle_radius,scale_factor=0.25,opacity=1,color=(0.0,0.8,0.0))
mlab.axes()
mlab.orientation_axes()
#mlab.outline()
mlab.draw()
mlab.show()

photo=mlab.imshow(np.transpose(image_3d_roi[z_end,:,:]),opacity=0.75)
## use
transpose to make orientation of image consistant with the 3D plotting of data.

photo.actor.position=[0.5*w*dist_per_pixel,0.5*h*dist_per_pixel,
(z_end)*dist_per_layer]
photo.actor.scale=[dist_per_pixel,dist_per_pixel,1]
mlab.view(-45,60)
#mlab.zoom(0.8)

#-----#

```

```

def fun_reconstruct3D_object(binary_image_3d,z_index_range):
    #### takes 3D binary image as input and returns the x,y,z coordinates of True values.
    #### z_index_range is the range over which the above mentioned computation is
done.

    bitumen_pts= np.where(binary_image_3d[z_index_range,:]==True)

    z_b=dist_per_layer*bitumen_pts[0]
    y_b=dist_per_pixel*bitumen_pts[1]
    x_b=dist_per_pixel*bitumen_pts[2]
    return x_b,y_b, z_b

# _____ #

```

```

def fun_pickle_reconstruction():
    #### This function stores the reconstructed structure and 3D image in pickle.
    #### The data is saved in first-in-first-out format.
    #### Image is stored first so, it will be loaded first.
    #### The stored 3D image needs to be transposed in x-y plane for superimposition
on 3D structure.

    global pickle_image, pickle_reconstruction
    dict_parameters={'dist_per_pixel':dist_per_pixel,'dist_per_layer':dist_per_layer}

    filename=asksaveasfilename
    (defaultextension='.pkl',initialdir=start_path,title='enter filename of pickle',
initialfile='reconstruction')

    #filename=start_path+'/reconstruction.pkl'
    pickle_out=open(filename,'wb')
    pickle.dump(pickle_image,pickle_out)
    pickle.dump(pickle_reconstruction,pickle_out)
    pickle.dump(dict_parameters,pickle_out)
    pickle_out.close()

```

```
##### End function definitions #####
```

```
##### Extract Green channel
```

```
image_3d_green=fun_get_green_from_3D(image_3d_raw) ### Extracts the Green channel for  
the 3D image.
```

```
##### plot the top view of image at 'z_index' #####
```

```
fig_full_image=plt.figure('This is full image. Select ROI.',figsize=(8,6))
```

```
fig_full_image.clf()
```

```
ax1_full_image=fig_full_image.add_subplot(221)
```

```
ax2_full_image=fig_full_image.add_subplot(223)#,sharex=ax1_full_image)
```

```
ax3_full_image=fig_full_image.add_subplot(222)#,sharey=ax1_full_image)
```

```
color_map_used='hot' # Color map of the image
```

```
ax1_full_image.imshow(image_3d_green[z_index,:,:],cmap=color_map_used)
```

```
ax1_full_image.axis([y_size,0, 0, x_size])
```

```
ax1_full_image.set_xlim([0, 500])
```

```
ax1_full_image.grid(1)
```

```
ax2_full_image.imshow(image_3d_green[:,y_index,:],cmap=color_map_used) # front view
```

```
ax2_full_image.axis([0, x_size, z_size,0])
```

```
ax3_full_image.imshow(np.transpose(image_3d_green[:,:,x_index]),cmap=color_map_used)
```

```
#side view
```

```
ax1_full_image.set_xticklabels([])
```

```
ax1_full_image.set_yticklabels([])
```

```
ax2_full_image.set_xticklabels([])
```

```
ax2_full_image.set_yticklabels([])
```

```
ax3_full_image.set_xticklabels([])
```

```
ax3_full_image.set_yticklabels([])
```

```
ax1_full_image.set_ylabel('$\leftarrow$ $y$ $\rightarrow$',fontsize=24)
```

```
ax2_full_image.set_xlabel('$\leftarrow$ $x$ $\rightarrow$',fontsize=24)
```

```
ax2_full_image.set_ylabel('\leftarrow$ $z$',fontsize=20)
ax3_full_image.set_xlabel('$z$ $\rightarrow$',fontsize=24)
plt.show()
plt.draw()
a_object=draw_roi(fig_full_image,ax1_full_image); ### object for ROI
a_object.connect(); ### connect canvas
```

Appendix C: Code for Animation of the 3D Reconstruction of fluorescence images Bitumen Coating on Clay in MFT Samples

This section gives the detailed code for the creation animation which constructs layer by layer and then rotates the 3D reconstruction of individual particles over selected region-of-interest of images such as those described in appendix B. This code was created by the PDF of our group.

```
#### This code loads 3D reconstructed structure and image. The 3D image needs to be transposed in x-y plane before superimposing with 3D structure.
```

```
#### The data in .pkl file is stored in first-in-first-out format. Since image was stored first, it will be loaded first.
```

```
#### After the reconstruction is loaded, it is visualized using Mayavi.
```

```
####
```

```
from Tkinter import Tk
```

```
from tkFileDialog import askopenfilename
```

```
from mayavi import mlab
```

```
import pickle
```

```
import sys
```

```
from os.path import dirname, realpath
```

```
import numpy as np
```

```
from tkFileDialog import askdirectory
```

```
##### begin definition of control parameter #####
```

```

flag_save_mavayi=1; # set '1' to save reconstruction animation

flag_show_construction=1; # set '1' to visualize reconstruction while animation is being saved.

##### end definition of control parameters #####

##### begin Function definition #####

def fun_3d_visualization(x_b,y_b,z_b,top_image,z_height):

    ### visualization commands

    particle_radius=0.75*np.ones(np.shape(x_b));

    fig_maya1=mlab.figure(1,bgcolor=(0,0,0),fgcolor=(1,1,1))

    #fig_maya1=mlab.figure(1,bgcolor=(1,1,1),fgcolor=(0.3,0.3,0.3))

    mlab.clf(fig_maya1)

    pts=mlab.points3d(x_b,y_b,z_b,particle_radius,scale_factor=0.3,opacity=1,color=

    (0.8,0.8,0.8))

    mlab.axes()

    mlab.orientation_axes()

    #mlab.outline()

    mlab.draw()

    #mlab.axis('on')

    #mlab.axes('equal')

```

```

#pts.actor.actor.scale=(1,1,1)

mlab.show()

### superimpose image on 3D structure

#z_position=z_height+particle_radius;

#top_image=image_3d[-1,:,:]

photo=mlab.imshow(np.transpose(top_image),opacity=0.3) ## use transpose to make
orientation of image consistent with the 3D plotting of data.

photo.actor.position=[0.5*w*dist_per_pixel,0.5*h*dist_per_pixel,z_height]

#photo.actor.position=[0.5*w*dist_per_pixel,0.5*h*dist_per_pixel,(z_index+2)*dist_per
_layer]

photo.actor.scale=[dist_per_pixel,dist_per_pixel,1]

mlab.view(-45,75)

return fig_maya1

##### End function definition #####

##### Begin main code #####

### code to ui get pickle filename

path=dirname(realpath(sys.argv[0]))

root = Tk()

root.withdraw() ## To delete a default Tk window created which does not close.

```

```

start_dir=path; #### Start directory

filename=askopenfilename(initialdir=start_dir,parent=root,title='select a pickle
file',filetypes=[('pickle file','*.pkl')])

#### Load pickle

pickle_in=open(filename,'rb') #### open pickle file

image_3d = pickle.load(pickle_in) #### load the 3D image.

structure_3d=pickle.load(pickle_in) #### load the coordinates of the structure

dict_parameters=pickle.load(pickle_in) #### load the imaging parameters

pickle_in.close() #### close the pickle file

#### store coordinates of structure in variables

x_b=structure_3d[0];

y_b=structure_3d[1];

z_b=structure_3d[2];

dist_per_pixel= dict_parameters['dist_per_pixel']

dist_per_layer= dict_parameters['dist_per_layer']

```

```

### call visualization function

z_height=max(z_b)

z_h,h,w=np.shape(image_3d)

if flag_save_mavayi==1:

dir_path=askdirectory(initialdir=start_dir,parent=root);

count_image=0;

if flag_show_construction==1:

    #z_index=30

    for z_index in range(z_h):

        #z_height=min(z_b)+z_index*dist_per_layer;

        z_height=z_index*dist_per_layer;

        #lower_pts=np.where(z_b<z_height)[0]

        lower_pts=np.where(z_b<z_height)[0]

        print len(lower_pts)

        fig_mayavi=fun_3d_visualization(x_b[lower_pts],y_b[lower_pts],z_b

[lower_pts],image_3d[z_index,:,:,z_height=z_height)

```

```

    if flag_save_mavayi==1:

        filename_image=dir_path+'/'+'{:03}'.format(count_image)+'.png'

        mlab.savefig(filename_image,figure=fig_mayavi)

        count_image+=1

        print 'saving image at', filename_image

view_angle=mlab.view()[0]

view_azimuth=mlab.view()[1]

for count_angle in np.linspace(0,2*360,100):

    mlab.view(view_angle+count_angle,view_azimuth)

    if flag_save_mavayi==1:

        filename_image=dir_path+'/'+'{:03}'.format(count_image)+'.png'

        mlab.savefig(filename_image,figure=fig_mayavi)

        count_image+=1

        print 'saving image at', filename_image

else:

    #z_height=min(z_b)+z_h*dist_per_layer;

    z_height=z_h*dist_per_layer;

    fun_3d_visualization(x_b,y_b,z_b,image_3d[-1,:::],z_height=z_height)

```